UNIVERSITY OF NOVA GORICA
GRADUATE SCHOOL

Zr/Cu-TiO_2 CATALYSTS FOR PHOTOCATALYTIC WATER TREATMENT

DISSERTATION

Olena Pliekhova

Mentor: Prof. Dr. Urška Lavrenčič Štangar

Nova Gorica, 2019

UNIVERZA V NOVI GORICI
FAKULTETA ZA PODIPLOMSKI ŠTUDIJ

Zr/Cu-TiO_2 KATALIZATORJI ZA FOTOKATALITSKO ČIŠČENJE VODE

DISERTACIJA

Olena Pliekhova

Mentorica: prof. dr. Urška Lavrenčič Štangar

Nova Gorica, 2019

UNIVERSITY OF NOVA GORICA
GRADUATE SCHOOL

Olena Pliekhova, *Zr/Cu-TiO_2 catalysts for photocatalytic water treatment*, Dissertation, (2019)

Acknowledgements

I would like to express my greatest gratitude to my supervisor Prof. Dr. Urška Lavrenčič Štangar. Foremost, her huge kind heart and personality deserve acknowledgements. It is the biggest honour and pleasure to work under the supervision of the person who in harmony combines the best personal and very high quality professional features. Urška, thank you very much for your meaningful suggestions, inspiring guidance, unconditional support and united superintendence and freedom, which gave me an opportunity to grow up as a scientist and develop as a person. Thank you sincerely, I will always owe you!

From the beginning of my thesis, I would like to declare formal acknowledgements. Financial support from Infinity program in the framework of the EU Erasmus Mundus Action 2 and Slovenian-Belgian ARRS-FWO project "Development of advanced TiO_2-based photocatalyst for the degradation of organic pollutants from wastewater" (2015 – 2019) made this research technically possible.

My sincere thanks go also to the other scientists who have invested their time and shared their knowledge with me. It will not be possible to finish this work and to achieve the results without you:

Prof. Dr. Iztok Arčon from the University of Nova Gorica. I would like to express appreciation for EXAFS and XANES measurements, calculations and help with writing discussions. Thank you very much! You have opened for me completely new world of synchrotron radiation facilities. Thank you for your patient and comprehensible explanations of the atomic structure of materials and fruitful discussions, which resulted in two articles.

Prof. Dr. Mattia Fanetti from the University of Nova Gorica. I am deeply thankful for TEM measurements and interpretations. It was difficult to find time in your tight schedule, but you were always willing to help. Thank you for your time, enthusiasm and dipping in the problem.

Doc. Dr. Zuzana Babrierikova and Prof. Dr. Vlasta Brezova from Slovak University of Technology in Bratislava. I am extremely grateful for insights into EPR measurements, results interpretation and help in writing discussions. Thanks a lot for your hospitality during my stay in Bratislava. I hope that our collaboration will continue and will bear fruits in a form of articles and new discoveries.

Doc. Dr. Dorota Korte and Doc. Dr. Humberto Cabrera for assistance and guidance with TLS technique.

I would like to appreciate time and kindness of Dr. Andraž Mavrič, Dr. Iuliia Mikulska and Ms. Mojca Vrčon for initial orientation and induction training in using DLS and XRD equipment.

I feel thankful to all the current and former co-workers from the Laboratory for Environmental and Life Science of University of Nova Gorica. Special thanks to Prof. Dr. Mladen Franko for his wise and tireless management activities. Thanks go to always available and helpful secretaries, Ms. Nadja Lovec Santaniello and Ms. Marina Artico for their help in difficult situations. Thanks to all staff of entire University of Nova Gorica who I ever worked or met with. You have always being friendly and supportive. I am glad that I was working with you; it is a great luck to be surrounded by people like you. Thanks a lot!

Finally, I would like to thank my committee members, Prof. Dr. Pegie Cool, Prof. Dr. Matjaž Valant and Prof. Dr. Claudio Minero for constructive critique and willingness to make this dissertation better.

My sincere and very personal thanks go to Sabina Zelinšček. There are not enough words to express all my gratitude and feelings. You were helping me from the very first day I came to Slovenia. You continue supporting me now. Thank you very much my dear friend! Hanna Budasheva, I am glad that we spent this year together. I have learned something from you! I wish you good luck and thanks for the friendship! You both girls, made my life brighter!

At last, but not least I would like to express my gratitude to my husband Oleksii and to my sons Andrii and Illia. You are my dear friends, my support, my love… my life. It is priceless treasure to have you all by my side. Thank you for encouraging me, for believing in me, for the chance to be myself near you.

Abstract

This work entitled «Zr/Cu-TiO_2 catalysts for photocatalytic water treatment» tackles a problem of tons of dyes discharged everyday mainly from textile industries. This is a huge concern because of dyes persistence, toxicity and potential to the bioaccumulation in living organisms. Here, a small contribution to overall problem is presented.

The research work consists of three main parts: Theoretical background, Experimental and Results and discussion. In the Theoretical background chapter the overall problem is identified and discussed. The main water treatment techniques are presented briefly with their advantages and drawbacks. Photocatalysis assisted with TiO_2 is shown as an alternative additional technique with its own pros and cons. Further, a cursory overview of TiO_2 modification techniques is made and advantages in using copper and zirconium oxides for TiO_2 modification are presented. The reason and possible positive effect of using of two oxides simultaneously for TiO_2 modification is indicated. Additionally, a positive impact of solar light for overall rate of dyes degradation assisted with TiO_2 is discussed. Within the framework of photosensitization effect, the problem of using dyes for assessment of photocatalytic properties of materials under the visible light is touched on. Photothermal methods as possible beneficial techniques for this purpose are proposed.

In the Experimental chapter, all experimental techniques used in current research work with the technical details specific for the research work are presented. There are methods of materials preparation, photocatalytic tests under different conditions and varying model pollutants, and physico-chemical characterization techniques.

The Results and discussion chapter is divided by three subchapters. Each chapter is dedicated to one hypothesis, which was checked and confirmed or disproved. The first hypothesis is about beneficial loading of copper and zirconium oxides to TiO_2. After numerous experiments held, it was concluded that the pair of copper and zirconium oxides is beneficial for simultaneous application on TiO_2 surface to promote its performance.

The second subchapter is about zirconium distribution and its impact on the activity of studied materials towards the antraquinone dye Reactive Blue 19. Different techniques such as XRD, TEM, EXAFS and many others were used in

order to characterize the materials and to understand the details of the processes taking place. The existence of upper limit of copper oxide loading for its beneficial effect on TiO_2 performance was demonstrated. It was observed that zirconium species loading leads to improvement in performance of materials with higher copper loading, which otherwise lowers activity of TiO_2 – this is in case when copper only above its optimal level is present. It was concluded that zirconium oxide containing species occupy rutile surface sites in mixed phase TiO_2 and this way beneficially influence the material performance towards the dye removal.

The third subchapter is about the visible light TiO_2 assisted dye degradation. It is well known that photosensitization mechanism of dye degradation appears under the visible and as a consequence under the solar light irradiation. This leads to the overall enhancement of dyes degradation, which is positive and may be used as a benefit for faster pollutant destruction. However, this fact leads to mishmash in the determination of real photocatalytic activity of materials towards the dye. It was hypothesized that the impact of photosensitization mechanism on the overall material performance against Reactive blue 19 dye (RB19) descends with the dye concentration lowering. Thermal lens spectrometry (TLS) which is sensitive to chemicals at low concentrations was used for hypothesis evaluation.

To summarize the research work achievements, the conclusions of the thesis are given at the end.

Key words: titanium dioxide, photocatalysis, zirconium/copper, surface modification, water treatment, dyes

Povzetek

Doktorsko delo z naslovom Zr/Cu-TiO_2 katalizatorji za fotokatalitsko čiščenje vode obravnava problematiko odpadnih barvil, ki jih v velikih količinah odlaga predvsem tekstilna industrija. Slednje vzbuja skrb zaradi njihove trdovratnosti, toksičnosti in možnosti bioakumulacije v živih organizmih. V nadaljevanju bo predstavljen majhen prispevek k celotni problematiki.

Raziskovalno delo sestoji iz treh glavnih delov: teoretičnega ozadja, eksperimentalnega dela ter rezultatov in razprave. Teoretični del predstavi celotno problematiko in o njej razpravlja. V tem poglavju so na kratko predstavljene prednosti in pomanjkljivosti tehnik čiščenja vode. Prikazana je tudi TiO_2-fotokataliza kot alternativna pomožna tehnika s svojimi prednostmi in slabostmi. Sledi splošen pregled tehnik za modificiranje TiO_2 ter predstavitev prednosti pri uporabi bakra in cirkonija pri modifikaciji TiO_2. Nakazan je tudi razlog za simultano uporabo dveh oksidov v modifikaciji TiO_2 ter možni pozitivni učinki. Obravnavan je pozitivni učinek sončne svetlobe na celokupno stopnjo razpada barvil v prisotnosti TiO_2. V okviru učinka fotoobčutljivosti je obravnavan tudi problem uporabe barvil pri oceni fotokatalitičnih lastnosti materialov pod vplivom vidne svetlobe. V tem oziru se kot primernejše predlagajo fototermične metode.

V eksperimentalnem delu so predstavljene vse eksperimentalne tehnike, ki sem jih uporabila v raziskovalnem delu, skupaj s tehničnimi podrobnostmi, ki so pomembne za raziskavo. V tem poglavju so predstavljene metode priprave materialov, fotokatalitični testi, opravljeni pod različnimi pogoji in s spremenljivimi modelnimi onesnaževali, ter tehnike fizikalno-kemijske karakterizacije.

Poglavje Rezultati in razprava se deli na tri podpoglavja, od katerih se vsako posveča svoji hipotezi, ki je bila preverjena in potrjena ali ovržena. Prva hipoteza se nanaša na ugoden vnos bakrovega in cirkonijevega oksida v sintezi TiO_2. Po opravljenih številnih poskusih sem lahko zaključila, da sta bakrov in cirkonijev oksid ugoden par za hkratno modifikacijo površine TiO_2 pri spodbujevanju njegovega delovanja.

Drugo podpoglavje se nanaša na razporeditev cirkonija in njegov vpliv na aktivnost obravnavanih materialov glede na antrakinonsko barvilo Reactive Blue 19. Za karakterizacijo materialov in razumevanje podrobnosti procesov sem uporabila različne tehnike, kot so XRD, TEM, EXAFS in druge. Dokazana je bila najvišja meja

vnosa bakrovega oksida, ko še ugodno vpliva na delovanje TiO_2. Opaziti je bilo, da dodatek cirkonija vodi k izboljšanju delovanja materialov z visoko vsebnostjo bakra, ki pa drugače znižuje aktivnost TiO_2 − to se zgodi v primeru, ko je baker prisoten v rahlem presežku glede na njegovo optimalno raven. Ugotovili smo, da zvrsti, ki vsebujejo cirkonijev oksid, zasežejo površine rutila v dvofaznem TiO_2 in tako ugodno vplivajo pri delovanju materiala na barvilo.

Tretje podpoglavje se nanaša na razpad barvila pod vplivom TiO_2 in vidne svetlobe. Znano je, da se mehanizem fotoobčutljivosti pri razpadu barvila pokaže pri obsevanju z vidno in posledično tudi s sončno svetlobo. To vodi k celokupnemu ojačenju razpada barvila, kar ima pozitivne vidike in se lahko dobro uporablja pri hitrejšemu odstranjevanju onesnaževala, po drugi strani pa to vodi v nepravilnosti pri določanju pravih fotokatalitičnih aktivnosti materialov na barvilo. Predvidevali smo, da se vpliv mehanizma fotoobčutljivosti na celokupno delovanje materiala na barvilo Reactive blue 19 (RB19) znižuje skupaj z zmanjševanjem koncentracije barvila. Pri ovrednotenju te hipoteze smo uporabili tehniko spektrometrije termičnih leč (TLS), ki je občutljiva na nizke koncentracije kemikalij.

Dosežki raziskovalnega dela so povzeti v zaključkih na koncu naloge.

Ključne besede: titanov dioksid, fotokataliza, cirkonij/baker, modifikacija površine, čiščenje vode, barvila

TABLE OF CONTENTS

Acknowledgements VII
Abstract IX
Povzetek XI
LIST OF TABLES XV
LIST OF FIGURES XVII
ABBREVIATIONS XXIII
INTRODUCTION 1
1 THEORETICAL BACKGROUND 3
1.1 OVERALL PROBLEM STATEMENT 3
1.1.1 Textile processing and its global water impact 3
1.1.2 Photocatalysis as an effective technique for water purification 6
1.1.3 Basics about TiO_2 as a photocatalyst 10
1.1.3.1 TiO_2 crystal polymorphs 10
1.1.3.2 The size of TiO_2 particles 13
1.1.4. Shortcoming and weakness of TiO_2 14
1.2. DETAILED UNDERSTANDING OF THE RESEARCH WORK ISSUE 15
1.2.1 Different techniques for TiO_2 modification 15
1.2.2 Advantages of TiO_2 modification with the second material 18
1.2.2 Copper oxide as TiO_2 modifier 20
1.2.3 Zirconium oxide as TiO_2 modifier 23
1.2.4 Multicomponent TiO_2 modification 23
1.2.3 Dye and the visible light activity connected problems. Thermal lens spectrometry for photocatalytic activity evaluation 24
1.3. HYPOTHESIS, GOALS AND OBJECTIVES 30
2 EXPERIMENTAL 33
2.1. PREPARATION OF PHOTOCATALYSTS 33
2.2. PHOTOCATALYTIC TESTS 34
2.3. CHARACTERIZATION OF Cu/Zr-TiO_2CATALYST 35
2.3.1 X-ray diffractometry (XRD) 35
2.3.2 Scanning electron microscopy (SEM) and energy dispersive X-ray (EDX) 36
2.3.3 Transmission electron microscopy (TEM) 37
2.3.4 Nitrogen sorption measurements (BET SSA) 38
2.3.5 Diffuse reflectance UV/VIS spectroscopy (DRS) 39

2.3.6 Dynamic light scattering (DLS) ... 39
2.3.7 $HO^{\cdot}$ radical capturing test ... 40
2.3.8 Amine titration for determination of surface acidity of Cu/Zr-TiO_2 catalysts ... 41
2.3.9 Complexometric titration with EDTA ... 42
2.3.10 Isoelectric point (IEP) ... 42
2.3.11 X-ray absorption spectroscopy (EXAFS and XANES) ... 43
2.3.12 Electron paramagnetic resonance (EPR) spectroscopy ... 45
2.3.13 Thermal lens spectrometry (TLS) ... 46
2.4. PHOTOCATALYTIC FILMS ... 48
2.4.1 Film preparation ... 48
2.4.2 Mechanical stability test ... 49
3. RESULTS AND DISCUSSION ... 51
3.1. EVALUATION OF THE FIRST HYPOTHESIS. ... 51
SIMULTANEOUS LOADING OF Cu AND Zr IONS FOR PHOTOCATALYTIC DEGRADATION OF WATER POLLUTANTS UNDER THE SIMULATED SOLAR LIGHT ... 51
Conclusions ... 64
3.2. EVALUATION OF THE SECOND HYPOTHESIS. ... 65
Cu AND Zr SURFACE SITES IN PHOTOCATALYTIC ACTIVITY OF TiO_2 NANOPARTICLES: THE EFFECT OF Zr DISTRIBUTION ... 65
Conclusions ... 91
3.3. EVALUATION OF THE THIRD HYPOTHESIS. ... 93
TLS FOR DETERMINATION OF RB19 DEGRADATION UNDER THE SIMULATED SOLAR LIGHT ... 93
Conclusions ... 103
CONCLUSIONS OF THE THESIS AND FUTURE OUTLOOK ... 105
REFERENCES ... 107

LIST OF TABLES

Table 1. Phase composition, particle size, specific surface area (SSA) and Zr/Cu loading of TiO_2 catalysts. 51

Table 2. Parameters of the nearest coordination shells around Cu cations in the P25/Zr/$Cu_{0.1}$ sample after drying at 150 °C, and calcined at 500 °C, and in the P25/Zr/$Cu_{0.5}$ sample calcined at 500 °C: average number of neighbor atoms (*N*), distance (*R*), and Debye-Waller factor (σ^2). Uncertainty of the last digit is given in parentheses. A best fit is obtained with the amplitude reduction factor $S_0^2 = 0.85$. The shift of the energy origin ΔE_o and *R*-factor (quality of fit parameter), are listed in the last column. 62

Table 3. Data from X-ray diffraction patterns and copper/zirconium loading of Cu/Zr modified P25 photocatalysts. 67

Table 4. The band gaps of P25 modified with Cu and Zr ions estimated from Kubelka Munk curves. 69

Table 5. Parameters of the nearest coordination shells around Cu cations in the Cu modified P25 photocatalysts at 0.05%, 0.1% and 0.5% Cu loading: average number of neighbor atoms (*N*), distance (*R*), and Debye-Waller factor (σ^2). Uncertainty of the last digit is given in parentheses. A best fit is obtained with the amplitude reduction factor $S_0^2 = 0.85$. The shift of the energy origin ΔE_o and *R*-factor (quality of fit parameter), are listed in the last column. 84

Table 6**.** Parameters of the nearest coordination shells around Cu cations in the Cu modified P25 photocatalysts at 1% and 3% Cu loading: average number of neighbor atoms (*N*), distance (*R*), and Debye-Waller factor (σ^2). Uncertainty of the last digit is given in parentheses. A best fit is obtained with the amplitude reduction factor $S_0^2 = 0.85$. The shift of the energy origin ΔE_o and *R*-factor (quality of fit parameter), are listed in the last column. 85

Table 7**.** Parameters of the nearest coordination shells around Cu cations in the Cu/Zr modified P25 photocatalysts: average number of neighbour atoms (*N*), distance (*R*), and Debye-Waller factor (σ^2). Uncertainty of the last digit is given in parentheses. A best fit is obtained with the amplitude reduction factor $S_0^2 = 0.90$. The

shift of the energy origin ΔE_o and *R*-factor (quality of fit parameter), are listed in the last column. 86

Table 8. Parameters of the nearest coordination shells around Zr cations in the Zr and Cu/Zr modified P25 photocatalysts: average number of neighbor atoms (*N*), distance (*R*), and Debye-Waller factor (σ^2). Uncertainty of the last digit is given in parentheses. A best fit is obtained with the amplitude reduction factor $S_0^2 = 0.90$. The shift of the energy origin ΔE_o and *R*-factor (quality of fit parameter), are listed in the last column. 87

Table 9. The fraction (F) of anatase and rutile surface sites covered by a modifier. 90

LIST OF FIGURES

Fig. 1. Structural formula of C.I. Reactive Blue 19 and C.I. Basic Blue 9 (Methylene blue). 4

Fig.2. Crystal structure of (a) anatase, (b) rutile, (c) brookite (Carp et al. 2004). 11

Fig. 3. The mechanism of charge separation on P25. (A) Model of P25 activity where charge separation occurs on anatase and rutile acts as an electron sink (Bickley et al. 1991). (B) Proposed model of a rutile antenna and subsequent charge separation (Hurum et al. 2003). 12

Fig. 4. (a) General model of TiO_2 photocatalysis. (b) TiO_2 modified structure exhibiting TiO_2 composite heterojunction (Dahl et al. 2014). 19

Fig. 5. The schematic pattern of the reverse charge localization mechanism on CuO modified rutile TiO_2. 22

Fig. 6. Comparison of the photocatalytic mechanism (A) for UV irradiation of TiO_2 with the self-photosensitized pathway (B) of dye degradation under visible light (Wu et al. 1998b) 26

Fig. 7. Photocatalyst assisted RB19 degradation pathway based on mass spectrometry: A) under the UV light; B) under the simulated solar light. The preferential bond cleavage at initial stage of RB19 dye degradation is marked. 27

Fig. 8. Scheme of the TLS experimental setup. L1, L2, L3, L4, L5: lenses, M1, M2, M3, M4: reflecting mirrors, DM: dichroic mirror. 47

Fig. 9. Optical absorption spectrum of RB19. 48

Fig. 10. X-ray diffraction patterns of pure P25 and Cu and Zr modified P25 photocatalysts. 52

Fig. 11. Photocatalytic MB decolorization promoted by Cu and Zr modified P25 nanoparticles under the simulated solar light (determined rate constants (k±0.01, min^{-1}): 0.08 for P25, 0.09 for P25/Zr, 0.11 for P25/$Cu_{0.1}$, 0.04 for P25/$Cu_{0.5}$, 0.16 for P25/Zr/$Cu_{0.1}$). 53

Fig. 12. The photocataltytic mineralization of MB with P25 and P25/Zr/$Cu_{0.1}$ catalysts determined by TOC measurements. 54

Fig. 13. The kinetics of HTPA formation with Cu and Zr modified P25 catalysts (determined rate constants (k±$1\cdot10^{-4}$, min^{-1}): $7\cdot10^{-3}$ for P25, $6\cdot10^{-5}$ for P25/Zr, $2\cdot10^{-3}$ for P25/$Cu_{0.1}$, $8\cdot10^{-4}$ for P25/$Cu_{0.5}$, $4\cdot10^{-3}$ for P25/Zr/$Cu_{0.1}$). 56

Fig. 14. SEM images and qualitative EDX spectra of a) unmodified P25 and b) P25/Zr/$Cu_{0.1}$. 57

Fig. 15. The mean diameter of agglomerates of Cu and Zr modified P25 measured by DLS at three time intervals (0, 30, 60 min) after 1h stabilization of ultrasonically treated suspension. 58

Fig. 16. Cu K-edge XANES spectra of the P25/Zr/$Cu_{0.1}$ sample after drying at 150°C, and calcined at 500 °C, and P25/Zr/$Cu_{0.5}$ sample calcined at 500 °C. Reference Cu^{+} and Cu^{2+} copper compounds with different Cu cation coordinations (Cu_2O, CuO, $CuSO_4 \cdot 5\ H_2O$, $Cu(OH)_2$, $Cu(NO_3)_2\cdot 2{,}5H_2O$ crystalline and 0.1M aqueous solution of $Cu(NO_3)_2$) are shown for comparison. The spectra are shifted vertically for clarity. The pre-edge shoulder at 8983 eV in the calcined P25/Zr/$Cu_{0.1}$ sample is indicated by the arrow. 60

Fig. 17. Fourier transform magnitude of k^3-weighted Cu EXAFS spectra of the P25/Zr/$Cu_{0.1}$ sample after drying at 150 °C, and calcined at 500 °C, and P25/Zr/$Cu_{0.5}$ sample calcined at 500 °C, calculated in the k range of 2.5 – 11 $Å^{-1}$ and R range of 1 to 3.5 Å. Experiment – (solid line); model -- (dashed line). 61

Fig. 18. Scratch resistance test of immobilized layers of photocatalysts (6H – the hardest, 6B – the softest pencil). 66

Fig. 19. Kubelka-Munk transformed UV-Vis reflectance of powder Cu/Zr modified TiO_2 photocatalysts. 68

Fig. 20. Isoelectric point of Cu/Zr modified samples of TiO_2. 70

Fig. 21. Degradation of RB19 by Cu/Zr modified TiO_2. UV results correspond to calculated degree of dye degradation measured by UV-Vis spectroscopy (bleaching) after 50 min of light irradiation; TOC results correspond to calculated degree of dye degradation measured by means of total organic carbon after 3h of light irradiation. 71

Fig. 22. The bleaching of RB19 by Fenton's reagent in the presence of Cu/Zr modified TiO_2. 72

Fig. 23. (A)X-band and (B) Q-band EPR spectra of powdered P25/$Cu_{0.05}$ measured at 295 K or100 K. 74

Fig. 24. (A) X-band and (B) Q-band EPR spectra of powdered P25/Zr/$Cu_{0.05}$ measured at 295 K or 100 K. 75

Fig. 25. (A) X-band and (B) Q-band EPR spectra of powdered Zr modified TiO_2 measured at 295 K or 100 K. 76

Fig. 26. (A) Time course of EPR spectra (magnetic field sweep, SW = 8 mT) monitored upon continuous UV irradiation (λ_{max} = 365 nm; 16 mW cm^{-2}) of Zr modified TiO_2water suspension in the presence of spin trapping agent DMPO under air. (B) Experimental (black) and simulated (red) EPR spectrum (SW = 8 mT) obtained upon 180 s UV irradiation. Initial concentrations: c(TiO_2) = 0.33 g L^{-1}; c_0(DMPO) = 30 mM. 77

Fig. 27. Concentrations of the $^{\cdot}$DMPO-OH spin adduct obtained from the EPR spectra monitored upon 180 s exposure (UV:λ_{max} = 365 nm; λ_{max} = 385 nm; λ_{max} = 400 nm; VIS;160 klx) of water suspensions of surface modified TiO_2nanostructures in the presence of the spin trapping agent DMPO. Initial concentrations: c_0(photocatalyst) = 0.17 g /L; c_0(DMPO) = 35 mM 77

Fig. 28. EPR spectra as well as the concentrations of the $^{\cdot}$DMPO-OH obtained upon UV (λ_{max} = 365 nm; λ_{max} = 385 nm; λ_{max} = 400 nm; 16 mW cm^{-2}) and visible (160 klx) light exposure of H_2O_2 water solutions in the presence of spin trapping

agent DMPO under the air. Initial concentrations: $c_0(H_2O_2)$ = 40 μM; c_0(DMPO) = 35 mM. 79

Fig. 29. Dark-field scanning transmission electron micrographs of 0.05 mol % Cu modified TiO_2 at different magnifications: a) an agglomeration of nanoparticles; b) CuO nanoclusters on the surface of a TiO_2 nanoparticle identified by arrows. 80

Fig. 30. Normalized Cu K-edge XANES spectraof Cu and Cu/Zr modified P25 photocatalysts. Spectra of reference Cu(I) and Cu(II) compounds (crystalline Cu_2O, CuO and $Cu(OH)_2$), and Cu/Zr modified P25 photocatalyst sample calcined at 500 °C (P25/Zr/$Cu_{0.1}$_500 °C) from Fig.18 are plotted for comparison. 81

Fig. 31. Fourier transform magnitude of k^2-weighted Cu K-edge EXAFS spectra of Cu and Cu/Zr modified P25 photocatalysts, calculated in the k range of 2.5 $Å^{-1}$ – 11.0 $Å^{-1}$ and in the R range of 1.0 Å – 3.6 Å. Experiment: solid line; best-fit EXAFS model: dashed line. 82

Fig. 32. Fourier transform magnitude of k^3-weighted Zr K-edge EXAFS spectra of Zr and Cu/Zr modified P25 photocatalysts, calculated in k and R ranges of 3.0 $Å^{-1}$ –13.5 $Å^{-1}$ and 1.0 Å – 3.7 Å, respectively. Experiment: solid line; best-fit EXAFS model: dashed line. 83

Fig. 33. STEM-EDX mapping results for P25/Zr/$Cu_{0.1}$ sample. 88

Fig. 34. Surface acidity of Cu/Zr modified TiO_2. The abbreviations in the figure are: NR - neutral red, BB - bromothymol blue, MR - methyl red, MY - methyl yellow. 89

Fig. 35. Schematic presentation of beneficial Zr contribution to Zr/Cu modified mixed phase TiO_2 performance. 90

Fig. 36. The absorption spectrum of RB19 after the simulated solar and UV lights irradiation in presence of TiO_2 (P25) for 0 min. (blue), 20 or 100 min. (red). For clarity all curves were normalized to the intensity of absorption peak at 590 nm. 94

Fig. 37. The absorption spectrum of RB19 after the simulated solar irradiation in presence of P25/Cu0.05 for 0 min. (blue), 20 or 120 min. (red). For clarity all curves were normalized to the intensity of absorption peak at 590 nm. 96

Fig. 38. Normalized optical absorption spectra of diluted RB19 dye measured by UV-Vis spectrometry in 1 cm cell. 96

Fig. 39. RB19 (50 mg/L) degradation kinetic in presence of P25 or P25/Cu0.5 measured by UV Vis spectroscopy at 532 nm under the solar simulating and UV lights. The data is normalized to the absorbance registered at 0 min irradiation time. 97

Fig. 40. Absorbance (532 nm) of RB19 solution with presence of 0.06 mg/L of TiO_2 and without TiO_2. For clarity all points were normalized to the intensity of absorption peak at 590 nm. 99

Fig. 41. Calibration curve for RB19. The inset shows the relative standard deviations (RSDs%) of the data. 100

Fig. 42. Temporal behavior of the TL signal for 0.06 mg/L P25 suspended in 5 mg/L RB19 under the simulated solar light irradiation. 101

Fig. 43. Temporal evolution (a-d) of the TL signal during the simulated solar light irradiation of RB19 aqueous solution accompanied with P25 and Cu/Zr modified P25. 102

ABBREVIATIONS

Advanced oxidation processes	(AOP)
Aeroxide® Degussa P25	(P25)
American Association of Textile Chemists and Colorists	(AATCC)
Brunauer–Emmett–Teller theory	(BET)
Color Index	(C.I.)
Conduction band	(CB)
Diffuse reflectance spectroscopy	(DRS)
5,5-dimethyl-1-pyrroline *N*-oxide	(DMPO)
Dynamic light scattering	(DLS)
Electron paramagnetic resonance	(EPR)
Energy dispersive X-ray	(EDX)
Ethylenediaminetetraacetic acid	(EDTA)
Extended X-Ray Absorption Fine Structure	(EXAFS)
Full width at half maximum	(FWHM)
Hydroxyterephthalic acid	(HTPA)
International Organization for Standardization	(ISO)
International Union of Pure and Applied Chemistry	(IUPAC)
Isoelectric point	(IEP)
Metal precursor	(MP)
Methylene blue	(MB)
Polychlorinated Biphenyls	(PCBs)
Reactive Blue 19	(RB19)
Scanning transmission electron micrographs	(STEM)
Society of Dyers and Colorists	(SDC)
Specific surface area	(SSA)
Temperature oscillations	(TO)
Terephthalic acid	(TPA)
Thetraethoxysilane	(TEOS)
Thermal lens spectroscopy	(TLS)
Total organic carbon	(TOC)
Transmission electron microscopy	(TEM)
Ultraviolet light	(UV)

Visible light	(Vis)
X-ray Absorption Near Edge Structure	(XANES)
X-ray diffraction	(XRD)

INTRODUCTION

Since the industrial revolution, escalating rate of production of numerous goods has been observed. As a result, the humanity has accumulated huge amount of waste with adverse influence on nature, making the problem of environmental pollution more pronounced every year.

Natural water resources are involved in large number of production cycles. Considering limited amount of water on the Earth, it suffers from pollution to a great extent (MacKenzie 2010). In 2016, the water crisis was determined as the global risk of highest concern for people and economies for the next ten years (Koncagül et al. 2017). The widespread presence of organic chemicals with different nature poses a serious threat to the environment. When such chemicals contaminate water sources, they become hazardous. Hence, recycling and water treatment methods are the only choices for getting clean water nowadays and in the nearest future. Therefore it is advisable to develop new or to improve already existing technologies and materials that promote sufficient, safe, easy and inexpensive water purification (Gupta et al. 2012).

Photocatalysis, as a representative of advanced oxidation processes (AOP), is one of the possible alternatives for highly toxic water treatment, when the most common biological system is not effective. TiO_2 remains the most used semiconductor among numerous photoactive materials because of its inherent superior properties.

Despite the on-going progress in material chemistry of TiO_2, the solar light driven photocatalytic water purification and disinfection processes, which are stated to be environmentally friendly, remained at the level of the past decades (Byrne et al. 2011). The wide band gap (3,2 eV) which is limiting TiO_2 visible light activity and the fast electron/hole recombination rate are the main inhibitors of the progress in the field of TiO_2 photocatalysis (Mukherjee and Ray 1999), (Stasinakis 2008).

Many efforts have been made with the aim to overcome these drawbacks. One of the often used techniques is TiO_2 modification with transition metal ions (Tayade et al. 2006). The proper metal ion doping of TiO_2 is able to induce a desired spectral shifts into the visible light region of the spectra, thus enhancing the absorption capacity of a photon under the solar light (Klosek and Raftery 2002), (Su et al. 2012), (Štengl and Bakardjieva 2010). However, the visible light (Vis) response

does not necessarily imply adequate photocatalytic activity of the material, *i.e.* the quantum yield under the Vis light is often lower compared to the ultraviolet (UV) light.

Lately, TiO_2 modification with two different elements became popular approach because of the possible synergistic effect between them (Schneider et al. 2014). However, the reason of improvement in activity of TiO_2 modified with two appropriate elements is not always clear.

In this work, I attempt to examine a number of variables, which affect the photocatalytic activity of CuO and ZrO_2 modified TiO_2. Structural information and insight into the chemical states of copper and zirconium oxides loaded into TiO_2 are the fields of interest in my thesis. The results help to clarify and to understand the metal ions impact with the final goal to guide synthesis protocols in order to be more beneficial in photocatalytic mineralization of aqueous organic pollutants under the solar light. In addition, this work tackles the problem of dye application for the photocatalytic activity evaluation under simulated solar light.

1 THEORETICAL BACKGROUND

1.1 OVERALL PROBLEM STATEMENT

1.1.1 Textile processing and its global water impact

Human race cannot survive without water. Amount of water in the Earth is huge, but only small part of it is suitable for humankind needs. Discouraging fact is that the more developed becomes the human race the more water pollutions it produces.

In recent years, the increasing demand in textile products leads to fast growth of textile industry (dos Santos et al. 2007). Potential pollutants from cotton processing operations and dyestuff industrial processes are mainly organic pollutants (Pearce et al. 2003), in particular, color-causing pollutants containing large quantities of dyes. Textile dyes belong to one of the largest group of organic compounds that represent an increasing environmental danger. The textile dyes are the second-largest polluter of clean water globally after agriculture (Koncagül et al. 2017).

During the dyeing process, the dye is distributed between the solid fiber phase and the aqueous phase. After the fiber and the dye associate, the solution is depleted and the fiber has to be washed repeatedly with portions of fresh water to remove unfixed dye. Thus, during the dyeing process tons of water appears to be contaminated with dyestuff and concomitant compounds. It is estimated that about 1 - 20 % of the total world production of dyes is lost during pretreatment and dyeing processes and released in waste waters (Forgacs et al. 2004), (Herbst et al. 2005).

What are dyes? Dyes are usually water soluble organic compounds. Dyes have been used widely not only in the textile industry, but also in photographic and coating industry and photochemical applications. Depending on the constituent elements of the dye molecule (chromogenes, chromophores, and auxochromes), dyes exhibit different physical and chemical properties, such as water solubility, color, brightness, fastness, and light absorption characteristics. The transmitted light appears colored to the observer because of missing (absorbed) part of the white light (Lye 2002).

The molecules of the most dyes contain two parts: i) aromatic system (benzene ring or fused ring system) with or without substituents and ii) extensive conjugated double bond system containing unsaturated groups (chromophores). The

absorbed wavelength and intensity of color of the dye molecule can be modified by addition to the aryl ring the saturated substituents containing nonbonded electrons (-OH; $-NH_2$; -NHR; $-NR_1R_2$). These groups are known as auxochromes. In order to make the dye molecule soluble in water the sulfonic group ($-SO_3H$), the carboxylic group (-COOH) or sodium salts of these acids ($-SO_3Na$ and -COONa) can be used.

Dyes can be classified according to the chemical structure of colorant or to the method of application. The Color Index International, provided by the Society of Dyers and Colorists (SDC) and American Association of Textile Chemists and Colorists (AATCC), is a comprehensive list of known commercial dyes and pigments. Each colorant is given a Color Index (C.I.), Name and Number. For example: C.I. Reactive Blue 19 (RB19).

RB19 is anthraquinone dye and typical representative of reactive dyes. Its structure is presented in Fig. 1. Reactive dyes are of outstanding importance for the dyeing of cotton, enabling bright intense coloration with high fastness. The use of reactive dyes worldwide has approached to 178,000 tons per year (Philips 1996). The characteristic structural feature is the presence of one or more reactive groups. Vinylsulfone groups, in particular ethenyl(vinyl)sulfone ($CH_2=CHSO_2$) group, are among the most important reactive groups, being also a part of RB19 dye molecule.

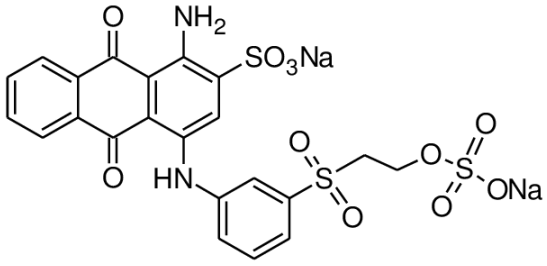

C.I. Reactive Blue 19

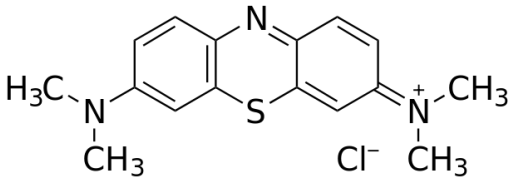

C.I. Basic Blue 9

Fig. 1. Structural formula of C.I. Reactive Blue 19 and C.I. Basic Blue 9 (Methylene blue).

Basic Blue 9, also called Methylene blue (MB), is another type of very popular dye. Methylene blue is a thiazine dye used as an anti-malarial and chemotherapeutic agent in the aquaculture industry (Burhenne et al. 2008). MB is economical and it has excellent brightness. So it is widely used in dyeing fibers, silk, wool and linen. Basic Blue 9 is used in colored paper. It is also used to make a variety of glaze and paint.

After the dyeing process, the millions of tons of effluent from industries are dumped. Annually, the amount of discharged dyes is constantly increasing. Most of the countries are separating the dye chemicals from the wastewater. This opens up the problem of dye sludge recovery and the treatment of traces of dyes in the water.

In Mexico and China, factories discharged the wastewater contaminated with dyes like indigo. This resulted in coloration of the river water (Shanker et al. 2017). Chemicals present in coloured water did not allow the light to reach the aquatic biota and the bulk of water. Thus, biological oxygen demand (BOD) was increased, the photosynthesis process was delayed and the dissolved oxygen level got reduced.

The presence of dyes in the water bodies can be not only aesthetically unpleasant because of coloring but also hazardous because of low level of degradation under the natural conditions and potential to bioaccumulation in living organisms. Moreover, possible high level of toxicity (Holkar et al. 2016) can affect the health of the local residents and people living close to the contaminated waters. Labours exposed to dye are detected with tumours, lung and cerebrovascular disease in Japan and USA at the rate of 40 times higher than general population (Shanker et al. 2017).

Lots of dyes constitute environmental hazards because of possible production of toxic intermediates as degradation products. For example, nitrobenzene, diaminobenzene, stilbene, aminonaphthol, benzidine and quaternary amines substructures in the dye molecule can causecarcinogenicity and toxicity problems (Epling and Lin 2002). In order to ensure a safe water supply, dye-containing wastewater from industries needs to be treated and its discharge controlled.

Bearing in mind all mentioned above, it is reasonable to pay more attention for developing new or improving already existing technologies for water purification in general and from dyestuff in particular.

1.1.2 Photocatalysis as an effective technique for water purification

As international environmental standards are becoming more stringent (ISO 14001, March 2016), the technological systems for the removal of organic pollutants from water have to be improved. Among already existing methods for purification of dye polluted effluents are the physical methods such as adsorption (Kausar et al. 2018), the biological methods (Banat et al. 1996), (Gonçalves et al. 2000), and the chemical methods (Punzi et al. 2015). Adsorption is based on the organic pollutant uptake by highly porous inorganic or organic matrixes (Bhatnagar and Sillanpää 2010). This technique is effective in terms of extracting pollutants, but it does not solve a problem of pollutants recycling. Modern and fast developing microbiological or enzymatic decomposition involves the cultivation of colonies of microorganisms against hazardous organics (Pearce et al. 2003), (dos Santos et al. 2007), (Dellamatrice et al. 2017). This technique is very promising, but it deals with live organisms, so it meets list of requirements and is not appropriate for some specific and toxic pollutants. Many of dyes are resistant to biological degradation because of the high degree of aromatic compounds (Carliell et al. 1996). Large number of publications indicates that advanced oxidation processes (AOP) may be an alternative for the oxidation of toxic organic compounds from wastewater (Klavarioti et al. 2009). Degradation of commercial reactive dyestuff by AOP is frequently reported as efficient and promising process (Akpan and Hameed 2009), (Akpan and Hameed 2009), (Konstantinou and Albanis 2004), (Rauf et al. 2011), (Zangeneh et al. 2015), (Reza et al. 2015), (Akpan et al. 2015).

Photocatalysis is widely studied AOP and it demonstrates potential applicability for wastewaters treatment because of the high theoretical probability to result in total non-selective destruction of organic compounds. In this action, hazardous organic compounds may transform to simple inorganic ones, such as CO_2, H_2O, inorganic anions and cations. This performance is attributed to the active species formed during the photocatalytic process (Carp et al. 2004).

The mechanism of photocatalysis derives from redox/charge transfer processes due to the electronic structure of the catalytic material (semiconductor) involved in the photocatalytic action (Linsebigler et al. 1995). The relevant energy levels for semiconductor electron transfer are the top of the valence band (VB) and the bottom of the conduction band (CB) and formed band gap in between.

The photons with energy higher than band gap excite an electron from the VB of semiconductor and promote it to the CB, leaving the active hole behind. The photo-excited electrons and holes can then migrate to the surface of semiconductor and take part in the photocatalytic action.

The common proposed mechanism of photocatalysis is as follows (Sirés and Brillas 2012):

1. Absorption of efficient photons by the photocatalyst (semiconductor):

$$Semiconductor + hv \rightarrow e_{CB}^{-} + h_{VB}^{+} \quad (1)$$

2. Oxygen reduction:

$$(O_2)_{ads} + e_{CB}^{-} \rightarrow O_2^{\cdot -} \quad (2)$$

3. Production of $HO^{\cdot}$ radicals:

$$(H_2O \leftrightarrow H^+ + OH^-)_{ads} + h_{VB}^{+} \rightarrow H^+ + HO^{\cdot} \quad (3)$$

4. Neutralization of $O_2^{\cdot -}$

$$O_2^{\cdot -} + H^+ \rightarrow HO_2^{\cdot} \quad (4)$$

5. Transient hydrogen peroxide appearance:

$$2HO_2^{\cdot} \rightarrow H_2O_2 + O_2 \quad (5)$$

6. H_2O_2 decomposition:

$$H_2O_2 + O_2^{\cdot -} \rightarrow HO^{\cdot} + HO^- \quad (6)$$

7. H_2O_2 decomposition (photodissociation):

$$H_2O_2 \xrightarrow{hv} 2HO^{\cdot} \quad (7)$$

8. Organic reactant oxidation:

$$R + HO^{\cdot} \rightarrow degradation\ products \quad (8)$$

9. Direct oxidation through reaction with hole:

$$R + h_{VB}^{+} \rightarrow degradation\ products \quad (9)$$

There are numerous argumentations in the scientific literature about the role of each active species mediated by irradiated TiO_2. However, there is no integrity of opinion concerning this problem. It is still an open question in regards to the most relevant process contributing to the photooxidation of organic pollutants. Many authors argue that $HO^{\cdot}$ radicals formed in the scheme proposed above are the primary oxidants in the photocatalytic process (Al-Ekabi et al. 1989). This statement is mainly based on hydroxylated products formed during pollutants degradation

reactions. Another significant support to this mechanism is given by EPR analysis (Jaeger and Bard 2005), confirming that the $HO^{\cdot}$ radical is the most abundant radical formed during the irradiation of TiO_2.

On the other hand, literature reports about very low probability of $HO^{\cdot}$ radicals implication in the photocatalytic oxidation also exist. It was demonstrated that no oxygen containing species are formed when ethyne and ethene are photohydrogenated on the surface of TiO_2 (Boonstra and Mutsaers 1975a). The same authors in another work concluded that the Ti_s-$O^{\cdot}$ radical formed at the surface of TiO_2 is the one governing the photocatalytic reaction (Boonstra and Mutsaers 1975b).

In the past decades charge carrier transfers on the solid/liquid interface of TiO_2 got considerable attention, which led to deeper understanding of photocatalytic process. In this context, recent finding (Salvador 2011) made the reaction of direct water oxidation (equations (3), in the proposed scheme), which was a long time considered as the main process responsible for the photocatalytic oxidation of organic substances, questionable. Thermodynamic and kinetic constrains were shown that make the reaction of direct water oxidation on rutile surface unlikely to happen. This discovery opens the possibility to the new pathways of photocatalytic reaction. In particular, generation of reactive species by hole trapping was considered as well as direct hole participation in the photocatalytic reactions.

Pulse radiolysis study (Lawless et al. 2005) pointed out that the species produced by the reaction of $HO^{\cdot}$ radicals with TiO_2 surface are essentially identical with the trapped holes on the surface of TiO_2. If this is the case, all the observations (hydroxylated intermediates and H_2O_2 formation) which previously led to the suggestion of $HO^{\cdot}$ radicals oxidation can occur via reactions of these surface species.

The difference in the mechanisms of active species formation on the distinct TiO_2 phases was proposed by some authors (Kakuma et al. 2015). They concluded, that for anatase the mechanism of $HO^{\cdot}$ radicals formation originates from the trapped holes while for rutile Ti-peroxo site plays a role of catalyst for $HO^{\cdot}$ radicals generation from water.

If the $HO^{\cdot}$ radicals are surface-bounded or they are able to diffuse out of the surface in the bulk of the suspension is another concern among the scientists in the area. The impact of free $HO^{\cdot}$ radicals as a consequence of equations (3), (6) and (7)

to overall photocatalytic reaction is still an open question.

These controversial, but solid arguments discussed above, however, may also suggest that every organic substrate undergoes transformation assisted with irradiated TiO_2 by its own pathway with involvement and significance of different active species for each case separately. Then, unification of the mechanism of TiO_2 assisted organic compounds degradation is not possible.

In this work we attempt to stand by the essential similarity between active species formed by surface-bonded $HO^{\cdot}$ radicals and holes trapped on the surface and their major role in the degradation of pollutants. However, the possibility of diffusion of some $HO^{\cdot}$ radicals out of the surface and their contribution to the overall photocatalytic performance of the material also exists and has to be checked.

The photo-induced holes can take part in two different types of reactions. First, if the redox potential of the aqueous couple is higher in energy than the VB edge, electrons will be transferred from the aqueous donor to fill the hole in the VB, thereby oxidizing the aqueous electron donor. As photocatalysts, semiconducting materials can photo-oxidize a wide range of compounds. Environmentally important reactions include photo-oxidation of phenol (Palmisano et al. 1988), PCBs (Pagni and Sigman 1999), insecticides (Harada et al. 1990), dyes (Akpan et al. 2015). Second, if the standard potential for anodic decomposition of the semiconductor is higher in energy, the hole can also cause oxidation of the semiconductor. Thus, in aqueous solutions, the photo-electrochemical stability of a semiconductor is determined by the standard potential for anodic decomposition relative to the oxidation potential of water. These two types of photoelectron transfer associated with a VB energy position are crucial for determining the activity and stability of the semiconducting materials in aqueous environment.

Contrary, the photo exited electrons take part in the reduction reactions. To reduce compound, one needs a semiconductor with a conduction band edge higher than the reduction potential of the compound. Semiconductors with conduction band edges higher than that of the oxygen reduction potential ($O_2/O_2^{\cdot -}$) can facilitate the photochemical reaction by producing additional amount of active species in an aqueous solution. However, it can be the case when the semiconductor with higher CB energy does not catalyze the photoreduction of compounds with lower reduction potential, but catalyzes energetically less-favorable reactions (Yanagida et al. 1990).

The rates of electron transfer reactions generally increase with increase in the driving force (*i.e.*, the energy difference between electron donor and acceptor levels), however a large difference in energy between donor and acceptor levels results in a slow electron transfer. This phenomenon has been described as the "inverted region effect" (Gould et al. 1990).

Among the numerous photoactive semiconductors, the leading position holds TiO_2. It complies with major requirements for efficient photocalysts: chemical and biological inertness and photostability, relatively low cost, low toxicity level, adequate conversion values (Hoffmann et al. 1995), (Ollis at al. 2000), (Fujishima et al. 2000), (Kubacka et al. 2012).

1.1.3 Basics about TiO_2 as a photocatalyst

TiO_2 is well established material which is used in different areas, such as a white pigment in paint, food, cosmetics and paper coloring, UV absorber in sunscreens. All these applications deal with size range of TiO_2 particles from hundreds of nanometers till micrometers. On the contrary, its nanosized particles utilization is focused on its electronic properties as a semiconductor (Fujishima et al. 2000).

1.1.3.1 TiO_2 crystal polymorphs

Since 1977, when cyanide in water was decomposed by titania (Frank and Bard 1977), increasing interest to photo-oxidative degradation by titania catalyst for environmental applications has been registered. An important factor which determines the scope of use of TiO_2 as a photocatalyst is its crystal structure. There are three main crystal polymorphs of TiO_2: anatase (tetragonal), rutile (tetragonal), brookite (orthorhombic) (Carp et al. 2004). The Ti cations at anatase, rutile and brookite have coordination number of 6, so they are surrounded by an octahedron of 6 oxygen atoms. The three crystalstructures are different by the terms of distortion and assembly patterns of each octahedral arrangement: in anatase octahedra are connected by the vertices, in rutile by the edges, and in brookite by both, vertices and edges (Fig. 2).

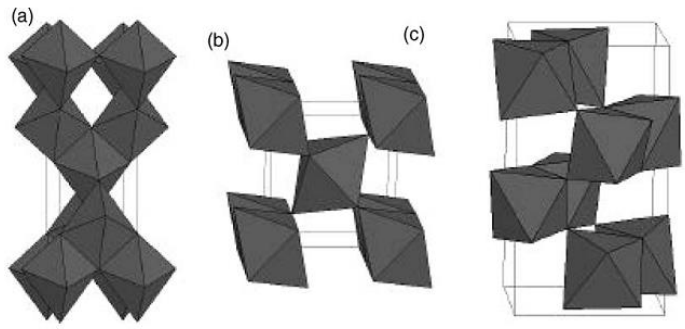

Fig.2. Crystal structure of (a) anatase, (b) rutile, (c) brookite(Carp et al. 2004).

The most thermodynamically stable phase is rutile. Anatase and brookite, which are stable at low temperatures, transform to rutile via heat treatment at temperatures higher than 600 °C. Proper transition metal doping can stabilize anatase and brookite at higher temperatures (Hanaor and Sorrell 2011).

Anatase and rutile, both are commonly used as photocatalysts. By examination the photocatalytic activity of 35 differently prepared TiO_2 photocatalysts it was shown that anatase is more active than rutile (Prieto-Mahaney et al. 2009). Different theories and hypotheses were proposed to explain higher activity of anatase: a) higher number of surface OH group (Sclafani and Herrmann 1996); b) higher potential of conduction band (Prieto-Mahaney et al. 2009); c) the longer liftime of photoinduced electron and hole pair due to the indirect band gap (Xu et al. 2011); d) special surface properties (Kakuma et al. 2015). Additionally, it was shown, that the charge carriers can be excited deeper in the bulk in case of anatase, thereby making more contribution for surface reaction (Luttrell et al. 2014). However, the works where rutile shows higher photocatalytic activity compared to anatase also exist (Sun et al. 2003), (Andersson et al. 2002).

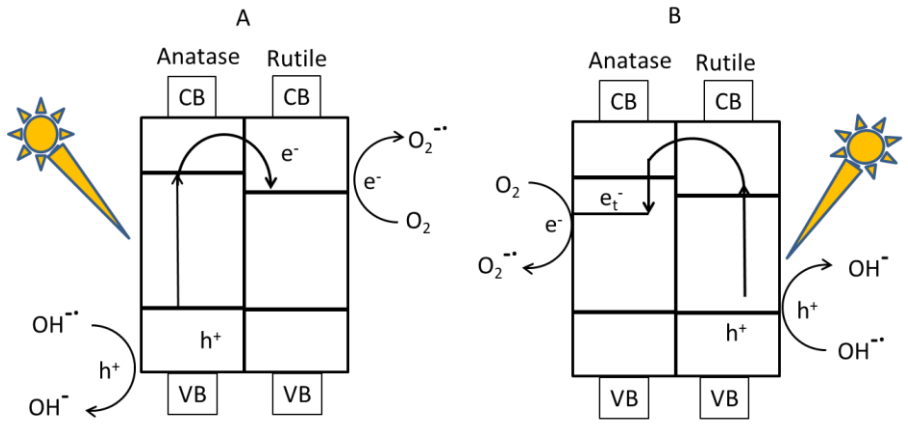

Fig. 3. The mechanism of charge separation on P25. (A) Model of P25 activity where charge separation occurs on anatase and rutile acts as an electron sink (Bickley et al. 1991). (B) Proposed model of a rutile antenna and subsequent charge separation (Hurum et al. 2003).

Compared to pure phases, the mixed-phase TiO_2 materials are often more active (Banerjee et al. 2006), (Baiju et al. 2009). Aeroxide® Degussa P25 (P25) is known as a mixed phase TiO_2 with high UV-light activity. It contains anatase and rutile phases in a ratio 3:1. It is declared that the synergistic effect between the anatase and rutile is responsible for the high reactivity of P25. Lately it was shown that it is the interphase charge transfer, which is responsible for the separating of electrons from holes. Surprisingly, there is still no consensus about the synergetic effect in general (Ohtani et al. 2010) and the charge transfer mechanism, responsible for synergy, in particular (Kumar and Devi 2011). Two different interfacial charge transfer mechanisms in the P25 were proposed by Bickley et al. (Bickley et al. 1991) and Hurum et al. (Hurum et al. 2003). The schematic pattern of completely distinct mechanisms is presented in Fig.3. The electron transfer appears to be directed from anatase to rutile in the one case (Bickley et al. 1991) and opposite direction in the other case (Hurum et al. 2003).

It is interesting to note that the mixture of anatase and rutile facilitates only the transfer of electron without the promotion of hole movement and distribution because the VB energy is the same in both anatase and rutile phases. Lately, the synergistic effect has been satisfactorily explained using a model based on the band-gap variation in the connected nanocrystallites as a function of the size distribution and the phases involved (Zachariah et al. 2008). It was shown, that the particle size

determines also relative phase stability. Anatase is the most thermodynamically stable at sizes less than 11 nm, brookite – between 11 and 35 nm, and rutile – bigger than 35 nm (Carp et al. 2004).

1.1.3.2 The size of TiO_2 particles

The photocatalytic degradation of organic pollutants in water occurs on the surface of TiO_2, thus its surface properties are highly important and influence the photocatalytic performance. High surface area can be an advantage for the photocatalyst due to bigger numbers of available surface sites. Specific surface area of material drastically grows with decreasing particles size, this fact led to photocatalytic materials fast shift towards the nano sizes. Additional advantage of the particles size lowering is that the charge carrier path to the surface becomes shorter in smaller particles which can positively influence the photocatalytic performance (Luttrell et al. 2014). From the other hand band bending is reduced with the particles size lowering (Pan et al. 2019), which is expected to negatively influence the charge separation of photocatalyst.

The nanopowder photocatalysts suspensions perform high efficiency in degrading organic pollutants in water due to its high surface area. However, an additional step of post separation or filtration after TiO_2 treatment is needed when the slurry or suspension system is used. This process is necessary for several reasons: to prevent the photocatalyst loss and to avoid the water contamination with nanosized TiO_2 particles (Chong et al. 2010). Membranes, filters and pH control procedure which are used for precise water and nanoparticles separation are expensive and do not provide complete removal of particles (Dong et al. 2015).

Besides, the TiO_2 nanoparticles in water solution may aggregate due to the instability of the nanosized particles (Dong et al. 2015). Aggregation can negatively influence the light incidence as well as it lowers the number of available active centers consequently reducing the catalytic activity of material (Mallakpour and Nikkhoo 2014). However, it must be taken into account that the photocatalytic activity is dependent of specific optical properties of material as well as experimental conditions and it may happen that the smaller particles scatter more light compared to larger ones (Minero and Vione 2006). Recently, because of high influence of agglomeration to the optical properties of solution it was recommended to evaluate

the aggregation level of photoactive particles before the photocatalytic tests (Pellegrino F et al. 2017). It was shown that deaggregation strongly increases light absorption, which is due to the low penetration depth of the light inside the agglomerated particles.

It is important to mention, that finite diminishment can be applied for getting enhancement in photoactivity. For oxide materials the limit is about 10 nm. After reaching this limit the degree of crystallinity becomes lower, which can increase recombination rate (Choi et al. 1994). The quantum size effect is also possible to become pronounced (Hoffmann et al. 1995).

All the reasons mentioned above led researches to the quest for suspended nanosized powders application alternatives. As an alternative solution, the immobilization of photocatalyst on the inert substrate can be offered. TiO_2 can be immobilized on different substrates such as glass, fibers, stainless steel, sand *etc*. To prevent leaching or detachment of nanoparticles from the layers that may otherwise negatively affect surrounding environment, binder material is needed. On the other hand, the immobilization leads to relative lowering of the photocatalytic efficiency.

Nowadays, Aeroxide® Degussa P25 in a powder form is the most applied and known TiO_2 photocatalyst because of its high reactivity. It is used as a standard reference for water treatment under the different conditions. Accordingly, it is clear, that anatase and rutile mixture as well as particle size distribution are playing significant role in the photocatalytic activity of TiO_2. It must be stressed, that all the difficulties and uncertainties related to TiO_2 application mentioned above are not the comprehensive list. There are other drawbacks, which are limiting its wide application and must be overcome for its widespread use.

1.1.4. Shortcoming and weakness of TiO_2

Photocatalytic oxidation with TiO_2 is one of the AOP for the rapid degradation of organic pollutants in water. TiO_2 can mineralize big number of organic pollutants including resistant pesticides, herbicides and dyes. To develop its photocatalytic properties, TiO_2 demands energy input by photons with energy greater than its band gap.

The Sun was considered as an abundant and the most fundamental sustainable energy source for humankind. Utilization of solar light for the TiO_2 photocatalytic

process is highly desirable from economic and environmental points of view. The solar light consists of ultraviolet (200 - 400 nm), visible (400 - 800 nm) and infrared (> 800 nm) irradiation with share of each 5 %, 43 % and 52 %, respectively. Unfortunately, the band gap of TiO_2 (~ 3.2 eV for anatase and brookite, ~ 3.0 eV for rutile) requires photons with energy corresponding to UV irradiation region, which accounts for only 5 % of solar spectrum. Development of visible light TiO_2 photocatalysis has become one of the most important topics because of much higher contribution of visible light irradiation to the solar spectrum (Stasinakis 2008).

Designing, fabricating, and tailoring the physicochemical and optical properties of titania is indispensable to utilize a large fraction of the solar spectrum and to realize the indoor and sustainable applications of this photocatalyst. Modification by various strategies such as coupling with a narrow band gap semiconductor, metal ion/nonmetal ion doping, co-doping with two or more foreign ions, surface sensitization by organic dyes or metal complexes and so on were explored to extend the TiO_2 light absorption to visible light region. It was also determined that TiO_2 composites with second material, which is either a hole or an electron sink can further increase catalytic efficiency of material.

Despite the achievement of desired spectral shift towards the visible light region, quantum yield of electronic process under visible light in doped materials is much lower than under UV (Choi et al. 1994). This fact can be referred to formation of new crystal defects and generation of recombination centers by doping. Considering this, the TiO_2 surface modification process is more attractive compared to doping (Šuligoj et al. 2018). In this case, visible light sensitivity is achieved by the charge transfer process of excited electrons from the one semiconductor to another (Irie et al. 2009), (Nolan et al. 2012), (Liu et al. 2014), hereby improving charge separation properties.

1.2. DETAILED UNDERSTANDING OF THE RESEARCH WORK ISSUE

1.2.1 Different techniques for TiO_2 modification

Keeping in mind the profitable price and environmental sustainability of the photocatalytic water treatment process (Anastas and Eghbali 2010), it is desired to tune the absorption edge of TiO_2 photocatalysts to visible range of the solar spectrum (Kubacka et al. 2012). The technique, which allows tailoring light absorption

properties, but not disturbing the band gap can be applicable. In this case, the visible-light response can be induced without changes in a crystal structure. The visible light sensitivity is achieved by the charge transfer process of excited TiO_2 electrons to the modifier (Irie et al. 2009), hereby improving electron/hole recombination properties.

There has been great interest for modification of TiO_2 with the second material (Kubacka et al. 2012), (Petronella et al. 2017). Several approaches of modification can be used: solid-state reactions, gas phase methods and solution routes. The solution route reactions (also called wet chemical methods) belong to bottom-up methods which means self-assembly of atoms or molecules to the nanoparticles. These methods have the advantage of control over the stoichiometry, producing homogeneous materials, relatively low synthesis temperature, allowing formation of complex shapes, and preparation of composite materials. The most common methods and their short descriptions are listed below.

- Sol-gel technology. This method is based on hydrolysis and condensation of metal alkoxides or inorganic metal precursors and leads to formation of sol or gel or precipitates. It can be used for the synthesis of thin films, powders, and membranes. There are many advantages of this method: purity, homogeneity, stoichiometry control over the composition of obtained materials. In addition, it is flexible in introducing dopants in large concentrations and allows easy processing. After sol-gel, the thermal treatment (usually 450 – 600 °C) is needed to remove the organic part and to crystallize either anatase or rutile TiO_2. Variety of research was made based on sol-gel technique (Kete et al. 2014), (Hernández-Alonso et al. 2006), (López and Gómez 2012), (Ilkhechi et al. 2015b), (Choudhury et al. 2013).
- Microemulsion. Microemulsion is thermodynamically stable, optically isotopic solution of two immiscible liquids. Water in oil or reverse microemulsion technique can be utilized. The stabilization of microemulsion happens with the help of interfacial film of surfactant. The surfactant molecule generally has a polar (hydrophilic) head and a long-chained aliphatic (hydrophobic) tail. These molecules self-organize in a way that they reduce the interfacial tension between two liquids with different nature. Notably, this technique is used together with sol-gel methods for hydrolysis of metal alkoxides (Andersson et al. 2002).
- Solvothermal. These methods can be described as chemical reactions in aqueous (hydrothermal) (Xing et al. 2011, (Peng et al. 2008), (Wang et al. 2010) or

organic (solvothermal) media (Su et al. 2012) under self-produced pressures at relatively low temperatures. For performing the experiment, solvothermal reactor is needed. The solvothermal treatment could be employed to control particle size, morphology and crystallinity by regulating the solution composition, reaction temperature, pressure, solvent properties, additives, and ageing time.

- Wet impregnation. This method allows loading the chemical species on the surface of particles. In description for impregnation offered by IUPAC it is written: "Impregnation consists in contacting a solid with a liquid containing the components to be deposited on the surface" (Haber et al. 1995). The required amounts of components are introduced in the appropriate volume of liquid with calculated concentration of target molecules, which have to be loaded on the surface. TiO_2 modified with Ag, Cu, Co, Fe, Ni were obtained by wet impregnation method (Tayade et al. 2006). The authors demonstrated relations between the ionic radius and work function of impregnated metals with photocatalytic activity of TiO_2 for nitrobenzene and acetophenone degradation under UV light. Results of another work, in which this technique was applied for obtaining Cr, Co, Cu, Fe, Mo, W, V modified TiO_2 and 4-nitrophenol degradation, suggest complexity in linkages between the specific properties of the powder and its photocatalytic activity (Di Paola et al. 2002).
- Solution combustion. The synthesis (hyperbolic reaction) involves a very rapid heating because of exothermal reaction between the components of solution containing redox mixture. All the components of redox mixture must be water soluble. Combustion synthesis allows obtaining highly crystalline, fine and large surface area particles. The initial temperature of reaction depends on the type of fuel that is used. The temperature of reaction reaches above 650 °C for a very short time (about 1-5 min) which made anatase to rutile transition almost impossible. Examples of applying such kind of technique for TiO_2 obtaining and modification can be found in several publications (Sivalingam et al. 2003),(Nagaveni et al. 2004), (Saito et al. 2015), (Chung and Wang 2012).

A huge number of techniques and chemicals were used for TiO_2 modification in recent years (Kumar and Devi, 2011), (Kubacka, Fernández-García and Colón, 2012), (Petronella et al., 2017). Good results in increasing TiO_2 efficiency as a photocatalyst were obtained with coupling it with Au (Li et al. 2007), Pd, Pt

(Sakthivel et al. 2004), (Paulauskas et al. 2013) adopted as dopants and surface modifiers.

1.2.2 Advantages of TiO_2 modification with the second material

The photocatalytic activity of TiO_2 is shown to be dependent on crystal phase, surface area, uncoordinated surface sites, defects in the lattice *etc.* The TiO_2 morphology control via composite materials synthesis has allowed fine tuning of many of these properties. Additionally, TiO_2 composite structures can create and tune mid-band-gap electronic states, which can alter charge migration.

In most semiconductors, all electronic levels in the VB are occupied where as the levels in the CB are empty. Hence, the highest occupied electronic level coincides with the top of the VB. The energy of the VB edge is a measure of the ionization potential of the bulk material. The lowest unoccupied electronic level in most semiconductors coincides with the bottom of the CB, where the band edge energy is a measure of the electron affinity of the compound. The Fermi level represents the chemical potential of electrons in a semiconductor. In essence, the Fermi level is the absolute electronegativity of a intrinsic semiconductor, the value, which corresponds to the energy halfway between the CB and VB edges.

For non-transition metal oxides (ZnO, PbO, CdO, SnO_2 etc.), the bottom of the CB is primarily from the metal s orbitals, where as the top of the VB is derived primarily from oxygen 2p orbitals. The top of the VB of most oxides of transition metals with low d electron occupancy (TiO_2, ZrO_2, WO_3) is also derived from oxygen 2p orbitals, but the CB edge for those oxides is generally derived from metal d orbitals (Yong and Schoonen 2000). These semiconductors usually have large band gaps. Their VB edges are situated at energy levels close to the absolute electronegativity of oxygen (-7.54 eV), and much lower than the oxidation potential of water (redox potential of O_2/H_2O couple). The CB edges of these semiconductors are close to the reduction potential of water (redox potential of H_2/H^+ couple). Hence, electrons in the CB and holes in the VB are very high in the reducing and oxidizing power, respectively.

For oxides of transition metals with high d electron occupancy, metal d states are present in both valence band edges and conduction band edges. As a result, the band structures become complicated and band gaps are generally smaller. For CuO,

the top of the VB is derived from the Cu 3d orbitals, whereas the bottom of CB is derived from the Cu 4s orbitals.

Incorporation of impurities in the structure of TiO_2 semiconductor leads to the presence of electron acceptor state levels and/or donor state levels within the band gap. The charge transfer from one semiconductor to another with suitable band edge positions that is thermodynamically favorable can increase the lifetime of the charge carriers promoting the interfacial charge transfer and catalytic efficiency. The presence of donor or acceptor state levels changes the position of Fermi level, which lies just above VB edge for p-type semiconductors (acceptor states) and just below CB edge for n-type semiconductors (donor states) (Yong and Schoonen 2000).

Figure 4a shows a general model for TiO_2 photocatalysis where electron−hole pair is produced by the adsorbed light. Formed charge migrates to the surface of the particle and redox reaction occurs. Charge separation can be enhanced by creation of surface defects where electrons and holes can be trapped to prevent recombination. Figure 4b shows an improved case utilizing a TiO_2 composite heterojunction. A structure with a narrower band gap can utilize visible light to produce an electron−hole pair. Assuming a favorable band offset, the electron can migrate to the TiO_2, while the hole is trapped in the second material. Redox reactions in this case occur at the separate surfaces. A TiO_2 composite structure can be rationally designed in order to produce a favorable band offset and band positions in order to develop a catalyst for the needs of specific reactions (Dahl et al. 2014).

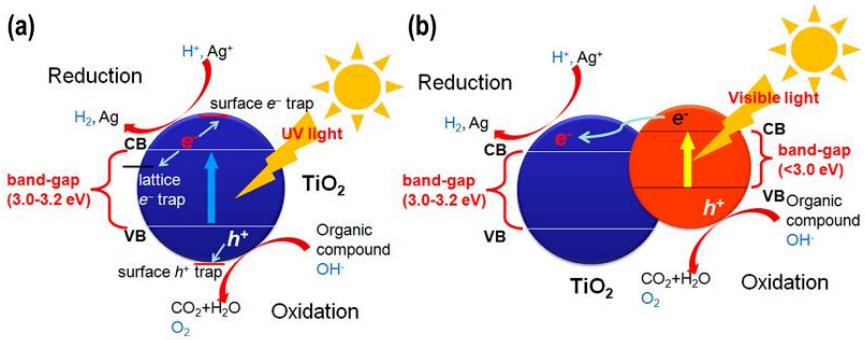

Fig. 4. (a) General model of TiO_2 photocatalysis. (b) TiO_2 modified structure exhibiting TiO_2 composite heterojunction (Dahl et al. 2014).

Composite structures can yield other benefits such as ability to tune the surface properties, *i.e.*, acidity/basicity or open coordination sites. Some mixed metal

oxide/TiO_2 composites are beneficial for stabilization of thermal catalysts or stabilization of nanoparticles against sintering or aggregation.

1.2.2 Copper oxide as TiO_2 modifier

As it is mentioned above, the efficient applicability of TiO_2 for environmental purposes, which is restricted by its limited activity under the solar light, is strongly connected to TiO_2 visible light sensitivity. In the context of TiO_2 limiting application under the solar light, Cu^{2+} ions and CuO have attracted much attention as promising surface modifiers (Li et al. 2008), (Janczarek and Kowalska 2017), (Irie et al. 2008), (Irie et al. 2009), (Helaïli et al. 2009) because they facilitate the visible light absorption.

Copper oxides have been extensively studied in the composition with TiO_2 due to their p-type configuration. Narrow band gaps of both copper oxides (~ 1.4 and ~ 2.2 eV for CuO and Cu_2O, respectively) make them interesting materials for visible light utilization.The visible light activation of Ti centers by copper ions was reported in 2005 (Lin and Frei 2005a). Positive effect of copper ions as surface modifiers is described in several papers. Charge separation properties of copper ions modified materials were claimed to be better (Chiang et al. 2002), (Li et al. 2008), (Sahu and Biswas 2011). Existence of optimal concentration (0.1 %) of CuO deposited by precipitation method on the surface of rutile nanoparticles was shown for methylene blue (MB) degradation (Li et al. 2008). It was discussed, that loading of relatively high concentration of copper leads to CuO clusters formation and results in reduced photocatalytic activity because of additional charge recombination centers appearance. In contrast, Cu^{2+} substitution sites (Ti-O-Cu linkages) are formed when very low copper concentration (lower than 0.1 %) is applied (Čižmar et al. 2018). Substitution sites contribute to enhancement of photocatalytic efficiency. Also, influence of surface CuO species on TiO_2 photocatalytic activity was studied in terms of surface photovoltage spectroscopy as well as degradation of Rhodamine B with help of copper modified TiO_2 obtained by sol-gel technology (Xin et al. 2008). The increase of photocatalytic ability of surface modified TiO_2 with 0.06 % of copper referred to formation of extra electron traps, while at higher copper loadings CuO can act as recombination centers (Choudhury et al. 2013) and can even cover the active centers on the surface of TiO_2.

There is no integrity about the optimal concentration of Cu loading, but there is a solid opinion, that at concentrations higher than 0.1% the negative effect is observed. Sometimes the concentrations lower than 0.1% (0.06%) are discussed like beneficial, however the steps of loaded amount of Cu can be different which may influence the result. Moreover, the methods of Cu loading may differ from case to case, which may certainly affect the observed results. In order to determine the optimal concentration for the specific loading procedure, the loading with narrow steps (0.01%) must be performed.

There were attempts to describe the phenomenon of photocatalytic enhancement by mechanism of interfacial charge transfer of electrons involving Cu(II) to Cu(I) reduction (Irie et al. 2009), (Liu et al. 2014). Irie with co-authors concluded, that Cu(II) ions on thesurface of TiO_2 exist as amorphous CuO-like clusters and mediate the reduction of oxygen molecules through a multielectron pathway. Thus, in order to improve the efficiency of interfacial charge transfer, Cu(II) ions should be grafted as multiatomic Cu(II) clusters. Liu *et al*. (Liu et al. 2014) used the idea for further improving of photocatalytic activity, by adding also hole-trapping agent.

According to the work (Irie et al. 2009), the visible light sensitivity and enhancement of TiO_2 photocatalytic activity by Cu^{2+} modification can be explained by formation of the mid-level Cu3d states. The mid-level states enable the transition of electrons from the valence band of TiO_2 to the empty CuO states (visible light sensitivity) leading to enhanced electron/hole separation (Nolan et al. 2012), (Liu et al. 2014). However, the benefits of modifying TiO_2 with copper containing species are not obvious. The efficiency of pollutant degradation under Vis and UV light depends strongly on the amount of the grafted species (Čižmar et al. 2018), (Yuliati et al. 2016). For example, the degradation of 2-naphthol and p-cresol by TiO_2 modified with a small amount of CuO increases, however it decreases with higher amount of CuO loaded (Jin et al. 2013).

This issue, concerning the loaded amount of CuO species and photocatalytic activity was thoroughly discussed by (Jin et al. 2013). The effect that CuO modification has on the energy levels (valence band (VB) and conduction band (CB)) of rutile (110) and anatase (001) TiO_2 surfaces was shown by density functional theory and spectroscopic experiments (Jin et al. 2013). The energy of the

VB maximum of photocatalyst is important because it determines the ability of the photo generated holes to oxidize organic pollutants (Zawadzki et al. 2012). The VB energy increase is leading to formation of holes with weakened oxidative power and as a consequence to lower photocatalytic activity. It was shown that the surface modification of rutile (110) and anatase (001) by the CuO nanoclusters can cause a significant change in the TiO_2 energy bands (Jin et al. 2013). It was clear that the change at the VB strongly depends on CuO loading, expressed by means of the elementary $(CuO)_n$ species in the surface supercell utilized for modeling, with n = 1, 2, 4 (Jin et al. 2013). The study concluded that at low and high CuO loading two different mechanisms of organic pollutant degradation are possible. The major effect of the CuO modification at low copper loading (n = 1) is the excitation of the electrons from the TiO_2 VB to the unoccupied Cu3d levels as suggested by (Irie et al. 2009). Whereas at higher copper loading (n = 2, 4) the upward shift of the VB edge and the excitation from the surface CuO to the CB of TiO_2 – reverse charge localization – is likely dominant. Moreover, it was hypothesized that the type of TiO_2 crystal phase, on which CuO clusters are formed, plays a role in the activity of CuO modified TiO_2. The upward shift of the VB edge at n = 2, 4 for anatase is not as significant as it is for modified rutile (Jin et al. 2013), therefore the reverse charge localization mechanism is not obvious in this case and, probably, it is shifted towards higher copper loading. The schematic pattern of the reverse charge localization mechanism is presented in Fig. 5.

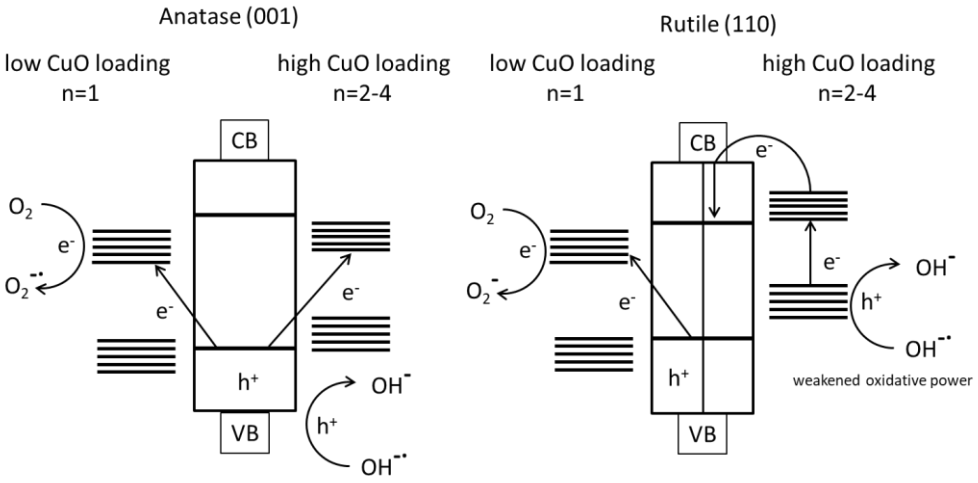

Fig. 5. The schematic pattern of the reverse charge localization mechanism on CuO modified rutile TiO_2.

1.2.3 Zirconium oxide as TiO_2 modifier

Another well-known additive to TiO_2 is zirconium. ZrO_2 can act as a photocatalyst itself (Karunakaran and Senthilvelan 2005). It has been shown that Zr ions addition to the TiO_2 matrix leads to increased photocatalytic activity in comparison with pure titania (Zorn et al. 1999), (Zorn et al. 2000). Successful utilization of solution combustion technique was applied for TiO_2 – ZrO_2 preparation (Polisetti et al. 2011). Improvement of durability of Zr doped materials is a feasible opportunity as well. It is postulated that because of great chemical and mechanical stability ZrO_2 can be used even for chromatography columns, requested excellent stability of the material (Nawrocki et al. 1993). Scratch resistance and durability of deposited layers of Zr modified TiO_2 was shown (Vodišek et al. 2016). However, due to the wide band gap of ZrO_2 (5.0 eV) it does not facilitate the visible light absorption. It was shown that Zr doping of bulk TiO_2 does not improve the band gap dependent electronic properties, such as electronic conductivity or photocatalytic properties (Lippens et al. 2008). The benefits of using Zr are claimed to increasing of surface acidity, adsorption ability and active surface area of TiO_2 (Xianzhi et al. 1996), (Venkatachalam et al. 2007). To the best of our knowledge, zirconia is not common for surface modification of TiO_2. Nevertheless, ZrO_2 was adopted in this way, when TiO_2 was used as a support for cobalt catalyst (Jongsomjit et al. 2012). The applying of Zr resulted in increasing of Co-TiO_2 catalytic activity for hydrogenation of carbon monoxide, apparently, by promoting chemisorption ability of the catalyst.

1.2.4 Multicomponent TiO_2 modification

Recently, to further improve the properties of TiO_2 and to enable more effective use of sunlight in visible part of the spectrum, technique of multicomponent TiO_2 modification has been employed (Schneider et al. 2014). One of the popular approaches of TiO_2 modification is its modification with two different elements such as B/Fe (Khan and O'Hare 2002), Sn/Pt, Al/Pt (Paulauskas et al. 2013), Fe/Ho (Wang et al. 2010), Zr/Mn(Pliekhov et al. 2016). The addition of two different species of metal oxides on the TiO_2 surface opens up new possibilities in the modification of photocatalysts. An additional positive effectis possible if two different transition metal elements are co-loaded to TiO_2 (Kontapakdee et al. 2007).

However, it is not always true that two elements are better than one. It should be appropriate mixture and amount of coupled elements. The improvement in activity of TiO_2 modified with appropriate elements is assigned to the existence of synergistic effect between modifiers. The positive effects of nickel (Riaz et al. 2013) and silver (Behnajady and Eskandarloo 2013) containing species for copper modified Aeroxide®Degussa P25 titanium dioxide were observed.

Few papers are dedicated to the investigation of optical and structural properties of Cu/Zr (Ilkhechi et al. 2015b) and Cu/Zr/Si (Ilkhechi et al. 2015a) doped titania nanopowders as photocatalysts. Zr/Cu coupling for doping of TiO_2 nanopowders was carried out by sol-gel method (Ilkhechi et al. 2015b) and showed enhancement in photocatalytic degradation of methyl orange compared to undoped TiO_2. Considering above, the promising combination for visible light driven photocatalysis could be a combination of Cu and Zr for TiO_2 modification.

It has to be mentioned that the first experimental confirmation of perspective visible light photoreduction with bimetallic moiety Zr-O-Cu was published in 2005 (Lin and Frei 2005b). The study of high relevance by Lin and Frei (2005) showed that mesoporous silica systems with pore allocated Zr(IV)-O-Cu(I) assemblies can be successfully used in the process of CO_2 photochemical splitting induced by photoexcitation of the Zr(IV)/Cu(I) metal to metal charge transfer assemblies at 355 nm.

Summarizing, the idea of nonselective, total decomposition of organic pollutants in the aqueous media at the surface of TiO_2 catalyst with the help of solar light is desirable, but still somehow utopian aspiration, which requires further development. Combinations of Cu and Zr for TiO_2 modification can be a possible alternative to overcome disadvantages of TiO_2, and make it one step closer to become the ideal photocatalytic material for environmental remediation.

1.2.3 Dye and the visible light activity connected problems. Thermal lens spectrometry for photocatalytic activity evaluation

For the photo-oxidation reaction to occur the light is necessary. The use of high energy UV light is not only costly, but also can be hazardous. Therefore, the possible use of visible light (as a part of abundant solar light) is costless, safe and has recently drawn scientist's attention. However, some flaws are following this

approach.

It must be mentioned that it is obvious, that quantum yield of materials absorbing visible light is much lower compared to those under UV and photocatalytic response of that materials is not always as high as required. The photocatalytic test of the Vis light active material with model pollutant under the visible light is necessary in order to evaluate velocity and degree of pollutant degradation.

Additionally, more research is required to determine if visible light active materials can deliver an increase in the efficiency of photocatalysis under the solar irradiation or to prove that the visible light response does not play an important role in the gross photocatalytic activity. The visible light active N, S co-doped and N-doped commercial anatase TiO_2 powders did not show an enhancement for the degradation of phenol neither photocatalytic inactivation of *E. coli* under simulated solar light, as compared to P25. Even though they reveal good visible light response (Dahl et al. 2014).

Another concern about visible light photocatalytic activity assessment is an application of dyes for these purposes. Dyes are very usable for photocatalytic efficiency evaluation because of fast and easy handling. A strong recommendation not to use dye tests for activity assessment of visible light photocatalysts was expressed (Wu et al. 1998a), (Bae et al. 2014), (Rochkind et al. 2015). This recommendation is relevant due to sensitization mechanism of dye degradation, which manifests itself rather than the photocatalytic one under the visible light.

However, it is very important to critically analyze each case separately. There is a very interesting and informative review (Rochkind et al. 2015) providing important message to audience regarding this problem. The relevant objectives of using dyes for photocatalytic test and suspected mechanisms of material activation need to be as clear as possible.

Application of dyes for visible light photocatalytic activity evaluation is not appropriate because of probable overestimation of the results obtained by means of bleaching of the dye (Kuo and Ho 2001). However, overall degradation of dye as a pollutant can even not progress after decoloration under the visible light (Liu et al. 2000). It is suspected that dye degradation reaction occurred under the visible light due to the photosensitization mechanism is discontinued after the dye molecule lost

its ability to absorb visible light (Nasr et al. 1996).

The results of experiments under the simulated solar light suggested that both photocatalytic and photosensitizing mechanisms occurred during the irradiation and both TiO_2 and the light source are prerequisites for both reactions to occur. In the photocatalytic oxidation, TiO_2 has to be irradiated and excited by UV light energy (Fig. 6 A). In case of photosensitization (Fig. 6 B), dyes rather than TiO_2 are excited by visible light followed by electron injection onto TiO_2 conduction band. It is known that the photosensitizing mechanism is helping to improve the overall efficiency of dye degradation under the solar light (Konstantinou and Albanis 2004), (Kuo and Ho 2001).

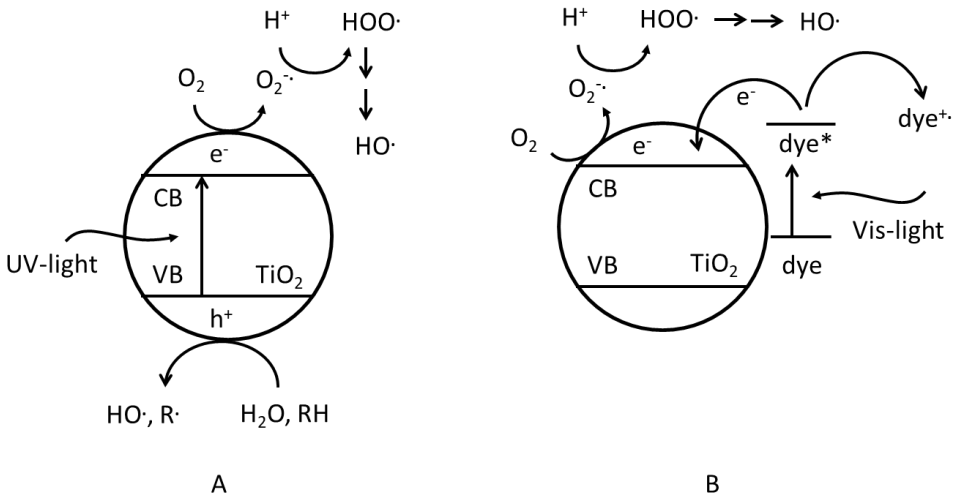

Fig. 6. Comparison of the photocatalytic mechanism (A) for UV irradiation of TiO_2 with the self-photosensitized pathway (B) of dye degradation under visible light (Wu et al. 1998b)

The photocatalytic degradation of RB19 dye under UV-light was studied carefully and the pathway of photocatalytic dye degradation was established (Bilal et al. 2018). It was shown that the C-N bond cleavage (Fig. 7 A) appears to be the first step for photocatalytic degradation of RB19 under the UV-light. In contrast to this, it was demonstrated another degradation pathway for RB19 under the simulated solar light (Abu Bakar et al. 2015). As a first step for the dye degradation under the simulated solar light the visible light chromophore (vinyl sulfonic group) cleavage is proposed (Fig. 7 B). It was shown earlier (Liu et al. 2000), that in the photosensitization mechanism the cleavage is preferentially located on the atom having the largest electron density in the ground state. It was demonstrated that the

mineralization process is in good correlation with the decolorization of dye. It was also established that dyes containing sulfur atoms (like RB19) are mineralized into sulfate ions (Hu et al. 2003), (Augugliaro et al. 2002). The kinetics of sulfate formation was found to be almost the same as that of dye decolorization.

Two different mechanisms are elucidated from the different processes occurred under the UV and simulated solar light. Under the UV light there is certainly the photocatalytic pathway, but under the solar light both photocatalytic and photosensitization mechanisms are possible. It is difficult to conclude whether the photocatalytic oxidation is superior to the photosensitizing oxidation mechanism or opposite. Moreover, it is a grate challange for scientists to distinguish between these mechanisms.

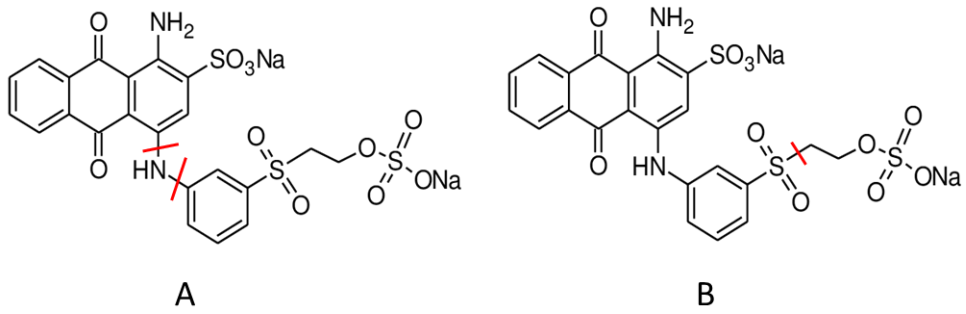

Fig. 7. Photocatalyst assisted RB19 degradation pathway based on mass spectrometry: A) under the UV light; B) under the simulated solar light. The preferential bond cleavage at initial stage of RB19 dye degradation is marked.

If we postulate that the probabilities of photocatalytic and photosensitization mechanisms are equal under the simulated solar light, then the feasibilities of photocatalytic and photosensitization mechanisms are equal. As a result, competition between two mechanisms occurs and the overall process efficiency consists of contribution of both mechanisms possibly taking place in parallel.

On the other hand, if there is a limiting factor influencing the probability of one of the mechanisms, the other mechanism is expected to become the governing one. The specification of the mechanism responsible for the dye degradation at different concentrations may help to determine the limiting factors and to deeper understand the photocatalytic processes.

As it is discussed in details on the p. 7-9 and shown in the photocatalytic mechanism scheme, it is commonly accepted that the photocatalytic mechanism is

based on two parallel processes (there are more than only two proceses, but in order to simplify the complicated scheme, we limit ourselves on two processes, which are globally different): 1) direct surface trapped hole or surface-bounded $HO^{\cdot}$ radicals oxidation, which may happen only after substrate (model pollutant) is adsorbed on the surface of TiO_2; and 2) free $HO^{\cdot}$ radical oxidation, which can occur without substrate adsorption (the contribution of this process to overall degradation is under the great concern, but can not be ignored) (Boonstra and Mutsaers 1975a), (Salvador 2011).

On the other hand, the photosensitization mechanism (shown in Fig. 6 (B)) is based on the electron transfer from dye molecule to TiO_2 particle. It was shown, that adsorption of the substrate (dye molecule in our case) on the TiO_2 is a necessary prerequisite for electron transfer (photosensitization mechanism) to occur (He et al. 2002).

These facts are leading to the following reflections: i) the efficiency of direct hole oxidation (surface-bounded $HO^{\cdot}$ radicals) and the efficiency of electron transfer processes in the photosensitization mechanism are dependent on efficient substrate adsorption on TiO_2 particles; ii) free $HO^{\cdot}$ radical oxidation process is independent of adsorption of substrate on TiO_2 particles (in water media with high concentration of water it may occur at close proximity to the TiO_2 particle, but does not require commencement of dye adsorption). Contribution of free $HO^{\cdot}$ radical oxidation process can be an advantage for photocatalytic mechanism making it superior.

In order that adsorption proceeds, a mass transport (diffusion) of the substrate from the bulk of solution towards TiO_2 particles surface is necessary. According to the Fick′s law flux is dependent of substrate concentration (Cussler 1997). Adsorption is also dependent on concentration. Moreover, the optimum loading of photocatalyst (TiO_2) found to be dependent on the initial substrate concentration (Herrmann 1999). Thus, the concentration of both dye and photocatalyst are influencing the degradation process. It is necessary to determine the mechanism responsible for the dye degradation at low dye and photocatalyst concentrations.

In order to follow the reaction of dye degradation at low dye and photocatalyst concentrations highly sensitive and accurate method is required. The accuracy requirement is satisfied by technique based on photothermal effect such as thermal lens spectroscopy (TLS). The general principle of operation of all

photothermal methods relies on the generation of heat by periodical excitation of the sample. Because of the nonradiative relaxation of the energy absorbed by the sample, a temperature gradient is produced, resulting in changes of physical parameters (*e.g.* density, refractive index) of the sample and its surroundings. These changes can be probed in a couple of ways depending on the chosen measurement technique. In case of TLS technique, the thermal lens arising from a refractive index gradient due to changes in temperature causes the defocusing of the laser beam (probe beam) passing through a transparent sample (Snook and Lowe 1995), (Marcano et al. 2006), (Franko 2001).

The intensity of probe laser beam is changed on its axis periodically depending on the absorption of the sample and is detected as the relative transmission of it through an aperture, which is located just in front of a photodetector. TLS method enables to perform sensitive measurement on samples for which the conventional spectrophotometric measurements cannot be used because of high errors at low absorbances. To the best of our knowledge, TLS method has been applied only in cases of photodegradation studies of soybean oils (Savi et al. 2015), hemoprotein–lipid complex (Tishchenko et al. 2017) and vitamin E acetate (Tiburcio-Moreno et al. 2012). However, no previous studies have used TLS method to study the photodegradation process of industrial textile dyes at very low concentrations.

1.3. HYPOTHESIS, GOALS AND OBJECTIVES

This research aims at obtaining novel photocatalytic materials and understanding the performance of as-synthesized Zr and Cu modified TiO_2 photocatalysts. The main objective of the research work is to evaluate the influence of simultaneous copper and zirconium oxides loading on the photocatalytic activity of mixed phase TiO_2. Determination of contribution of each oxide separately to the photocatalytic activity of TiO_2 is among important goals. A competition between photocatalytic and photosensitization mechanisms of RB19 dye degradation under the simulated solar light is the other point of interest of this work.

Three main hypotheses are claimed to be checked:

Hypothesis 1. ***Simultaneous utilization of Cu and Zr oxides on the surface of TiO_2 is beneficial for photocatalytic degradation of wastewater pollutants.***

At the first part of the research work, the hypothesis 1 is tested. The hypothesis 1 is based on previous research works showing enhancement of photocatalytic properties of TiO_2 modified with Cu and Zr (Ilkhechi et al. 2015a), (Ilkhechi et al. 2015b). A synergy effect between Cu and Zr ions loaded simultaneously is assumed to be present. The results of photocatalytic tests with methylene blue dye and terephthalic acid were taken as a main criterion for hypothesis evaluation. The basic characterizations of as synthesized photocatalytic powders and the results of photocatalytic tests are discussed in the Chapter 3.1.

Hypothesis 2. ***Cu and Zr oxides form Cu-O-Zr moieties on the surface of TiO_2 that beneficially contribute to the photocatalytic activity of TiO_2.***

The second part of the research work is about evaluation of the hypothesis 2. The hypothesis 2 is based on the study (Lin and Frei 2005b) where bimetallic moieties Zr-O-Cu were shown as perspective assemblies facilitating visible light photoactivity. Deep material structure characterization with XRD, EXAFS, XANES, EPR analysis, visualization with TEM and determination of material surface properties were chosen as a criterion for hypothesis testing. The results are presented in the Chapter 3.2.

Hypothesis 3. ***RB19 dye at low concentration degrades essentially by means of photocatalytic reaction.***

The third part of the research work is dedicated to evaluate the hypothesis 3. The 3rd hypothesis stands on the following statement: a competition between

photocatalytic and photosensitization mechanisms of dye degradation occurs under the simulated solar light. Attempt to distinguish between photocatalytic and photosensitization mechanisms was made. Determination of the governing mechanism at low dye concentration is in the focus of this work. The TLS method is chosen for hypothesis evaluation. The results are presented in the Chapter 3.3.

The objectives of the research work are summarized as follows:

1) to evaluate the effect of simultaneous presence of Cu/Zr on the properties of TiO_2;
2) to identify formation of Zr-O-Ti, Cu-O-Ti and Zr-O-Cu linkages on the TiO_2 particles;
3) to determine the role of Zr-O-Ti, Cu-O-Ti and Zr-O-Cu moieties in photocatalytic performance of TiO_2;
4) to reveal the reason of beneficial Cu/Zr loading;
5) to explore the capability of TLS method at low RB19 concentration;
6) to verify the governing mechanism responsible for RB19 degradation at low concentration.

The results obtained in the first, second and third year of my PhD studies are presented in the following chapters. They were presented also at the conferences: 9th European meeting on Solar Chemistry and Photocatalysis: Environmental Applications (SPEA9) in Strasbourg, June 2016; 1st AARC PhD Students Conference on Environmental and Sustainable Energy in Maribor, November 2016; 21st International Conference on Solid State Ionics in Padua, June 2017; New Photocatalytic Materials for Environment, Energy and Sustainability in Ljubljana, July 2017; 10th European meeting on Solar Chemistry and Photocatalysis: Environmental Applications (SPEA10) in Almería, June 2018; New Photocatalytic Materials for Environment, Energy and Sustainability in Porto, July 2018.

The article with the title “Cu and Zr surface sites in the photocatalytic activity of TiO_2 nanoparticles” (authors: O. Pliekhova, I. Arčon, O.Pliekhov, N. Novak Tušar, U. Lavrenčič Štangar) has been published in the journal Environmental Science and Pollution Research. The materials from this article are presented in the chapter 3.1.

The article with the title “Cu and Zr surface sites in photocatalytic activity of TiO_2 nanoparticles: the effect of Zr distribution” (authors: O. Pliekhova, O. Pliekhov, M. Fanetti, I. Arčon, N. Novak Tušar, U. LavrenčičŠtangar) has been published in the journal Catalysis Today. The materials from this article are presented in the chapter 3.2.

The article with the title “Determination of photocatalytic properties of copper and zirconium modified TiO_2 photocatalyst by photothermal techniques” (authors O. Pliekhova, Z. Ebrahimpour, M. Abdelhamid, K. Gadejisso-Tossou, H. Cabrera, D. Korte, J. Niemela, U. Lavrenčič Štangar, M. Franko) is under preparation for publication. The materials from this article are presented in the chapter 3.3.

2 EXPERIMENTAL

2.1. PREPARATION OF PHOTOCATALYSTS

The surface modified photocatalysts were prepared by modification of commercial Aeroxide® Degussa P25 (P25). Organic and inorganic metal precursors (MP) were adopted for surface modification. Deionized water prepared by a NANO pure system (Barnstead) was used for all solutions preparation.

Organic MP were applied in combination of sol-gel and impregnation methods. Ethanol absolute (C_2H_5OH) 99,9 % from Sigma-Aldrich, acetylacetone ($C_5H_8O_2$), 99 % from Merck, copper(ll) acetyl-acetonate ($C_{10}H_{14}CuO_4$), 99 % from Merck, zirconium(lV) butoxide, 80 % in 1-butanol $Zr(OC_4H_9)_4$, from Sigma-Aldrich were used. Sample solutions were prepared under ambient conditions with continuous stirring. Titanium dioxide with 0.05; 0.1; 0.5; 1; 5 mol % of copper, 1 mol % of zirconium and double metal modified samples with 0.05 and 0.1mol % of copper and 1mol% of zirconium were obtained. Initially, calculated amount of MP: copper(ll) acetyl-acetonate (0.008; 0.016; 0.08; 0.16 or 0.8 g) for copper modification and zirconium(lV) butoxide (286 µL) for zirconium modification were dissolved in 20 mL of absolute ethanol. Acetylacetone (chelating agent) was added gradually in a molar ratio of MP/$C_5H_8O_2$ =1/3. Water was added dropwise in 10-time excess to MP. Catalysts with simultaneous loading of Cu and Zr were prepared by loading required amount of both MP at the same time. After 1h of stirring, 5 g of P25 was dispersed in obtained Cu or/and Zr solution in ethanol and the slurry was stirred for another 1h. After slurries preparation, they were dried at 80 °C and calcined at 500 °C for 2h followed by the grinding process in an agate mortar.

Samples with inorganic origin of MP were produced by wet impregnation method. Aqueous solutions prepared from $Cu(NO_3)_2 \cdot 2.5H_2O$, 98 % (Alfa Aesar) and $ZrO(NO_3)_2 \cdot xH_2O$ (Fluka) were used. Before the solution preparation crystalohydrates were calcined till the constant mass. Modified catalysts with 0.1 and 0.5 mol % of copper and 1.0 mol % of zirconium relatively to the Ti content were prepared. Corresponding amounts of metal nitrates were dissolved in 20 mL of water together with 1 g of P25. The slurry was sonicated in ultrasound bath at 90 °C for 1 h. Afterwards, the samples were dried at 150 °C and calcined at 500 °C for 30 min. Obtained photocatalysts were grinded in agate mortar.

The samples were denoted as P25/Cu_x, P25/Zr or P25/Zr/Cu_x, where x indicated the molar percent of impregnated Cu ions, expressed as nominal(theoretical) amount; the nominal amount of Zr in all Zr containing samples was always 1 mol %.

2.2. PHOTOCATALYTIC TESTS

Photocatalytic experiments were performed by degrading the methylene blue (MB) in water (initial concentration 10 ppm), Reactive blue 19C.I. (RB19) in water (initial concentration 50 ppm) and terephthalic acid (TPA) in $2 \cdot 10^{-3}$ M sodium hydroxide solution (initial concentration 65 ppm). Suspensions consisted of 0.1 g, 0.1 g and 0.02 g of photocatalyst for MB, RB19 and TPA degradation, respectively, in 100 mL of model pollutant solution. Before experiment each suspension was sonicated for 10 min. In order to achieve adsorption-desorption equilibrium before irradiation, each suspension was sustained for 1 h by stirring in the dark. After equilibration, suspensions were irradiated in a solar simulator chamber (Suntest XLS+, Atlas, USA) with Xenon lamp, using daylight filter. Irradiation intensity was 75.0 mW/cm^2 (300–800 nm) with UV fraction of 6.1 mW/cm^2 (300–400 nm). The experiments under UV light irradiation were carried out in the home made photocatalytic chamber with UV light (λ_{max} = 365 nm, 2.3 mW/cm^2).

The beginning of the sample irradiation was treated as the onset of photocatalytic reaction. Every time point after irradiation the sample of suspension was taken and centrifuged at 1300 rpm for 3 min. Methods for determination of model pollutants degradation are given below.

To follow the degradation of TPA (equation (9)), the formation of fluorescent intermediate product of decomposition – 2-hydroxyterephthalic acid (HTPA) was monitored:

$$[TPA] \xrightarrow{k_1} [HTPA] \xrightarrow{k_2} other\ products \qquad (10)$$

where k_1 and k_2 are the rate constants of formation and degradation of HTPA, respectively.

The concentration of HTPA was evaluated by Infinity F200, Microplate reader, TECAN, Switzerland as an emission peak at wavelength 420 nm (excitation wavelength – 314 nm). The data of HTPA formation with irradiation time was fitted by solving simplified kinetic equation (Černigoj et al. 2010):

$$[HTPA] = \frac{k_1}{k_2}(1 - e^{-k_2 t}) \quad (11)$$

where k_1 and k_2 are the rate constants of formation and degradation of HTPA, respectively.

Concentration of MB was determined by Perkin Elmer UV/Vis spectrophotometer at the 664 nm wavelength. Rate constants (k) were calculated from the following equation:

$$ln(C_t / C_0) = -kt \quad (12)$$

where C_0 and C_t represent the MB concentrations at the photodegradation start and at time t, respectively.

The percent of MB decolorization was estimated using the following relation:

$$MB\ decolorization\ (\%) = [(C_0 - C)/C_0] \times 100 \quad (13)$$

Concentration of RB19 was determined by Perkin Elmer UV/Vis spectrophotometer at the 594 nm wavelength.

The percent of RB19 decolorization was estimated by using relation similar to *(13)*. Accuracy of photoactivity measurements was± 3 %.

Total organic carbon (TOC) was determined by Analytik Jena AG MULTI N/C 3100 analyzer. All the samples were centrifuged before analysis in order to separate TiO_2nanoparticles from the solution. Prior to the TOC analysis purging with oxygen during 150 s was applied for the solution and the sampleswere manually acidified by 25 % H_2SO_4 (3 drops). The analyzer was set for: the sample volume 100 μL; the washing volume 2 mL; the furnace temperature 850 °C; the integration time 300s.Percentage of mineralization was calculated from the determined concentration of organic carbon (COC) in mg/L. COC calculated after incineration of dye/catalyst solution before irradiation step was considered to represent 100 % of organic compounds in the solution. COC after irradiation of dye/photocatalyst suspensions during given time corresponds to organic compounds which have not been mineralized yet.

2.3. CHARACTERIZATION OF Cu/Zr-TiO_2CATALYST

2.3.1 X-ray diffractometry (XRD)

Diffraction of light can be observed when a wavelength is of the same order of magnitude as a distance between scattering objects. The interatomic distances

between neighboring atoms in crystals are about 0.5-2.5 Å. The electromagnetic radiation in this range is X-ray radiation. If the phase shift between the two elastically scattered X-rays is multiple of 2π the interference appears and a peak in the diffraction pattern is observed. A detailed characterization of peaks position and intensity gives information about phase quantities, unit cell parameters and crystallite sizes. All the crystallographic parameters can be refined with the best fit of observed and calculated diffraction patterns.

The crystal structures of the TiO_2 samples were identified by X-ray diffraction instrument (PAN-alytical Xpert proMPD, Almelo, Netherlands) using Cu Kα irradiation (1.5406 Å) over the range 10 to 80° 2θ at a scan rate of 2°/min.

Diffraction patterns were compared with reference ICSD database. The diffraction lines of anatase and rutile were detected and taken into account for data refinement. The phase composition analysis was performed and unit cell parameters were calculated by Rietveld refinement method based on the reference diffractograms from ICSD database (High Score Plus software). Estimation of the amount of the certain phase was performed by Profile fitting analysis. The quality of Rietveld refinement was evaluated in terms of goodness of fit indicator.

The crystallite size was determined by the broadening of the (011) anatase and (110) rutile peaks reflections by the Scherrer formula:

$$t = 0.9\lambda/(\beta \cos \theta) \qquad (14)$$

where t is the particle size in nm, λ is the wavelength of X-rays in Å (1.5418 Å), β is the full width of the diffraction peak on its half maximum (FWHM) in radians and θ is the Bragg angle in radians (Jenkins; Snuder 1996).

The errors for calculated crystallite sizes were determined as 0.001 nm for anatase and 0.002 nm for rutile. However, Scherrer formula yields an average value of the crystallite size, which however is affected by several approximations, which limit its application and reliability for heterogeneous catalysts (Hargreaves 2016). Therefore, the use of a digit after the comma in the values is not recommended.

2.3.2 Scanning electron microscopy (SEM) and energy dispersive X-ray (EDX)

A scanning electron microscope (SEM) scans a focused electron beam over a surface to create an image. The electrons in the beam interact with the sample, producing various signals that can be used to obtain information about the surface

topography and composition. As the electrons interact with the sample, they produce secondary electrons, backscattered electrons, and characteristic X-rays. These signals are collected by one or more detectors to form images, which are then displayed on the computer screen. When the electron beam hits the surface of the sample, it penetrates the sample to a depth of a few microns, depending on the accelerating voltage and the density of the sample. Many signals, like secondary electrons and X-rays, are produced as a result of this interaction inside the sample.

EDX is a qualitative and quantitative technique associated to electron microscopy. The elemental composition of the selected area of the sample can be determined by measuring the energy of emitted photons by Energy Dispersive Analyser (Goldstein et al. 2003).

A JSM – 7100f, JEOL scanning electron microscope (SEM) was used for morphological analysis.

The actual zirconium and copper loading was determined by energy dispersive X-ray (EDX) standardless analysis routed by means of field emission scanning electron microscope (JSM – 7100f, JEOL) equipped with an EDX detector (X-Max80, OXFORD). For making measurements the powders were pressed into pellets.

2.3.3 Transmission electron microscopy (TEM)

The TEM operates on the same basic principles as the light microscope but uses electrons instead of light. Because the wavelength of electrons is much smaller than that of light, the optimal resolution attainable for TEM images is many orders of magnitude better than that from a light microscope. Thus, TEM images can reveal the finest details of internal structure - in some cases as small as individual atoms.

The beam of electrons from the electron gun is focused into a small, thin, coherent beam by the use of the condenser lens. This beam is restricted by the condenser aperture, which excludes high angle electrons. The beam then strikes the specimen and parts of it are transmitted depending upon the thickness and electron transparency of the specimen. This transmitted portion is focused by the objective lens into an image. Optional objective apertures can be used to enhance the contrast by blocking out high-angle diffracted electrons. The image strikes the phosphor screen and light is generated, allowing the user to see the image. The darker areas of

the image represent those areas of the sample where fewer electrons were transmitted through while the lighter areas of the image represent those areas of the sample where more electrons were transmitted through (Williams and Carter 2009).

The powders were dispersed in water and a drop of diluted suspension was placed on a carbon-coated grid and evaporated at ambient temperature. Scanning transmission electron micrographs were acquired on a JEOL JEM 2100 microscope operated at 200 kV.

2.3.4 Nitrogen sorption measurements (BET SSA)

The specific surface area of a powder is determined by physical adsorption of a gas on the surface of the solid and by calculating the amount of adsorbate gas corresponding to a monomolecular layer on the surface. Physical adsorption results from relatively weak forces (van der Waals forces) between the adsorbate gas molecules and the adsorbent surface area of the test powder. The determination is usually carried out at the temperature of liquid nitrogen. The amount of gas adsorbed can be measured by a volumetric or continuous flow procedure. Gas adsorption also enables the determination of size and volume distribution of micropores (0.35 – 2.0 nm).

The outgassing conditions defined by the temperature, pressure and time should be chosen so that the original surface of the solid is reproduced as closely as possible. Outgassing of many substances is often achieved by applying a vacuum, by purging the sample in a flowing stream of a non-reactive, dry gas, or by applying a desorption-adsorption cycling method. In either case, elevated temperatures are sometimes applied to increase the rate at which the contaminants leave the surface. Caution should be exercised when outgassing powder samples using elevated temperatures to avoid affecting the nature of the surface and the integrity of the sample.

The specific surface areas (SSA) of the samples were evaluated by obtaining the adsorption isotherms by a Micromeritics Tristar 3000 instrument.Nitrogen was used as adsorbate gas. The amount of adsorbed gas is correlated to the total surface area of the particles including pores in the surface.

The samples were dried in a vacuum applying elevated temperatures. Unless otherwise instructed P/P0 of 0.1, 0.2 and 0.3 as standard measurement points were

used. The volume of gas adsorbed to the surface of the particles was measured at the boiling point of nitrogen (-196 °C). The calculation was based on the BET theory(Sing 1985).

2.3.5 Diffuse reflectance UV/VIS spectroscopy (DRS)

The widely used method for estimation of the electron transition nature and the energy band gap of the semiconductors is the UV/VIS diffuse reflectance spectroscopy. Normally, the diffuse reflectance spectrum is converted to the absorption spectrum by use of the Kubelka Munk equation:

$$\frac{K}{S} = \frac{(1-R_\infty)^2}{2R_\infty} = F(R_\infty) \qquad (15)$$

where K and S are Kubelka Munk scattering and absorption coefficients, respectively; R is reflectance and $F(R_\infty)$ is remission (Kubelka Munk) function.

The band gap can be determined by plotting $[F(R_\infty)h\nu]^2$or $[F(R_\infty)h\nu]^{\frac{1}{2}}$ versus photon energy (hν). The intersection between the linear fit and the photon energy axis gives the value of band gap energy (López and Gómez 2012).

The diffuse reflectance UV/Vis absorption spectra of powdered samples were measured using a UV/Vis spectrophotometer equipped with an integrating sphere (LAMBDA 950 UV/Vis with 150 mm integrating sphere, Perkin Elmer, USA). Direct and indirect band gaps were determined by plotting the Kubelka–Munk transformation of the original diffuse reflectance spectra vs. photon energy.

2.3.6 Dynamic light scattering (DLS)

The DLS technique is based on the Rayleigh scattering. Because of Brownian motion, which is the random movement of particles that collide to each other, the scattering of the incoming light occurs at the particles in liquid media. This scattering is oriented in all directions from the particle and caused by the light with bigger wavelength than the particle size. Brownian motion is affected by the particle size, viscosity of the liquid media and temperature. Since the viscosity and temperature are known, the particle size can be determined.

The sizes of agglomerates of nanoparticles were measured by dynamic light scattering (DLS) technique (Malvern, 2011), using particle size analyzer Brookhaven 90Plus/BI-MAS. The suspension with concentration 50 mg/L in ddH_2O was prepared

(Taurozzi et al. 2012), sonicated for 10 min in an ultrasonic bath and left for 1 h to stabilize. Optimum concentration was estimated by dilution of prepared solution. The cuvette was filled with as prepared solution and measured. Then the solution was diluted with water until the best result, with respect to polydispersity parameter, counting rate and autocorrelation function. After that, suspension was measured 3 times in given time interval (0 min, 30 min, 60 min).

2.3.7 $HO^{\cdot}$ radical capturing test

Fenton's reagent, which is a mixture of hydrogen peroxide and iron(II) sulfate, was used as a source of the hydroxyl radicals. All experiments were performed in a batch mode at room temperature and under continuous stirring. The 250 mL Erlenmeyer flask equipped with a magnetic stirrer and covered with aluminum foil to avoid contact with light was used as a reactor. In each experiment, the reactor was loaded with a reaction mixture that contained powdered TiO_2 samples (400.00 mg) and volume of 50.0 mL of the following reagents at the final concentrations stated in brackets: RB19 (50.00 mg/L), $Fe_2SO_4 \cdot 7H_2O$ (1.000 mg/L). The pH of the reaction medium was adjusted to 3 using 1.00 M H_2SO_4 to enhance H_2O_2 stability and to prevent the precipitation of iron at higher pH. The reaction was initiated by the addition of H_2O_2 (concentration in the final solution 10.00 mg/L). After initialization, the reaction mixture was left in the dark for 60 min. After that the mixture was centrifuged and filtered. The reaction between produced $HO^{\cdot}$ radicals and TiO_2 catalyst was tracked by decolorization of RB19 dye. The absorbance of RB19 at λ=595 nm was used as a measure of the degradation process by using a Hewlett Packard HP 8453 UV/Vis spectrometer. The conversion of RB19 was used to quantify the decomposition efficiency (De) according to:

$$De = (A_0 - A)/A_0 \qquad (16)$$

where A_0 is the absorbance of the RB19 solution before the addition of H_2O_2 and A is the absorbance of the BR19 solution after the reaction.

2.3.8 Amine titration for determination of surface acidity of Cu/Zr-TiO_2 catalysts

In the amine titration method with indicators, the color of suitable indicators adsorbed on the surface is giving a measure of its acid strength. The surface acidity of the catalysts was determined by titration with n-butylamine following the procedure described by (Papp et al. 1994). Four Hammett indicators with different pK_a were used: bromothymol blue (pK_a = +7.2), neutral red (pK_a = +6.8), methyl red (pK_a = +4.8), methyl yellow (pK_a = +3.3). Photocatalytic powder (0.1 g) was dispersed in 10 mL of benzene. Three drops of 0.01N indicator solution in benzene were added to the flask. Stirring with teflon bar was applied during the experiment.

N-butylamine (0.01N in benzene) was used for titration the catalyst suspension. The amount of N-butylamine required to affect the colour change on the surface of the powder was recorded. If the colour is that of the acid form of the indicator, then the value of the H_0 function of the solid is equal to or lower than the pK_a of the conjugated acid of the indicator.

The amount of acid on a solid (A) is expressed as the number of mmol of acid sites per unit weight:

$$A = C \cdot V/m \qquad (17)$$

where C is a concentration of N-butylamine (0.01 N), V is volume of N-butylamine used for titration, m is a mass of photocatalytic powder.

The number of acidic sites belonging to the particular crystal phase is calculated for each photocatalyst:

$$A(X)_{MR} = A^R_{pK1} \qquad (18)$$

$$A(X)_{BB} = A^R_{pK1} + A^A_{pK1} \qquad (19)$$

$$A(X)_{NR} = A^R_{pK1} + A^A_{pK1} + A^R_{pK2} \qquad (20)$$

where A_{MR}, A_{BB}, A_{NR} are the number of mmol of acid sites per unit weight determined by methyl red (MR), bromothymol blue (BB) and neutral red (NR), respectively; (X) is the name of the sample; the superscripts R and A are related to the rutile and anatase, respectively.

The number of acidic sites covered by modifier is expressed as:

$$AC(X)^y_z = A(P25)^y_z - A(X)^y_z \qquad (21)$$

where $AC$is the number of mmol of acid sites per unit weight covered by modifier; (X) is the name of the sample; the superscript y is R or A related to the rutile or anatase, respectively; the subscript z is pK_1 or pK_2.

The fraction of surface sites covered with modifier is expressed as:

$$F(X)_z^y = \frac{AC(X)_z^y}{A(P25)_z^y} \times 100\% \qquad (22)$$

where F is the fraction of surface sites covered with modifier, %; $AC$is the number of mmol of acid sites per unit weight covered by modifier; (X) is the name of the sample; the superscript y is R or A related to the rutile or anatase, respectively; the subscript z is pK_1 or pK_2.

2.3.9 Complexometric titration with EDTA

Precise amount of 0.5 g of the sample powder was mixed with 20 mL of conc. H_2SO_4 (d=1.84 g/cm^3) and 8.00 g of $(NH_4)_2SO_4$ in a 250 mL glass beaker. Mixture was heated at 200 ºC until dissolved. Cooled solution was diluted with water, and basified to pH 10 with 20 % NaOH in order to ensure the separation of soluble copper-ammonia complexes from precipitated titania. Precipitate was removed by filtration and washed with water. The filtrate was acidified to pH 5 with 20 % HCl and titrated with 0.005 M solution of EDTA using xylenol orange as an indicator.

2.3.10 Isoelectric point (IEP)

Surfaces of solid particles immersed to the liquid naturally charge to form a double layer. In the common case when the surface charge-determining ions are H^+/OH^-, the net surface charge is affected by the pH of the liquid in which the solid is submerged. In the absence of chemisorbed or physisorbed species particle surfaces in aqueous suspension are generally assumed to be covered with surface hydroxyl species.

The isoelectric point (IEP), is the pH at which a particle is electrically neutral. The net charge on the particle is affected by pH of its surrounding environment and can become more positively or negatively charged due to the gain or loss of protons (H^+). At pH values above the IEP, the predominant surface species is Me-O^-, while

at pH values below the IEP, Me-OH_2^+ species predominate (Chevalier and Bolzinger 2013).

Isoelectric points were determined using Zetasizer nano ZS instrument (Malvern) with electrophoretic light scattering technology in the pH range of 2–12 adjusted by the addition of either 0.1 M NaOH or 0.1 M HCl. The pH value of each suspension was measured using a digital pH meter (Mettler Toledo). The powder samples were preconditioned in cold ultrasonic bath for 1h to attain homogeneous suspension.

2.3.11 X-ray absorption spectroscopy (EXAFS and XANES)

EXAFS and XANES spectra of Cu and/or Zr modified TiO_2 samples with varied metal concentrations and reference Cu and Zr compounds were measured at P65 beamline of PETRA III (DESY) and XAFS beamline of ELETTRA synchrotron radiation facilities in fluorescence or transmission detection mode. A Si (111) double crystal monochromator was used at both beamlines, with energy resolution of about 1 eV at Cu K-edge and about 2 eV at Zr K-edge. At P65 beamline a flat mirror installed in front of the monochromator was used to effectively remove higher-order harmonics. The intensity of the monochromatic X-ray beam was measured by three consecutive ionization detectors. At P65 beamline 5 cm long ionisation chambers were used, filled with following gas mixtures for Cu K-edge: 1000 mbar N_2 (first), 1000 mbar Ar (second), 1000 mbar Kr (third). At XAFS beamline 30 cm long ionisation chambers were used, filled with following gas mixtures for Cu K-edge: (first) 1250 mbar N_2, and 750 mbar He; (second) 250 mbar Ar, 1000 mbar N_2 and 750 mbar He; (third) 1000 mbar N_2, 300 mbar He, and 700 mbar Ar; and for Zr K-edge: (first) 300 mbar Ar, 1000 mbar N_2 and 700 mbar He; (second) 2000 mbar Ar, (third) 400 mbar Kr, 1000 mbar N_2, and 600 mbar He.

The samples were prepared in the form of homogenous pellets, pressed from micronized powder mixed with boron nitride(BN). In all cases the total absorption thickness of the sample was about 2.5 above the Cu or Zr K-edge. Sample pellets were placed between the first and second ionization cell. For the samples with low Cu concentrations, fluorescence detection mode was used, with SDD fluorescence detector at XAFS beamline, and 7-pixel HPGe detector at P65 beamline, to measure the intensity of Cu K-alpha emission line. At both beamlines we used 100-micron

thick aluminium foil as a filter to reduce Ti K-alpha signal from the sample. Three to seven repetitions of the scans with integration time of 5 s/step, were superimposed to improve signal-to-noise ratio. Individual scans were measured on different spots of the same sample to avoid radiation damage.

The absorption spectra were measured in the energy region from -150 eV to +1100 eV relative to the Cu K-edge (8979.0 eV) or Zr K-edge (17998.0 eV). In the XANES region equidistant energy steps of 0.3 eV were used, while for the EXAFS region equidistant k steps of 0.03 $Å^{-1}$ were adopted. The exact energy calibration was established with simultaneous absorption measurement on a 7-micron thick Cu or Zr metal foil placed between the second and the third ionization chamber. Absolute energy reproducibility was ±0.03 eV.

The analysis of XANES and EXAFS spectra is performed with Demeter (IFEFFIT) program package (Ravel and Newville 2005) in combination with FEFF6 program code (Rehr et al. 1992) for ab initio calculation of photoelectron scattering paths.Structural parameters of the local Cu or Zr neighborhood (type and average number of neighbors, the radii and Debye-Waller factor of neighbor shells) were quantitatively resolved from the EXAFS spectra by comparing the measured EXAFS signal with model signal, constructed ab initio with the FEFF6 program code from the set of scattering paths of the photoelectron in a tentative spatial distribution of neighbor atoms.

The EXAFS models included three variable parameters for each shell of neighbors: the shell coordination number (N), the distance (R) and the Debye-Waller factor (σ^2). A common shift of energy origin ΔE_o was also varied for each shell. The amplitude reduction factor S_0^2 was fixed at the value of 0.85 for Cu EXAFS and 0.90 for Zr EXAFS.

The FEFF model for Cu K-edge EXAFS spectra comprised six oxygen atoms in nearest coordination shell, distributed at two distances characteristic for octahedrally coordinated Cu(II) cations tetragonally distorted due to Jahn–Teller effect. In the more distant coordination shells Ti, Cu, Zr and O atoms are included in the model at distances characteristic for the expected Cu(II) species that may be present in the samples (CuO nanoparticles or hetero-metallic Cu-O-Ti and Cu-O-Zr species). In a similar way, the FEFF model for Zr K-edge EXAFS spectra is constructed. It comprised oxygen atoms in nearest coordination shell, distributed at

two different distances, and Ti, Cu, Zr and O atoms in the more distant coordination shells to identify a presence of ZrO nanoparticles or hetero-metallic Zr-O-Ti or Zr-O-Cu bonding. The atomic species of neighbors are identified in the fit by their specific scattering factor and phase shift.

2.3.12 Electron paramagnetic resonance (EPR) spectroscopy

The low temperature EPR experiments were performed by EMX Plus EPR spectrometer (Bruker, Germany) operating in Q-band in the standard ER 5106 QT Q-band probe for cw-EPR and by EMX EPR spectrometer (Bruker) operating in X-band at 100 kHz field modulation in the standard TE_{102} (ER 4102 ST) rectangular cavity using thin-walled quartz EPR tubes (Bruker). The temperature was lowered to 100 K by the temperature control unit ER 4141VT-U (Q-band; Bruker) or ER 4111 VT (X-band; Bruker) with liquid nitrogen as the refrigerant. The EPR spectra of powder TiO_2 samples were recorded at room temperature (RT) and/or at 100 K, in dark or upon continuous *in situ* UV or visible light photoexcitation. The irradiation source of the UV light was a UV LED monochromatic radiator (λ_{max} = 365 nm; Bluepoint LED, Hönle UV Technology). The value of the irradiance (λ_{max} = 365 nm; 20 mW cm^{-2}) within the EPR cavity was determined using a UVX radiometer (UVP, USA). The LED light source KL 1600LED (T = 5600 K; Schott, Germany) was applied to provide the visible light irradiation, characterized with the illuminance of 160 klx measured by a digital lux meter (Metra Blansko, Czech Republic). The *g*-values were determined with an uncertainty of ± 0.0005 by the simultaneous measurement of a reference sample containing Mn(II)/MgO standard (Yordanov et al. 1999) or using a built-in magnetometer.

The EPR experiments with TiO_2 powders dispersed in water or dimethylsulfoxide were carried out by means of EMX Plus X-band EPR spectrometer with a High Sensitivity Probe-head (Bruker) in the small quartz flat cell (WG 808-Q, Wilmad-LabGlass, optical cell length 0.045 cm). The spin trapping agent (5,5-dimethyl-1-pyrroline *N*-oxide, DMPO) was added to the TiO_2 stock suspensions (1 g L^{-1}), which were further diluted to the final TiO_2 concentration of 0.33 g L^{-1}. The prepared suspensions were then carefully aerated by a gentle air stream. The samples were irradiated at 295 K directly in the EPR resonator using

LED sources of either UV (λ_{max} = 365 nm; 14 mW cm^{-2}) or visible (160 klx) radiation and the EPR spectra were recorded *in situ*.

All the EPR experiments were carried out at least in triplicate; with the standard deviation in the relative EPR intensity of ± 10 %. The concentration of photogenerated paramagnetic species was evaluated from the double-integrated EPR spectra based on the calibration curve obtained from the EPR spectra of 4-hydroxy-2,2,6,6-tetramethylpiperidine (Tempol) solutions measured under strictly identical experimental conditions. The experimental isotropic EPR spectra were analyzed and simulated using the Bruker software (WinEPR) and Winsim2002 software (Duling 1994).

2.3.13 Thermal lens spectrometry (TLS)

The degradation of RB19 by unmodified and Cu or/and Zr modified TiO_2 nanoparticles was investigated under simulated solar light irradiation with a 300W UV lamp (Osram Ultra Vitalux 300W E27) with radiated power of 13.6 W in near UV (315-400 nm) and 3.0 W at shorter wavelengths (280-315 nm), the remaining 284 W at Vis (400-800 nm) light. The lamp was placed in a vertical position at 5 cm distance from the cuvette. The sample containing 6 g/L of photocatalyst suspended in an initial concentration of 5 mg/L RB19 was placed in a 1cm·1cm·5cm quartz cuvette and illuminated by the lamp over 50 min. After each 5 minutes of irradiation, the suspension has been left for about 20 min to relax and remove any thermal energy induced by illumination. The TLS measurements were performed after each 5 min time interval of irradiation.

The experimental setup of TLS system for the dye degradation measurements used in this work is shown schematically in Fig. 9. The excitation laser beam (MGL-III-532-100, UltraLasers) at 532 nm wavelength and with 25 mW power was first collimated and after that focused into a small spot of 20 microns on the sample surface using a set of lenses L3, L4, L5 with 30 mm, 15 mm, 100 mm focal lengths (LB1757-A, LB1437-A,LB1676-A,Thorlabs), respectively. The excitation beam was modulated in intensity at 1 Hz frequency by a signal generator (RIGOL DG1022, RIGOL Technologies, Inc). The TL effect was probed by a 3 mW output power at 632.8 nm output wavelength He-Ne probe laser beam (05-UR-111, Melles Griot) which was previously collimated in a 6 mm spot using a set of 30 mm and 15 mm

focal length lenses (LB1757-A, LB1437-A, Thorlabs), respectively. Both beams were directed coaxially through the sample using a dichroic mirror DM (DMSP605, Thorlabs). Then, the resulted intensity change was detected by the Si amplified detector (PDA 36A-EC, Thorlabs) equipped with a pinhole of 0.5 mm diameter located in front of it. The TL signal was recorded directly using both a digital oscilloscope (RIGOL DS1102E, RIGOL Technologies, Inc) and a parallel Arduino (Mega 2560, Arduino).

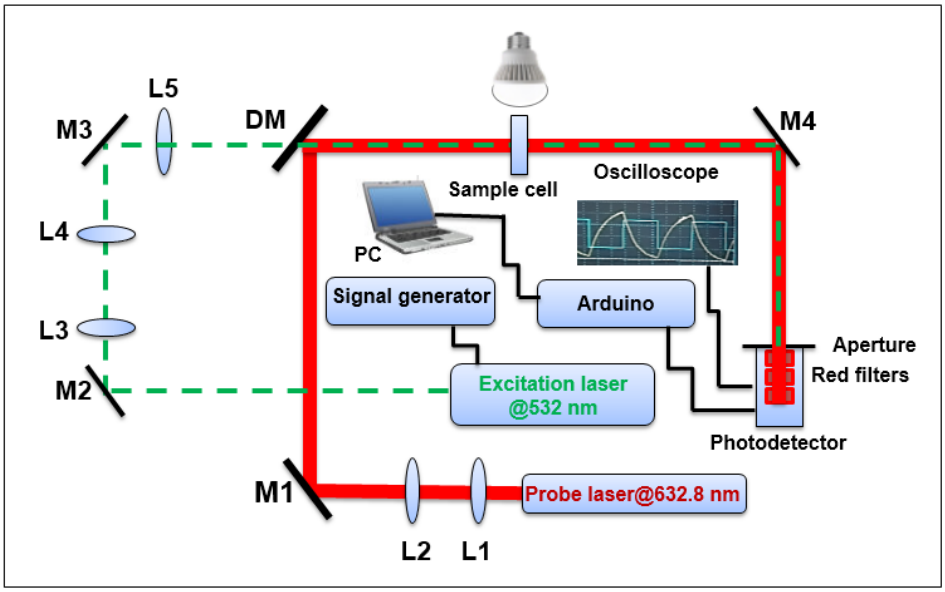

Fig. 8. Scheme of the TLS experimental setup. L1, L2, L3, L4, L5: lenses, M1, M2, M3, M4: reflecting mirrors, DM: dichroic mirror.

The absorbance spectra of the investigated samples were recorded on a dual beam UV-Vis spectrophotometer (PERKIN ELMER, model Lambda 650) in a 10 mm optical path quartz cuvette (HELLMA, model 100-QS). According to producer's specification the photometric accuracy of the instrument within the 440-635 nm range is ±0.005 a.u.

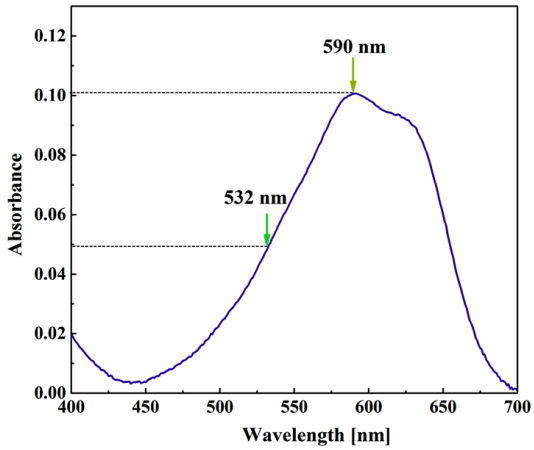

Fig. 9.Optical absorption spectrum of 10 ppm RB19 solution.

Fig. 9 shows the optical absorption spectrum of 10 ppm RB19 solution recorded with UV-Vis spectrophotometer. As it can be seen, the spectrum was broad and has a maximum absorption peak at 590 nm. However, the available excitation laser was emitting at 532 nm and the absorption bands of the photocatalysts (unmodified and Cu/Zr modified TiO_2) are in the blue region of the optical spectrum. Therefore, the selected pump beam wavelength was suitable also for sensing RB19 degradation although the absorption of the dye is half of the maximum value.

2.4. PHOTOCATALYTIC FILMS

2.4.1 Film preparation

Obtained powders were dispersed in titania-silica sol-suspension according to patented procedure and previous studies of commercial powder catalysts immobilization (Kete et al. 2014). Titanium tetraisopropoxide in ethanol solution was hydrolyzed by aqueous solution of perchloric acid. After hydrolysis and condensation reactions suspension was refluxed for 48h resulting in nanocrystalline TiO_2 sol. Separately, thetraethoxysilane (TEOS), deionized water and hydrochloric acid were mixed, producinghomogeneous silica sol. Further, nanocrystalline TiO_2 sol, silica sol, colloidal SiO_2 and ethanol were mixed together producing binder sol. Finally, corresponding Cu or Zr modified P25 powders were dispersed in the binder sol. The films were immobilized on microscope slides (76 mm·26 mm·1 mm) by the dip coating technique with 10 cm/min pulling speed. After the deposition the layer was dried using a hair dryer and treated at 150°C for 30 min.

2.4.2 Mechanical stability test

Mechanical stability of deposited layers was determined by Hardness Pencil test (also named Wolff-Wilborn test) with ELCOMETER 501.The Elcometer 501 tester uses graphite pencils with different hardness. It was designed to ensure that the pencil is maintained at a constant angle of 45° and exerts a force of 7.5 N. The pencil must be prepared with the special sharpener and abrasive paper before using. After preparation, the device was pushed over the flat-coated surface. The lowest hardness value of the pencil, which marks the coating, determines the coating's hardness rating.

3. RESULTS AND DISCUSSION

3.1. EVALUATION OF THE FIRST HYPOTHESIS.

Hypothesis 1. ***Simultaneous utilization of Cu and Zr oxides on the surface of TiO_2 is beneficial for photocatalytic degradation of wastewater pollutants.***

SIMULTANEOUS LOADING OF Cu AND Zr IONS FOR PHOTOCATALYTIC DEGRADATION OF WATER POLLUTANTS UNDER THE SIMULATED SOLAR LIGHT

The photocatalytic powders modified with Cu and Zr ions were obtained by wet impregnation method with Aeroxide® Degussa P25 (P25) as a source of TiO_2 and metal nitrates $Cu(NO_3)_2 \cdot 2.5H_2O$ and $ZrO(NO_3)_2 \cdot xH_2O$ as sources of metal ions. The crystal structures of Cu and Zr modified TiO_2 catalysts were determined by XRD. X-ray diffraction patterns of Cu and Zr modified TiO_2 along with reference P25 compound are presented in Fig. 10.

Table 1. Phase composition, particle size, specific surface area (SSA) and Zr/Cu loading of TiO_2 catalysts.

Sample	Phases	Phase content,%	Particle size (SEM), nm	SSA (S_{BET}), m^2/g	Zr/Cu loading (EDX), mol %
P25	Anatase	87.2	20-30	48.45±0.04	-/-
	Rutile	12.8			
P25/Zr	Anatase	87.2	20-30	51.06±0.03	1.2±0.1/-
	Rutile	12.8			
$P25/Cu_{0.1}$	Anatase	86.4	20-30	46.27±0.04	-/0.09±0.03
	Rutile	13.6			
$P25/Cu_{0.5}$	Anatase	87.3	20-30	42.96±0.04	-/0.27±0.03
	Rutile	1.6			
$P25/Zr/Cu_{0.1}$	Anatase	86.5	20-30	50.92±0.04	1.1±0.1/0.08±0.03
	Rutile	13.5			

As it is evident from the figure, only characteristic peaks belonging to P25 are found for all modified TiO_2 samples. No separate Cu or Zr ions containing crystalline phases have formed during preparation. Phase composition of photocatalysts according to X-ray data is about 87.0 % anatase and 13.0 % rutile (Table 1).

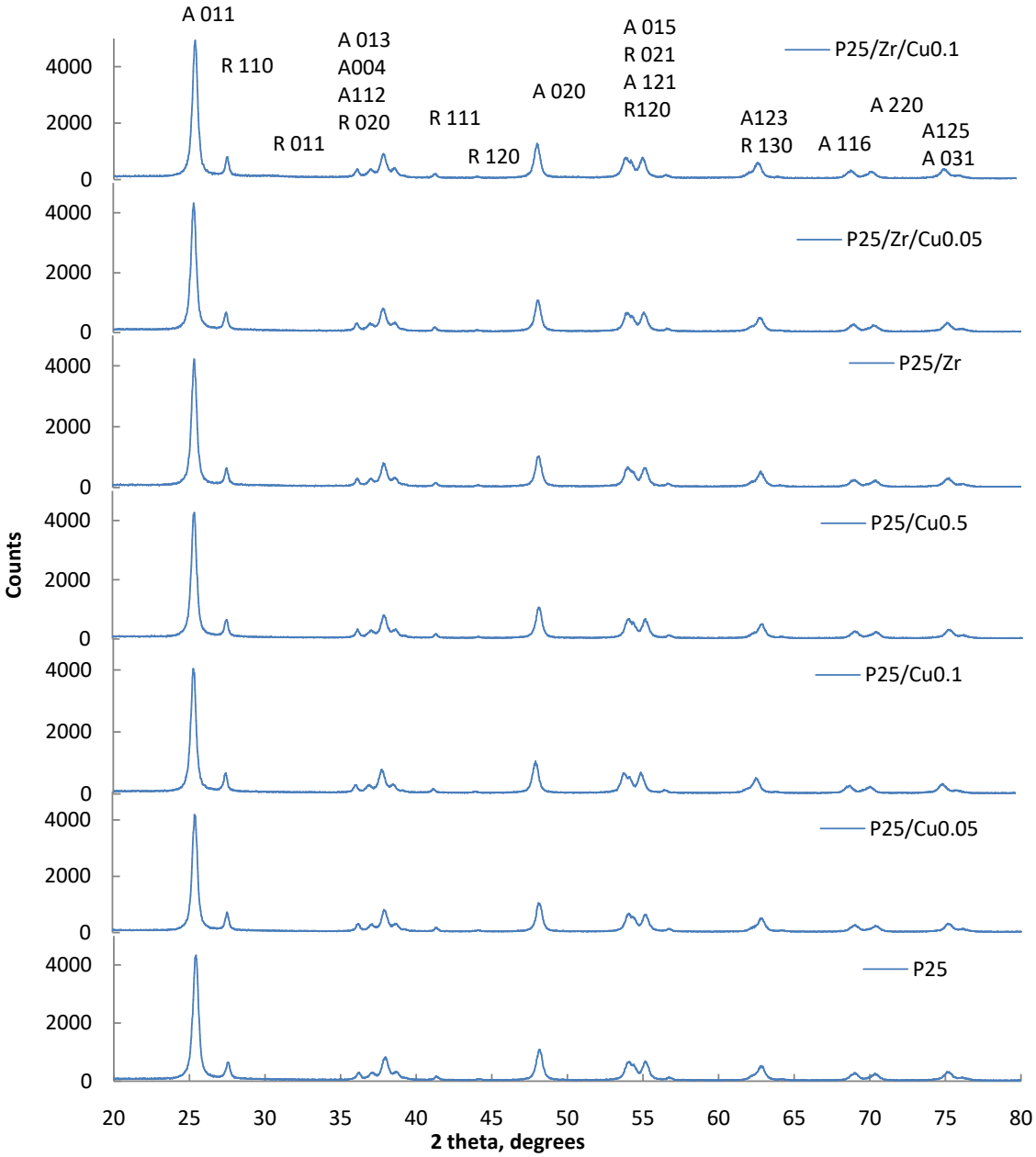

Fig. 10. X-ray diffraction patterns of P25 and Cu and Zr modified P25 photocatalysts.

As it is evident from the Table 1, introduction of copper and zirconium does not affect the phase composition. It does not significantly affect the specific surface area (SSA) of the catalyst, which usually has a great impact on the photocatalytic activity of the sample. Determined SSA of the reference catalyst P25 is 48.45±0.04 m^2/g, which is in good agreement with data published in the literature (Suttiponparnit et al. 2011), (Jafry et al. 2011). Usually, because of heterogeneity of the particles the range of SSA reported for P25 is between 46 and 53 m^2/g. All the obtained results are in good agreement with literature (Di Paola et al. 2002), (Hernández-Alonso et al. 2006), however, the SSA changes are within the error range of 5% and cannot be taken into account as reliable differences.

The photocatalytic test of Cu and Zr modified P25 was performed with MB dye as a model pollutant. The kinetics of MB decomposition is well described by the first order reaction for synthesized catalysts (Fig. 11).

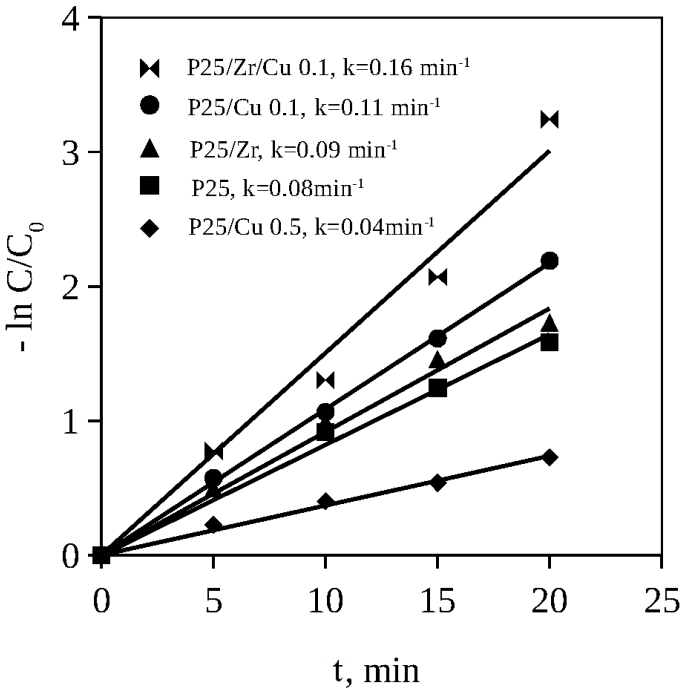

Fig.11. Photocatalytic MB decolorization promoted by Cu and Zr modified P25 nanoparticles under the simulated solar light (determined rate constants (k±0.01, min^{-1}): 0.08 for P25, 0.09 for P25/Zr, 0.11 for P25/$Cu_{0.1}$, 0.04 for P25/$Cu_{0.5}$, 0.16 for P25/Zr/$Cu_{0.1}$).

Evaluation of photocatalytic efficiency, obtained by MB decolorization, suggests that introduction of 0.1 mol % of Cu ions improves efficiency of the TiO_2 nanocomposite by 9 %. Nevertheless, higher loading of Cu results in a photocatalytic efficiency decrease by ~28 %. Introduction of 1 mol % of Zr shows only slight increase in the efficiency (~2 %). These results are in good agreement with previous studies (Hernández-Alonso et al. 2006), (Li et al. 2008). Simultaneous loading of Zr and 0.1 mol % of Cu to the P25 nanoparticles results in 16 % efficiency increase of TiO_2 photocatalyst.

Discoloring of dyes usually appears due to the destruction of chromophore, which is responsible for color. However, the main molecular structure of dye is not easily degradable. In order to explore the ability of the photocatalyst to mineralize the model pollutant, TOC analysis before and after photodegradation of MB was determined.

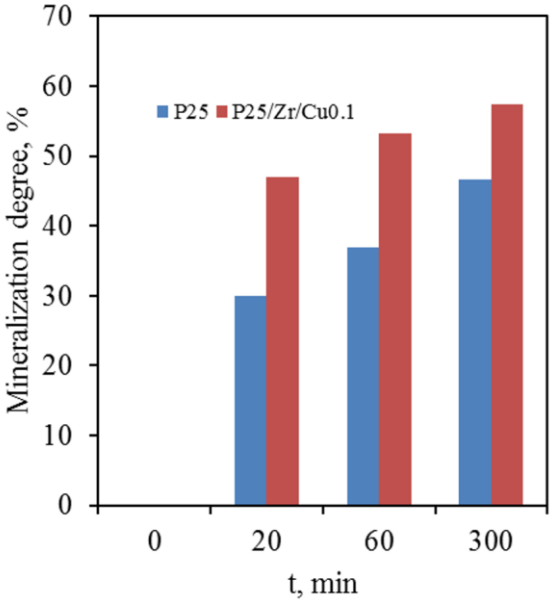

Fig. 12. The photocataltytic mineralization of MB with P25 and P25/Zr/$Cu_{0.1}$ catalysts determined by TOC measurements.

After 20 min of irradiation 80 % of MB was discolored by P25 catalyst. The level of mineralization reached 30 %. By contrast, improved mineralization efficiency was achieved with P25/Zr/$Cu_{0.1}$ catalyst showing 96 % of MB discoloration and 46 % of mineralization level after 20 min reaction time. No traces of organic nitrogen after this time were detected, demonstrating breakdown of

nitrogen-containing groups in MB molecules by this time. Fig. 12 shows that with extension of reaction time the mineralization degree is raising, reaching 57 % in 300 minutes for P25/Zr/$Cu_{0.1}$ catalyst.

As the MB dye was suspected to degrade through the photosensitization, which could prevail over photocatalytic pathway under the visible light, it was interesting to check if the tendency in behavior of Cu and Zr modified photocatalysts remains the same at the presence of another pollutant. As alternative model pollutant terephthalic acid was chosen. Terephthalic acid is one of the well-known environmental organic probes since its derivatives are used in synthesis process of variety of chemical compounds (Thiruvenkatachari et al. 2007). With regard to MB, slightly different trend was traced for TPA degradation by following the concentration of HTPA (Fig. 13). It can be seen from Fig. 14 that in case of HTPA formation better photocatalytic activity of the modified samples with respect to unmodified P25 was not detected. However, addition of both Cu and Zr to the TiO_2 surface still showed better result than single Cu or Zr modified TiO_2.

The lowered photocatalytic activity registered for Cu modified TiO_2 with respect to the P25 and shape of kinetic curves (Fig. 13) is an open question needed more experimental data. However, it may be attributed to the limitations of the method used, where the main analytical signal is the formation of fluorescent intermediate – HTPA. The evaluation of the photocatalytic activity using TPA degradation process in aqueous solution relies only on TPA to HTPA transformation and completely ignores decomposition of TPA through other pathways, affecting the observed results (Bubacz et al. 2013).

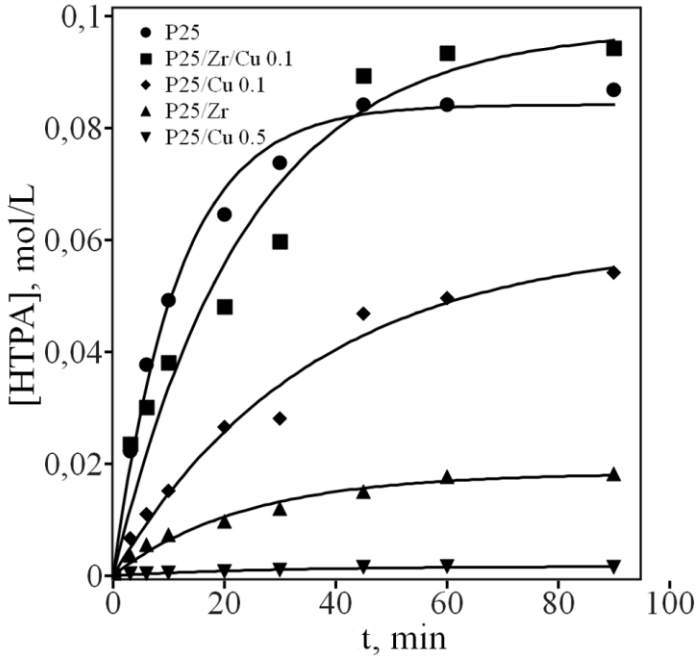

Fig. 13**.** The kinetics of HTPA formation with Cu and Zr modified P25 catalysts (determined rate constants ($k \pm 1 \cdot 10^{-4}$, min^{-1}): $7 \cdot 10^{-3}$ for P25, $6 \cdot 10^{-5}$ for P25/Zr, $2 \cdot 10^{-3}$ for $P25/Cu_{0.1}$, $8 \cdot 10^{-4}$ for $P25/Cu_{0.5}$, $4 \cdot 10^{-3}$ for $P25/Zr/Cu_{0.1}$).

The morphology of all copper and zirconium modified TiO_2 nanoparticles studied by SEM reveals that there is no impact of additives on the shape and the size of the particles (Fig. 14a, b). The average size of the primary nanoparticles remains stable for all compounds and lies in the range of 20 to 30 nm. In order to inspect the loading of Cu and Zr in synthesized catalysts, EDX analysis was carried out. Analysis shows that measured concentrations of copper and zirconium in prepared catalysts are in good agreement with their theoretical concentrations, except for 0.5 mol % of Cu, where concentration appears to be ~50 % lower than theoretical Cu loading (Table1). Nevertheless, it is worth mentioning that Cu loadings are close to detection limit and reliable measurement is achieved for zirconium only (Goldstein et al. 2003).

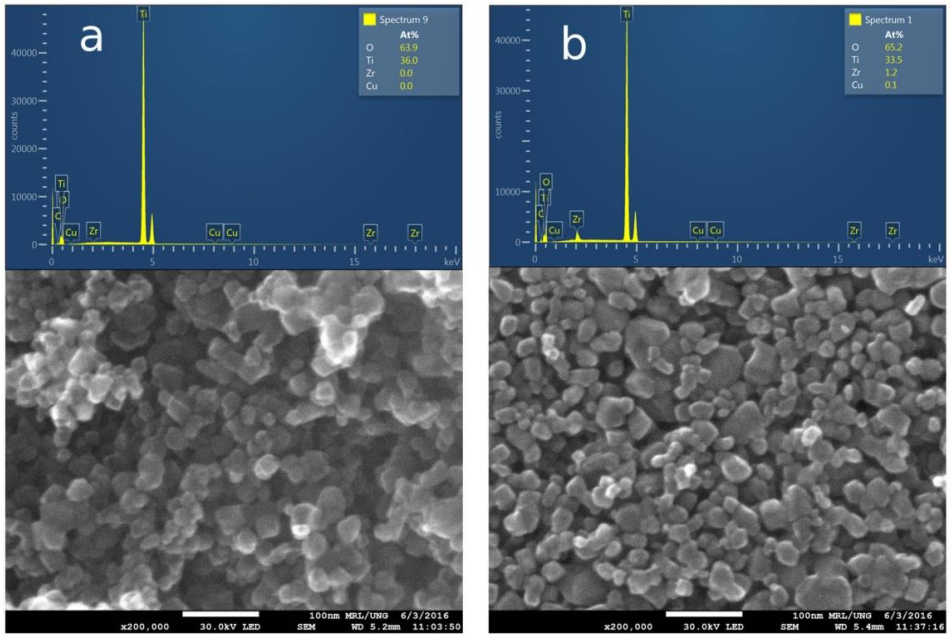

Fig. 14. SEM images and qualitative EDX spectra of a) unmodified P25 and b) P25/Zr/$Cu_{0.1}$.

Calcination step is crucial in utilized wet impregnation method as nitrogen-containing residuals can influence the efficiency of prepared catalyst. Data of the thermal decomposition of $Cu(NO_3)_2 \cdot 2.5H_2O$ into CuO at 200 – 250 °C (Morozov et al. 2003) and $ZrO(NO_3)_2$ into ZrO_2 at 575 °C (Wendlandt 1956), implies that calcination at 500 °C should be enough to remove all nitrogen residuals. In order to check this assumption, we additionally checked nitrogen presence by EDX. Indeed, no nitrogen was detected in any of the samples, justifying assumption described above.

The photocatalytic activity is closely related to the size of nanoparticles, so the particle size is an important factor, which needs to be properly defined. However, the electrostatic interaction between nanoparticles in water medium results in secondary particles (Domingos et al. 2009). Therefore, the size of the agglomerated nanoparticles was used as characteristic parameter to be considered for suspended catalyst in water. Results of DLS measurements are presented in Fig. 15. It should be noted that Cu modified particles have higher tendency for agglomeration and the size of agglomerates rises with time, which could negatively affect their photocatalytic activity. The obtained results of lower photocatalytic activity with higher copper loading can be elucidated with the strengthened agglomeration tendency of the

samples. The polymeric surface modification (Phenrat et al. 2008) can be applied to decrease the impact of agglomeration promoted by the metal ions. Nevertheless, it is important to notice that Zr showed an ability to lower Cu induced agglomeration, most probably by changing the surface properties of the material (Fu et al. 1996).

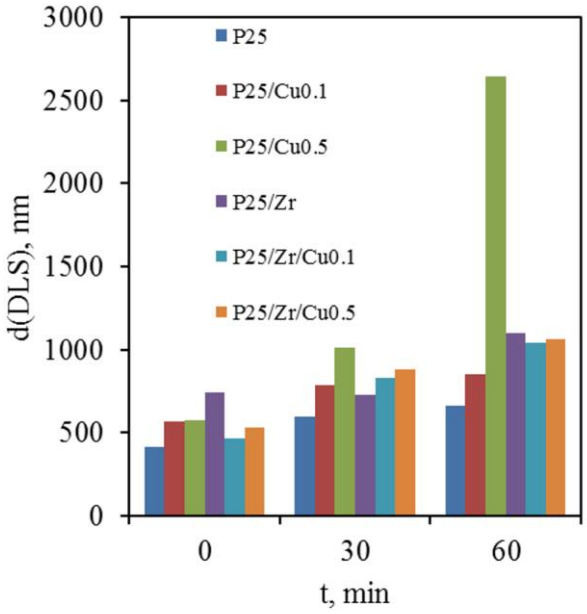

Fig. 15. The mean diameter of agglomerates of Cu and Zr modified P25 measured by DLS at three time intervals (0, 30, 60 min) after 1h stabilization of ultrasonically treated suspension.

The adsorption, or bonding of Cu cations on the surface of TiO_2 particles, with the consequent formation of Cu-O-Ti bridges, was stated as the key mechanism that facilitates charge separation in TiO_2 particles (Li et al. 2008). Therefore, we used Cu K-edge EXAFS and XANES analysis to monitor the local Cu neighborhood in the catalysts and to identify copper coordination and valence state, and copper species in the synthesized nanocomposites. Normalized Cu K-edge XANES spectra of the catalysts together with the spectra of attributing Cu compounds are shown in Fig. 16.

As a rule, valence state of Cu cation can be determined from the energy position of the Cu K-edge. The change in energy (about 4 eV) of the Cu K-edge is observed with Cu^+ to Cu^{2+} conversion (Lytle et al.1988), (Manceau and Matynia 2010), (Norma et al. 2005). The energy position of Cu K-edge in P25/Zr/$Cu_{0.1}$ and P25/Zr/$Cu_{0.5}$ calcined at 500 °C, coincides with the energy position of Cu^{2+} reference

compounds (Fig. 17), so we can conclude that Cu cations in the photocatalysts are in divalent form. The same conclusion can be drawn for Cu cations in the photocatalyst precursor, dried at 150 C, before calcination.

The comparison of the Cu K-edge profiles of the catalyst samples clearly indicates differences in the local symmetry of Cu^{2+} cation in P25/Zr/$Cu_{0.1}$ and P25/Zr/$Cu_{0.5}$ sample calcined at 500 °C (Fig. 16). The pre-edge shoulder in the calcined P25/Zr/$Cu_{0.1}$ sample is more pronounced and positioned at lower energy (8985 eV) than in the calcined P25/Zr/$Cu_{0.5}$ or in the P25/Zr/$Cu_{0.1}$ dried at 150°C, before calcination (where the shoulder is at 8987 eV). The shoulder appears in case of octahedral Cu^{2+} coordination, tetragonally distorted due to the Jahn-Teller effect. In previous studies it was attributed to the 1s to 4p dipole excitation (Lytle et al. 1988), (Frenkel et al. 2000), (Manceau and Matynia 2010). In CuO the shoulder's energy position is at 8985 eV.

The spectrum of the calcined P25/Zr/$Cu_{0.1}$ sample can be defined as a linear combination of CuO (72 %), $CuSO_4 \cdot 5\ H_2O$ (15 %) and $Cu(OH)_2$ (13 %) spectra. The same XANES spectra, but with different relative ratios: CuO (52 %), $CuSO_4 \cdot 5\ H_2O$ (16 %) and $Cu(OH)_2$ (32 %) can be used for the best description of the P25/Zr/$Cu_{0.5}$ spectra. The spectrum of the P25/Zr/$Cu_{0.1}$ precursor dried at 150 °C can be fitted by two reference spectra $CuSO_4 \cdot 5\ H_2O$ (35 %) and $Cu(OH)_2$ (65 %), without any CuO.

The Cu K-edge EXAFS analysis was used to arbitrate the structure around Cu cations in the photocatalysts. Fourier transform (FT) of Cu EXAFS spectra of the P25/Zr/$Cu_{0.1}$ sample after drying at 150 °C, and calcined at 500 °C, and P25/Zr/$Cu_{0.5}$ sample calcined at 500 °C are shown in Fig. 16. The first peak between 1 Å and 2.2 Å is contributed by oxygen neighbors in the nearest coordination shell. More distant Cu neighbors contribute weaker peaks between 2.5 Å and 3.5 Å. Qualitative comparisons of the FT spectra clearly show that average Cu neighborhood in the samples is not the same.

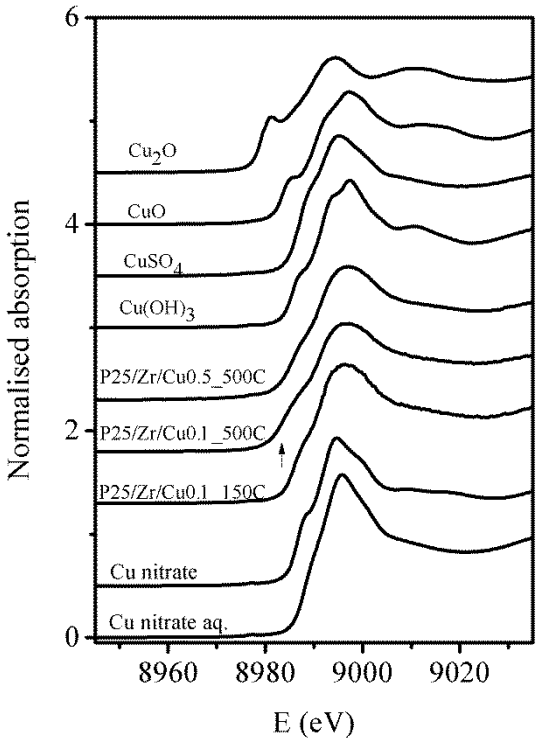

Fig. 16. Cu K-edge XANES spectra of the P25/Zr/$Cu_{0.1}$ sample after drying at 150 °C, and calcined at 500 °C, and P25/Zr/$Cu_{0.5}$ sample calcined at 500 °C. Reference Cu^{+} and Cu^{2+} copper compounds with different Cu cation coordinations (Cu_2O, CuO, $CuSO_4$ ·5 H_2O, $Cu(OH)_2$, $Cu(NO_3)_2$·2,5H_2O crystalline and 0.1 M aqueous solution of $Cu(NO_3)_2$) are shown for comparison. The spectra are shifted vertically for clarity. The pre-edge shoulder at 8983 eV in the calcined P25/Zr/$Cu_{0.1}$ sample is indicated by the arrow.

The structural parameters were determined by comparison of the measured and model EXAFS spectra. It should be stressed, however, that two or more Cu^{2+} species with different copper cation neighborhood may coexist in each sample, and the resulting EXAFS signal represents average Cu neighborhood in the sample.

Our EXAFS model was composed of six oxygen atoms in the nearest Cu coordination shell at two different distances, nitrogen or oxygen neighbors in the next shell and Ti, Cu and/or Zr neighbors at larger distances. Types of atoms in neighbor shells are resolved in the EXAFS analysis by the characteristic photoelectron backscattering factor and phase shift, however, atoms with consecutive atomic numbers, such as O and N, produce a very similar backscattering amplitudes and phase shifts, and are therefore difficult to resolve from each other.

The EXAFS model included three variable parameters for each shell of neighbors: the coordination number, the distance to the neighbor atoms and the Debye-Waller factor. The amplitude-reduction factor S_0^2 was fixed at the value of 0.85. A common shift of energy origin ΔE_o was also varied for each shell. To improve the stability of the fit and reduce parameter uncertainties, a parallel fit of all three EXAFS spectra was performed, where some of the parameters were constrained to common values. We used same Debye-Waller factors for the same type of neighbors in each coordination shell, and same values for the Cu-Ti, Cu-Cu interatomic distances in all three sample spectra.

An excellent EXAFS fit (Fig. 17) was obtained in the R range of 1 to 3.5 Å and in the k range of 2.5 – 11 $Å^{-1}$ in case of P25/Zr/$Cu_{0.1}$ and 3.0–11.8 $Å^{-1}$ in case of P25/Zr/$Cu_{0.5}$sample. Best fit parameters are given in Table 2.

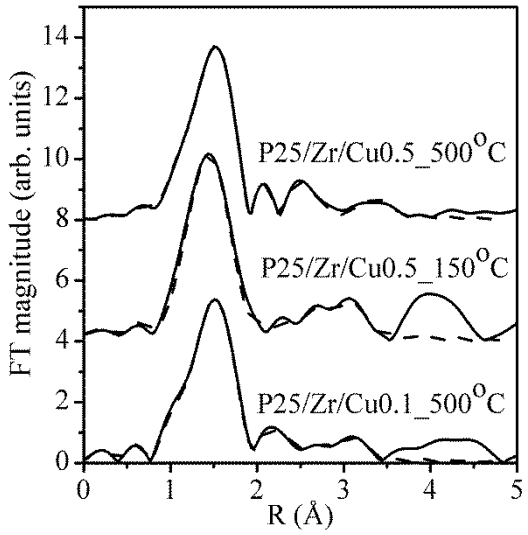

Fig. 17. Fourier transform magnitude of k^3-weighted Cu EXAFS spectra of the P25/Zr/$Cu_{0.1}$ sample after drying at 150 °C, and calcined at 500 °C, and P25/Zr/$Cu_{0.5}$ sample calcined at 500 °C, calculated in the k range of 2.5 - 11 $Å^{-1}$ and R range of 1 to 3.5 Å. Experiment – (solid line); model -- (dashed line).

Cu EXAFS results show that Cu atoms in all three samples are coordinated to six oxygens in a distorted octahedron: four oxygen atoms in the equatorial plane are at shorter Cu-O distance (1.91 Å - 1.94 Å), and two oxygen atoms on axial positions

at longer distance (2.33Å - 2.43 Å). The differences between the equatorial and axial Cu-O distances are slightly distinct for the three samples.

Table 2. Parameters of the nearest coordination shells around Cu cations in the P25/Zr/$Cu_{0.1}$ sample after drying at 150 °C, and calcined at 500 °C, and in the P25/Zr/$Cu_{0.5}$ sample calcined at 500 °C: average number of neighbor atoms (*N*), distance (*R*), and Debye-Waller factor (σ^2). Uncertainty of the last digit is given in parentheses. A best fit is obtained with the amplitude reduction factor $S_0^2 = 0.85$. The shift of the energy origin ΔE_o and *R*-factor (quality of fit parameter), are listed in the last column.

Cu	*N*	*R* [Å]	σ^2	ΔE_o/*R*-factor
P25/Zr/$Cu_{0.1}$ 150 °C				
O	3.8(5)	1.91(2)	0.008(2)	-7 ± 3 eV/ 0.0095
O	2.2(5)	2.43(4)	0.008(2)	
N	2(1)	2.73(3)	0.008(2)	
Ti	1.0(5)	3.03(3)	0.012(2)	
Cu	1.0(5)	3.36(6)	0.007(2)	
P25/Zr/$Cu_{0.1}$ 500 °C				
O	3.8(3)	1.94(1)	0.008(2)	-6 ± 2 eV/ 0.0029
O	2.2(3)	2.38(1)	0.008(2)	
O	2.0(4)	2.71(3)	0.008(2)	
Ti	0.7(3)	3.03(3)	0.012(2)	
Cu	1.1(5)	3.36(6)	0.011(2)	
P25/Zr/$Cu_{0.5}$ 500 °C				
O	3.9(3)	1.92(1)	0.008(2)	-8 ± 2 eV/ 0.0014
O	2.1(3)	2.33(4)	0.008(2)	
O	2.2(2)	2.57(6)	0.008(2)	
Ti	1.1(2)	2.92(6)	0.012(2)	
Zr	3(2)	3.63(6)	0.020(6)	

Two nitrogen atoms at 2.73 Å in the P25/Zr/$Cu_{0.1}$ sample dried at 150 °C were found. Nitrogen could be ascribed for two nitro groups attached to copper cation forming Cu-O-N bridges. After calcination at 500 °C two nitrogen neighbors are replaced with two oxygen neighbors at about the same distance.

It must be taken into account that the atoms with consecutive atomic numbers, such as O and N, cannot be uniquely resolved due to similar scattering amplitudes and phase shifts. However, we can exclude the presence of N neighbors in the samples, after heat treatment at 500 °C, based on the data of the thermal decomposition of $Cu(NO_3)_2 \cdot 2{,}5H_2O$ into CuO at 200-250 °C (Morozov et al. 2003). In the calcined P25/Zr/$Cu_{0.5}$ sample we also identified two oxygen neighbors in the second coordination shell, but at shorter Cu-O distance of 2.57 Å.

In more distant coordination shells one Ti neighbor was found in all three samples, clearly indicating the formation of Cu-O-Ti bridges already in the dried precursor. The Cu-O-Ti linkages are retained after calcination at 500 °C. The Cu-Ti distance is shorter in the P25/Zr/$Cu_{0.5}$ sample compared to P25/Zr/$Cu_{0.1}$ samples.In both P25/Zr/$Cu_{0.1}$and P25/Zr/$Cu_{0.5}$samples we identified the formation of Cu-O-Cu connections: in a dried and in calcined samples we found one Cu neighbor at the distance of 3.35 Å.

Conclusions

Modification of commercial TiO_2 nanoparticles (Aeroxide® Degussa P25) was performed with Zr and Cu oxides simultaneously. It has been shown that there is no impact of additives on the crystal structure, shape and size of the primary P25 nanoparticles. Modification did not significantly affect to specific surface area of the materials. However, Cu ions loading led to pronounced agglomeration of primary TiO_2 particles to bigger secondary particles in the water solution. It has been shown that Zr ions loading led to lowering of copper modified secondary particles growth.

X-ray absorption spectroscopy (XANES) allowed to confirm that copper ions are present at divalent form in the TiO_2 based composites. The formation of Cu-O-Ti linkages is confirmed by the EXAFS analysis.

The 1st hypothesis of the thesis is confirmed. It has been shown that P25 modification with Cu/Zr ions simultaneously at specific concentrations is beneficial for model pollutants decomposition under the simulated solar light. Presence of Zr and Cu sites simultaneously help to reach deeper mineralization level of methylene blue in shorter time. The higher activity of these double metal modified samples is well correlated with suppressed agglomeration of primary nanoparticles in aqueous solution and retained Cu-O-Ti bridges in the nanostructured material.

3.2. EVALUATION OF THE SECOND HYPOTHESIS.

Hypothesis 2. ***Cu and Zr oxides form Cu-O-Zr moieties on the surface of TiO_2 that beneficially contribute to the photocatalytic activity of TiO_2.***

Cu AND Zr SURFACE SITES IN PHOTOCATALYTIC ACTIVITY OF TiO_2 NANOPARTICLES: THE EFFECT OF Zr DISTRIBUTION

After the first part of the work was completed, it was important to take into account the difficulties and probable shortcomings revealed from the photocatalysts synthesis technique and photocatalytic activity evaluation method. The TiO_2 particles aggregation into larger secondary particles discussed in the previous chapter was possibly connected to the waterborne synthesis technique applied for the photocatalysts production. A decision was made to change the photocatalysts synthesis conditions from water to ethyl alcohol medium. The inorganic metal precursors were changed to organic metal precursors, *i.e.* copper(ll) acetyl-acetonate and zirconium(lV) butoxide. The methylene blue dye was changed for the more stable and persistent dye Reactive Blue 19.

Towards the characterization of obtained materials, some major visual variations were first observed. The powders with copper loading were different in color, showing intensification of green-brownish shade with increased Cu concentration. Powders with Zr loading retained white appearance. The same trend was observed also with the samples obtained from inorganic metal precursors.

Considering that the photocatalysts were developed for water purification purpose, the immobilization of the active materials is an important aspect. The prepared powders of copper and zirconium modified TiO_2 were mixed with binder sol and immobilized on the glass plates. The results of scratch resistance tests of the layers of the Zr/Cu modified TiO_2 photocatalysts are presented in Fig. 18.

It is evident, that Cu modification leads to formation of less resistant coatings. The hardness of the film obtained from the powder with 0.5 mol % of Cu drops by 4 units compared to film obtained from unmodified P25. In a contrast, application of both elements simultaneously (Zr and Cu) leads to formation of films with better hardness characteristics compared to the films with only copper loading. The results are probably the consequence of the agglomeration process we keep on observing for the copper modified samples and discussed in previous chapter. The connection

between the size of the secondary particles and resulting mechanical resistance of the photocatalytic layers is described elsewhere (Kete et al. 2014). It was clearly shown that catalytic layers made of bigger secondary particles end up with mechanically less resistant coatings which was suspected to the formation of layers with higher macro-porosity.

The changes in crystalline structure were checked by X-ray diffractometry (XRD). Alike for the samples obtained from inorganic precursors, only peaks responsible for anatase and rutile phases from P25 were observed. The absence of XRD reflections of copper and zirconium crystalline phases on the XRD patterns can be attributed to low amount and fine dispersion of copper and zirconium species on the TiO_2 surface. The unit cell parameters and phase content of obtained photocatalysts are presented in Table 3. It is clearly seen that with modification there is a slight growth from 23 to 26 nm and from 17 to 18 nm of crystallites for rutile and anatase, respectively.

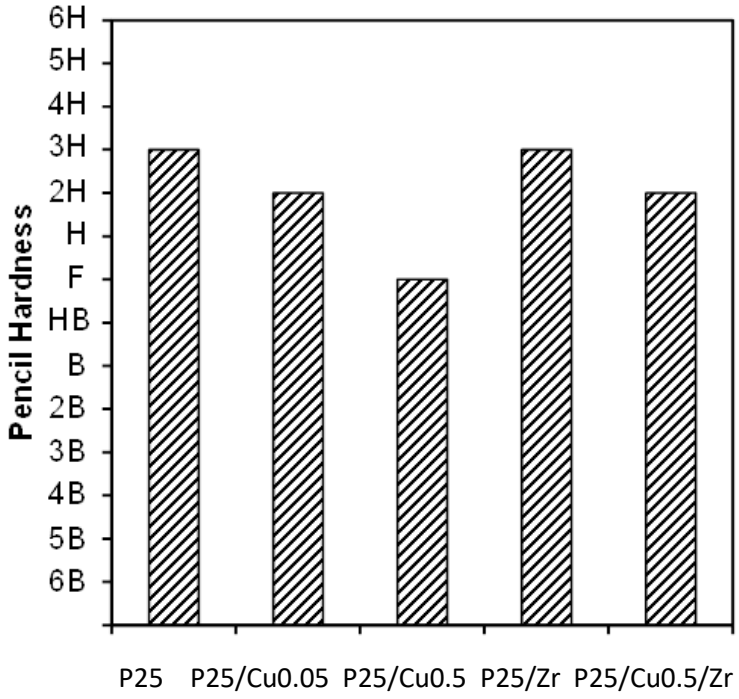

Fig 18. Scratch resistance test of immobilized layers of photocatalysts (6H – the hardest, 6B – the softest pencil).

Table 3. Data from X-ray diffraction patterns and copper/zirconium loading of Cu/Zr modified P25 photocatalysts.

Sample	Phase and the № of ICSD reference file	Goodness of fit	Phase content, %	Crystallite size, nm	Crystal cells parameters			Cu/Zr content, mol %	
					Volume x 10^6, pm^3	a =b	c	Theoretical	Determined*
P25	Anatase 96-900-8214	1.9	87.2	17	136.4929 ±0.0009	3.7880 ±0.0002	9.5124 ±0.0005	-	-
	Rutile 96-900-7433		12.8	23	62.513 ±0.001	4.5950 ±0.0004	2.9608 ±0.0005		
P25/$Cu_{0.05}$	Anatase 96-900-8214	1.9	86.4	18	136.4296 ±0.0009	3.7873 ±0.0002	9.5115 ±0.0005	0.05	0.06± 0.01
	Rutile 96-900-9084		13.6	26	62.513 ±0.001	4.5956 ±0.0004	2.9599 ±0.0004		
P25/$Cu_{0.1}$	Anatase 96-900-9087	1.8	87.2	18	136.2691 ±0.0009	3.7858 ±0.0002	9.5081 ±0.0005	0.10	0.14± 0.01
	Rutile 96-900-9084		12.8	26	62.422 ±0.001	4.5934 ±0.0004	2.9585 ±0.0004		
P25/$Cu_{0.5}$	Anatase 96-900-8214	1.9	87.3	18	136.3369 ±0.0009	3.7866 ±0.0002	9.5087 ±0.0005	0.5	0.56± 0.04
	Rutile 96-900-7433		12.7	26	62.452 ±0.001	4.5938 ±0.0004	2.9594 ±0.0004		
P25/Zr	Anatase 96-900-8214	2.0	87.6	18	136.3624 ±0.0009	3.7867 ±0.0002	9.5097 ±0.0006	1.0	0.2± 0.1
	Rutile 96-900-4142		12.4	26	62.475 ±0.001	4.5941 ±0.0005	2.9601 ±0.0005		
P25/Zr/$Cu_{0.05}$	Anatase 96-900-8214	2.0	87.5	17	136.3478 ±0.0009	3.7866 ±0.0002	9.5093 ±0.0006	0.05 /1	0.07± 0.01/ 0.2± 0.1
	Rutile 96-900-4142		12.5	26	62.448 ±0.001	4.5932 ±0.0005	2.9600 ±0.0005		
P25/Zr/$Cu_{0.1}$	Anatase 96-900-9087	2.0	87.8	18	136.2388 ±0.0009	3.785503± 0.000196	9.507224± 0.000542	0.10 /1	0.12± 0.01/ *0.2 ±0.1
	Rutile 96-900-7433		12.2	26	62.403 ±0.001	4.592827± 0.000434	2.958315± 0.000463		

The loading of copper as determined by complexometric titration is in good agreement with theoretical one (Table 3). The loading of Zr, as resulting from EDX analysis, is constant in all the samples but lower than the nominal 1 mol %.The Zr content has been determined by standardless EDX analysis and±0.01 mol % is only the statistical part of the uncertainty. Important systematic errors are possible in EDX analysis of compressed powders performed without standards, as in our case, which can affect the accuracy to a greater extent.

A lot of work has been done applying Cu ions as a surface modifier, because of its ability to bring beneficial shift of absorption edge of the photocatalyst to visible part of the sunlight spectrum. TiO_2 coupled with copper oxides exhibits desired red shift because of the narrow band gap of copper oxides. The absorption edge of Cu/Zr modified TiO_2 was checked by UV-Vis diffuse reflectance spectroscopy (DRS). Reflectance curves transformed to Kubelka Munk absorption units are presented in Fig. 19. It was possible to register additional absorption shoulder at ~450 nm which is growing at higher Cu loading. In the samples modified with Zr this shoulder does not occur, but it persists at combined Cu/Zr modified samples. The shoulder about 450 nm is attributed to the presence of CuO nanoclusters (Lin et al. 2015). An additional broad band appears at about 700 nm and it can be attributed to the d-d transition of Cu in an (pseudo-) octahedral environment in CuO.

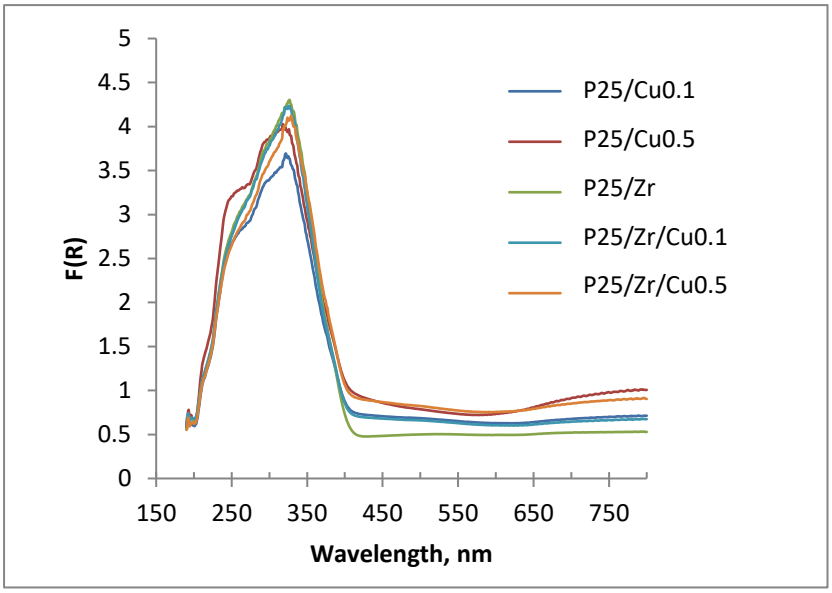

Fig. 19. Kubelka-Munk transformed UV-Vis reflectance of powder Cu/Zr modified TiO_2 photocatalysts.

A very common technique to evaluate the capability of photocatalysts to act under the visible light is by determining the apparent band gap of the material. The results obtained from commonly used technique, which is estimation of band gap from the Kubelka-Munk curves, are presented in Table 4. It is clearly seen, that the values of estimated band gaps of examined powders do not differ for more than 3 % and may not significantly influence the result of visible light activity.

Table 4. The band gaps of P25 modified with Cu and Zr ions estimated from Kubelka Munk curves.

Sample	Indirect	Direct
P25	3.09	3.46
P25/$Cu_{0.05}$	3.04	3.45
P25/$Cu_{0.1}$	2.99	3.36
P25/$Cu_{0.5}$	2.99	3.37
P25/Zr	3.03	3.46
P25/Zr/$Cu_{0.1}$	3.04	3.36
P25/Zr/$Cu_{0.5}$	3.05	3.36

It is worth mentioning, that the energy gap measured by DRS is a characterization of a bulk material. However, with surface modification we are not changing the bulk, but the surface of the nanoparticles. So, the band gap measured by DRS is not the essential energy needed for understanding the behavior of the photocatalysts in aqueous solutions. In the solution determining role plays particle/solution interface.

When a semiconductor is placed in a solution containing redox species, electrons are transferred across the semiconductor/electrolyte interface until the equilibrium and CB and VB edges are bent so that a potential barrier is established against further electron transfer across the interface (Yong and Schoonen 2000). As a result, the energies of CB and VB edges at the semiconductor/electrolyte interface deviate from their bulk values. The development of a net charge at the particle surface affects the distribution of ions in the surrounding interfacial region.This liquid surrounding is the Helmholtz double layer. The potential that exists in Helmholtz double layer is known as Zeta potential. IEP is commonly expressed as pH at which zeta potential is equal to zero. The IEP of obtained Cu/Zr modified samples are presented in Fig. 20. It is clearly seen, that surface modification

influences the properties of catalyst/electrolyte interface. Low amount of CuO mounted on the surface of TiO_2 does not influence value of pH of zero charge (the results are in the error range of the measurements). In the same time, higher loading of CuO biases IEP towards higher pH. This fact can be logically explained by the formation of "islands" of CuO species on the top of TiO_2 with rising copper concentration. Formed CuO species (Cu-OH surface species) bring the properties intrinsic to the copper oxide with IEP lying at much higher pH of about 8.5 and 9.5 for Cu_2O and CuO, respectively (Butler 1978).

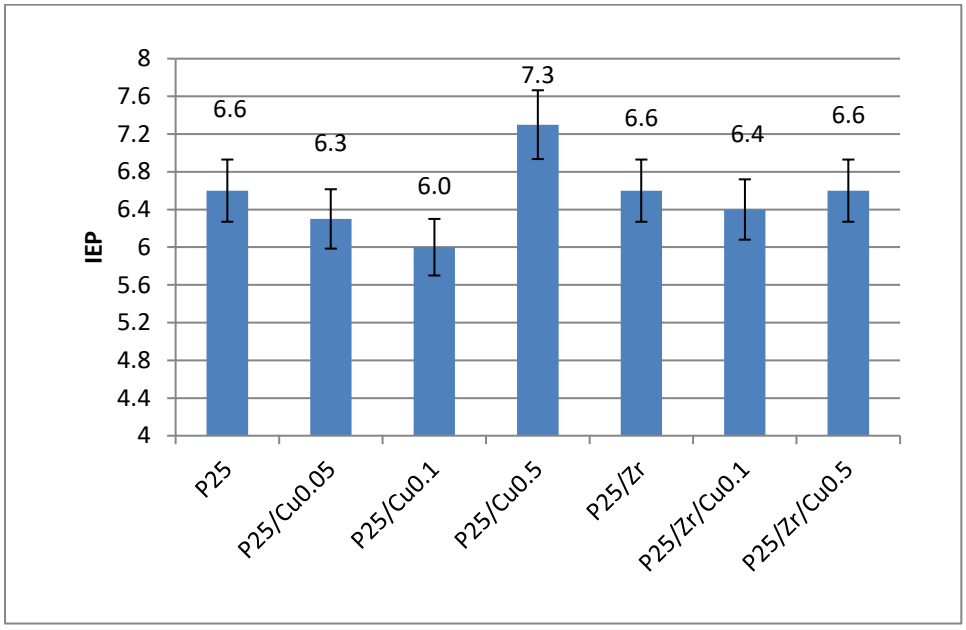

Fig. 20. Isoelectric point of Cu/Zr modified samples of TiO_2.

Surface modification with Zr keeps the IEP around the values characteristic to zirconium oxide (pH pzc = 6.7) (Butler 1978), which is not different from the IEP value obtained for the P25 sample (pH=6.6±0.4) (Fig. 20). Combined Cu/Zr modification reveals IEP close to unmodified TiO_2 or Zr modified TiO_2. This observation can be explained by dominant surface Zr-OH species.

The degradation of RB19 dye under simulated solar light was performed to test photocatalytic activity of these samples. Fig. 21 shows that the highest degree of dye degradation, calculated from the UV-Vis spectroscopy measurements (bleaching, 72 %) after 50 min of irradiation and the highest degree of mineralization calculated from the TOC data (83 %) after 3 h of irradiation, were recorded for the sample with the lowest (0.05 mol %) copper loading. According to (Irie et al. 2009), this enhancement can be explained by the formation of the mid-level Cu3d states. In this

case, upon irradiation an electron is localized at the copper nanocluster and a hole on the TiO_2 surface. The mid-level states enable the transition of electrons from the VB of TiO_2 to the empty CuO states and enhance electron/hole separation (Irie et al. 2009). At a higher copper loading, a lower level of dye degradation was observed: about 40 % of bleaching and 50 % of TOC reduction for 0.1 and 0.5 mol % of Cu loading. This result is consistent with the statement about the dependence of photocatalytic activity of copper modified photocatalysts from the amount of deposited copper oxide (Čižmar et al. 2018), (Jin et al. 2013). According to (Jin et al. 2013) the upward bands shift causes reverse localization of electrons and holes at higher copper loading, which leads to a weakened oxidation ability of the generated holes.

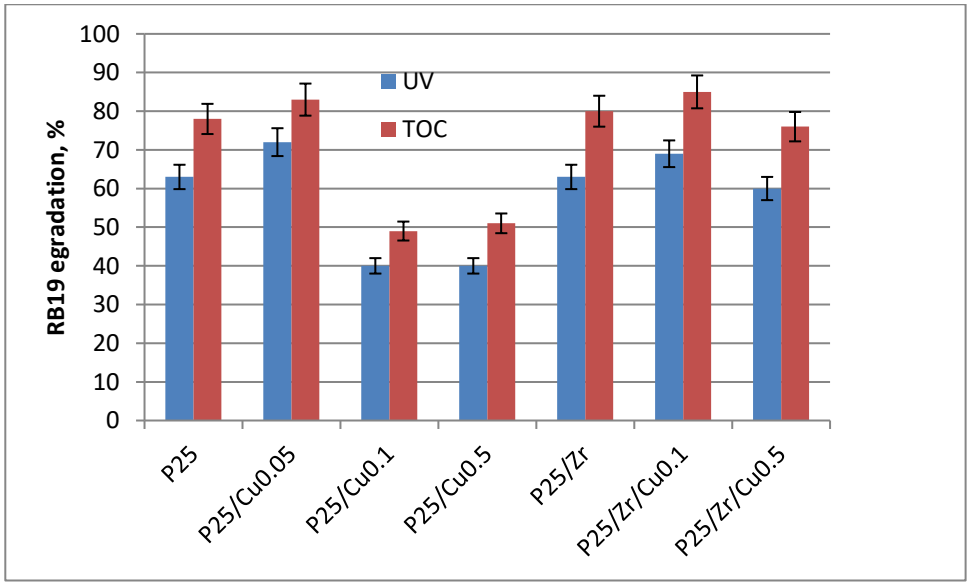

Fig. 21. Degradation of RB19 by Cu/Zr modified TiO_2. UV results correspond to calculated degree of dye degradation measured by UV-Vis spectroscopy (bleaching) after 50 min of light irradiation; TOC results correspond to calculated degree of dye degradation measured by means of total organic carbon after 3h of light irradiation.

It is interesting to observe that surface modification with 1 mol % of Zr-only (without copper) does not influence the photocatalytic performances of P25 towards RB19. In fact, in this case, about 63 % of bleaching and 80 % of TOC reduction is registered, which is within the error range of the result for unmodified P25. Our findings do not contradict results obtained by (Guerrero-Araque et al. 2017) who

showed, that beneficial defects induced by ZrO_2-TiO_2 heterojunction are not formed at low Zr loading.

At the same time, in the presence of copper, zirconium species play beneficial role for the dye degradation efficiency. In case of low copper loading (0.05 mol %) influence of Zr on photocatalytic activity is not detected: 69 % of bleaching and 85 % of TOC reduction for RB19 degradation by Cu/Zr modified sample versus 72 % of bleaching and 83 % of TOC reduction by Cu modified sample without addition of Zr. However, at higher copper loading (0.1 mol %), dye degradation efficiency of double metal modified photocatalyst rose to 60 % of bleaching and 76 % of TOC reduction compared to 40 % of bleaching and 50 % of TOC reduction performed by copper modified sample.

To understand the nature of the inhibition effect, more accurate analysis of the mechanism is required. According to the experimental results, the decrease in the reaction rate could be caused by the competitive side reaction between $HO^{\cdot}$ radicals and Cu ions.

To clarify this suggestion, the chemical oxidation of RB19 with Fenton's reagent in the presence of Cu/Zr modified TiO_2 in the dark was used. The Fenton reaction is a homogeneous reaction in which Fe^{2+}acts as a catalyst to initiate the decomposition of H_2O_2 and to generate $HO^{\cdot}$ radicals.

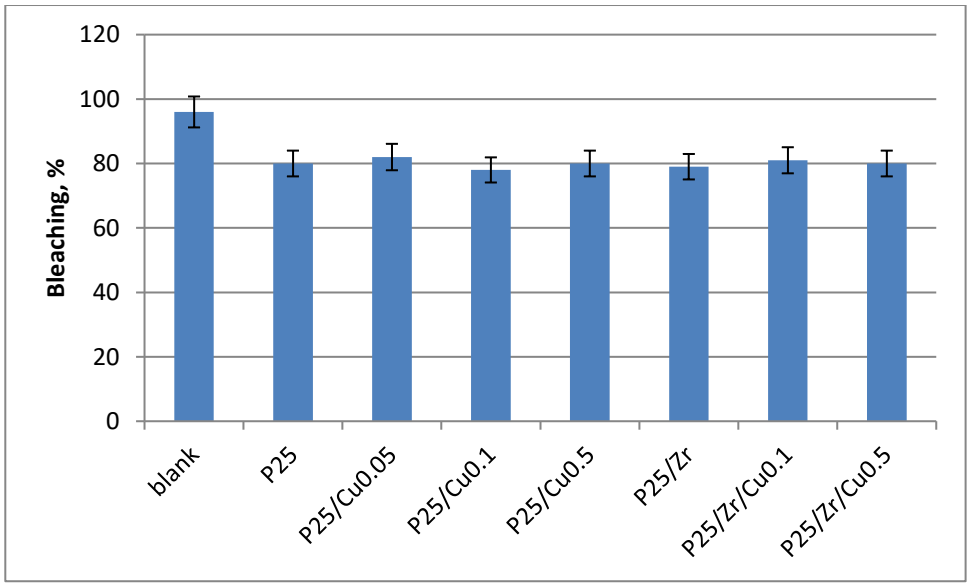

Fig. 22. The bleaching of RB19 by Fenton's reagent in the presence of Cu/Zr modified TiO_2.

The bleaching of RB19 by Fenton's reagent in the presence of Cu/Zr modified photocalysts is presented in Fig. 22. The blank test performed without photocatalytic powder showed RB19 bleaching by Fenton's reagent of about 96 %. P25 was used as a reference and showed decrease in bleaching for about 15 % compared to the blank test. All the experiments with diversity of surface modified samples showed the result within the errors range of experiment, about 80 % of RB19 bleaching. This result clearly suggests, that the lowering in photocatalytic efficiency of Cu modified TiO_2 is not connected to the $HO^{\cdot}$ radicals capturing by the copper species.

Further investigation of the Cu modified samples was performed with solid state EPR experiments. EPR spectroscopy represents a unique tool to follow the paramagnetic centers present in the TiO_2-based nanomaterials, character of which is determined by the synthetic procedure and further treatment applied as well as by the presence of a modifier (Pližingrová et al. 2017). Even though the main prerequisite to obtain an EPR spectrum is the presence of unpaired electron, which is not necessarily present in the modifier, the effect of the modifier presence on the structure of the photocatalyst may evoke the formation of paramagnetic centers in the TiO_2 lattice and such defects can be monitored by EPR.

EPR spectra of all studied samples were measured at room temperature and at 100 K using X- and Q-band EPR spectrometer. Since in the samples the presence of CuO clusters on the TiO_2 surface was expected and EPR spectroscopy enables the identification of Cu^{2+} as a paramagnetic $3d^9$ ion, the corresponding EPR spectra can confirm the presence and character of the surface modification with copper oxide. EPR spectra of the powdered Cu modified samples in the X-band monitored at room temperature and at 100 K exhibit an anisotropic EPR signal with a hyperfine structure due to I= 3/2 of Cu^{2+} typical for isolated mononuclear slightly axially distorted octahedral Cu^{2+} complexes (Fig.23 A). The hyperfine structure is well resolved for the $g_{\|} = 2.33$ where we observe a quartet with the hyperfine coupling constant of $A_{\|} \sim 14$ mT, while the perpendicular component of the g-tensor at $g_{\perp} = 2.04$ is present without resolvable hyperfine structure. Analogous EPR spectra were monitored previously for the TiO_2 nanostructures modified/doped with copper and attributed either to the surface-bound Cu^{2+} ions or to Cu^{2+} substituting lattice Ti^{4+}, which is coupled with the formation of oxygen vacancies (Li et al. 2008). EPR

spectrum measured at 100 K provides a better resolution of the above described signals and in addition a further signal of low intensity with the *g*-value lower than 2.00 is recognised. This signal can be assigned to the perpendicular component of the axially symmetric g-tensor $g_{\perp} = 1.97$ of Ti^{3+} centres in the anatase lattice (Pližingrová et al. 2017). The Q-band EPR spectra of Cu modified samples surprisingly do not give a better resolution of the hyperfine structure of the anisotropic Cu^{2+} signals, however increased sensitivity helps to confirm the identification of the EPR signal of T^{3+} centers (Fig.23 B). The corresponding EPR signal with the $g_{\perp} = 1.97$ and a non-resolved parallel *g*-tensor component is also observable only at low temperature measurement, due to the short spin-lattice relaxation time of T^{3+} centers, which hinders their detection at room temperature (Czoska et al. 2008). In addition to the EPR signals observed also in the X-band EPR spectra of Cu modified samples, the Q-band spectra, at room temperature as well as at 100 K, exhibit signal with $g \sim 2.00$. Analogous EPR signal was observed previously for the rutile nanostructures modified with copper annealed at 450 °C (Neubert et al. 2016).

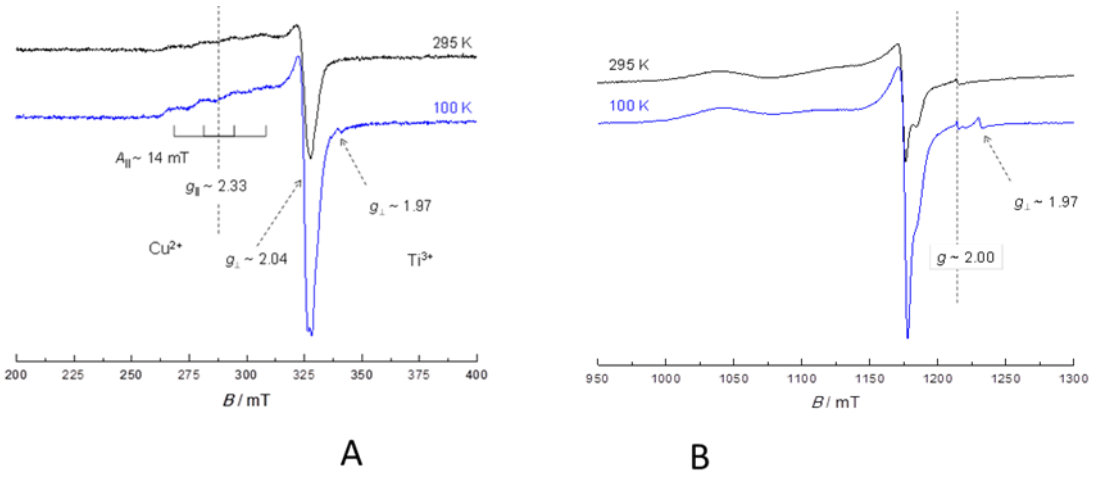

Fig. 23. (A) X-band and (B) Q-band EPR spectra of powdered P25/$Cu_{0.05}$ measured at 295 K or100 K.

Sample with Zr and Cu modification exhibits analogous EPR spectra as Cu only modified sample (Fig. 24).

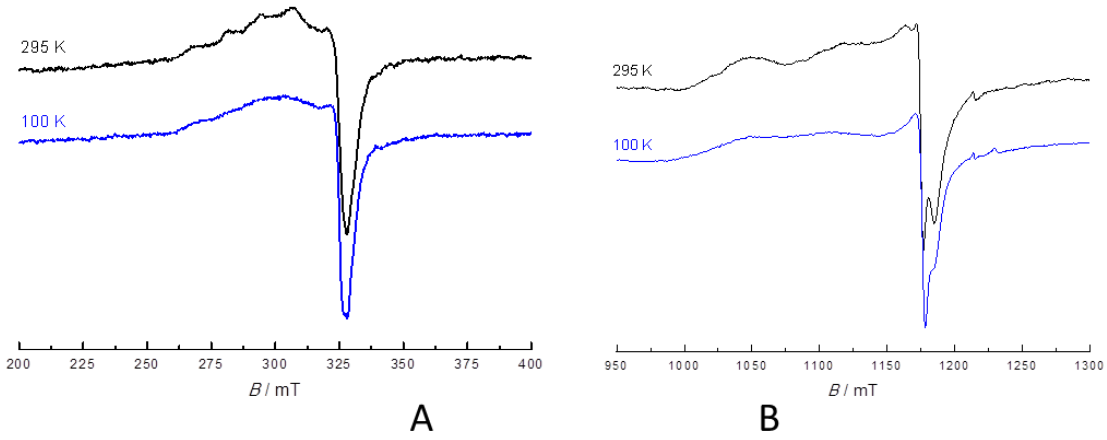

Fig. 24 (A)X-band and (B) Q-band EPR spectra of powdered P25/Zr/$Cu_{0.05}$ measured at 295 K or 100 K.

X-band EPR spectra of Zr surface modified sample exhibited low intensity EPR signal observable only at 100 K (Fig. 25 A). The analogous signal with $g_{\perp}$ = 1.97 and unresolved parallel component of the *g*-tensor attributed to Ti^{3+} centres in the anatase lattice was identified in all surface modified P25 samples. Also in the Q-band EPR spectra the signal at $g \sim 2.00$ was observed, reflecting the formation of oxygen vacancies upon annealing procedure up to 550 °C.

Photo excitation of water suspensions of modified TiO_2 samples was additionally performed. Irradiated water suspensions of TiO_2 represent complex systems where the primarily photogenerated charge carriers are further involved in series of different redox processes generating a wide range of paramagnetic intermediates, character and amount of which is significantly affected not only by the photocatalyst itself but also by the experimental conditions (solvent, molecular oxygen presence, irradiation source, *etc.*). Hydroxyl radicals formed in the water suspensions of TiO_2 upon UV irradiation are commonly declared as the one of important reactive oxygen species responsible for the nonselective photocatalytic decomposition of toxic pollutants present in water (see p. 7-8). Even though the $HO^{\cdot}$ radicals are extremely short-lived, the EPR spin trapping technique enables their detection based on the monitoring of the corresponding spin adduct. The ability of studied photocatalysts to generate $HO^{\cdot}$ radicals in the irradiated water suspensions under air was monitored using the DMPO spin trapping agent.

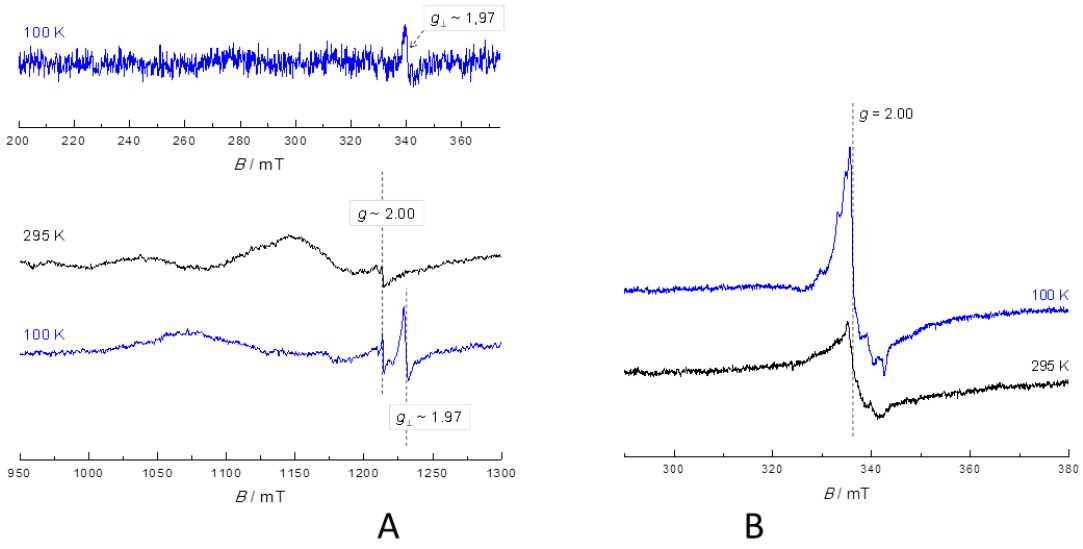

Fig. 25 (A) X-band and (B) Q-band EPR spectra of powdered Zr modified TiO_2 measured at 295 K or 100 K.

Fig. 26 displays the typical time course of EPR spectra obtained upon continuous UV (λ_{max} = 365 nm; 16 mW cm^{-2}) irradiation of the TiO_2/DMPO/H_2O/air system. The four lines EPR signal assigned to the spin adduct $^{\cdot}$DMPO-OH based on the parameters obtained from the simulation analysis (Fig. 27 B, a_N = 1.499 mT, a_H = 1.485 mT, g = 2.0057) increases immediately after the irradiation starts.

Analogous experiments were conducted with all studied samples in order to follow the effect of the surface modification with CuO and ZrO_2 on the $HO^{\cdot}$ radicals' formation. EPR spectra obtained upon/after the photoexcitation of the system TiO_2/DMPO/H_2O/air using different light sources, *i.e.* UV (λ_{max} = 365 nm; λ_{max} = 385 nm; λ_{max} = 400 nm) or VIS (160 klx) revealed the formation of $^{\cdot}$DMPO-OH spin adduct immediately after the irradiation started for all samples. However, the intensity of the signals, evaluated as the concentration of $^{\cdot}$DMPO-OH spin adduct obtained after 180 s exposure (Fig. 27) varies significantly with respect to the cation and to the irradiation source used.

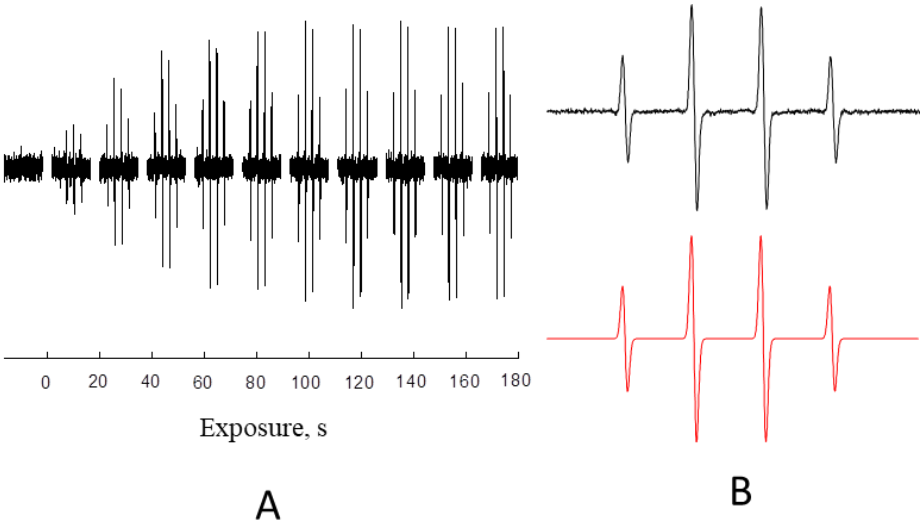

Fig. 26 (A) Time course of EPR spectra (magnetic field sweep, SW = 8 mT) monitored upon continuous UV irradiation (λ_{max} = 365 nm; 16 mW cm^{-2}) of Zr modified TiO_2water suspension in the presence of spin trapping agent DMPO under air. (B) Experimental (black) and simulated (red) EPR spectrum (SW = 8 mT) obtained upon 180 s UV irradiation. Initial concentrations: c(TiO_2) = 0.33 g L^{-1}; c_0(DMPO) = 30 mM.

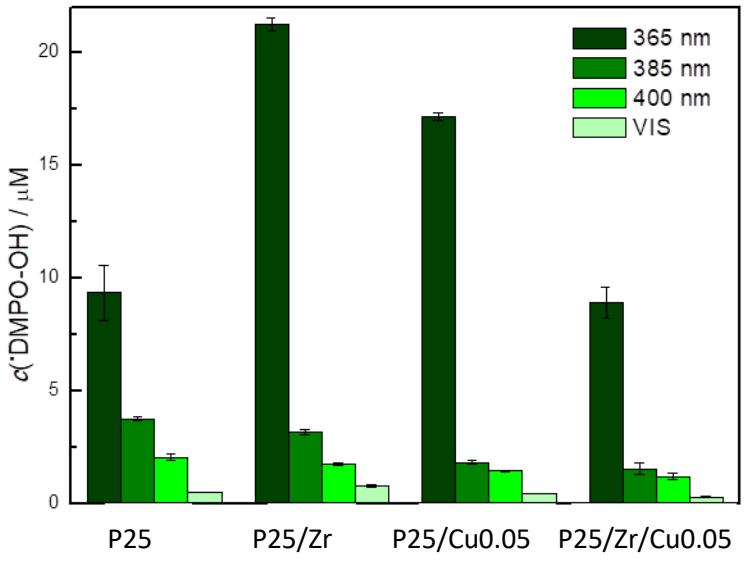

Fig. 27. Concentrations of the DMPO-OH spin adduct obtained from the EPR spectra monitored upon 180 s exposure (UV:λ_{max} = 365 nm; λ_{max} = 385 nm; λ_{max} = 400 nm; VIS;160 klx) of water suspensions of surface modified TiO_2 nanostructures in the presence of the spin trapping agent DMPO. Initial concentrations: c_0(photocatalyst) = 0.17 g /L; c_0(DMPO) = 35 mM.

Highest concentration of spin adduct was observed for Zr modified sample photoexcited with 365 nm light. Both Zr and Cu modified samples exhibit in water suspension significantly higher concentrations of $^{\cdot}$DMPO-OH spin adduct compared to benchmark P25 upon 365 nm light photoexcitation (Fig. 27). Distinct decrease in the concentration of observed spin adducts was observed upon increase of the wavelength of the irradiation applied. The modified samples do not even reach the concentrations observed by P25 photoexcitation with 385 and 400 nm. Visible light exposure of TiO_2/DMPO/H_2O/air systems lead to the formation of very low intensity EPR signals (the concentration of monitored spin adducts bellow μM).

UV irradiation of TiO_2 based photocatalysts leads to a complex reaction system, when after the primary photogeneration of charge carriers, their further reactions yield various reactive oxygen species involved in a number of consecutive processes (see the mechanism described in the Theoretical background chapter). Hydrogen peroxide may be formed in the irradiated TiO_2 water suspension (equations (4-5)). H_2O_2 undergoes several consecutive reactions (equations (6), (7)) which may represent an important source of $HO^{\cdot}$ radicals in the studied systems.

To support this statement series of experiments were conducted where the formation of $^{\cdot}$DMPO-OH upon 180 s UV (λ_{max} = 365 nm; λ_{max} = 385 nm; λ_{max} = 400 nm) or VIS exposure of water solution of H_2O_2 in the presence of DMPO was studied. The result of the experiments is presented in the Fig. 28. The presence of the spin adduct signal in the EPR spectra is strongly dependent on the type of irradiation applied revealing the highest intensity for λ_{max} = 365 nm. Even though hydrogen peroxide exhibits only limited absorption of light in the region above 300 nm recognisable signals of $^{\cdot}$DMPO-OH spin adduct were still measured for the irradiation light of 385 nm and 400 nm. When the visible light is applied only low intensity EPR spectra were monitored corresponding to the spin adduct concentration below 1 μM. This suggests that upon UV irradiation the photoinduced decomposition of hydrogen peroxide represents an important source of hydroxyl radicals. This could be one of the reasons of such high spin adduct concentration detected under the UV light. As it is clearly seen from equation (4-5) the number of H_2O_2 is proportional to the number of $O_2^{\cdot-}$ formed. This observation suggests increased concentration of oxyradical produced by Zr and Cu containing species, which was discussed for Cu modified TiO_2 earlier (Irie et al. 2009) and seems reasonable.

It is also important to notice, that formation of H_2O_2 is more pronounced for the rutile phase compared to anatase (Kakuma et al. 2015) and increased amount of H_2O_2 produced by Zr and Cu containing species on TiO_2 surface may suggest changes in surface structure of the samples.

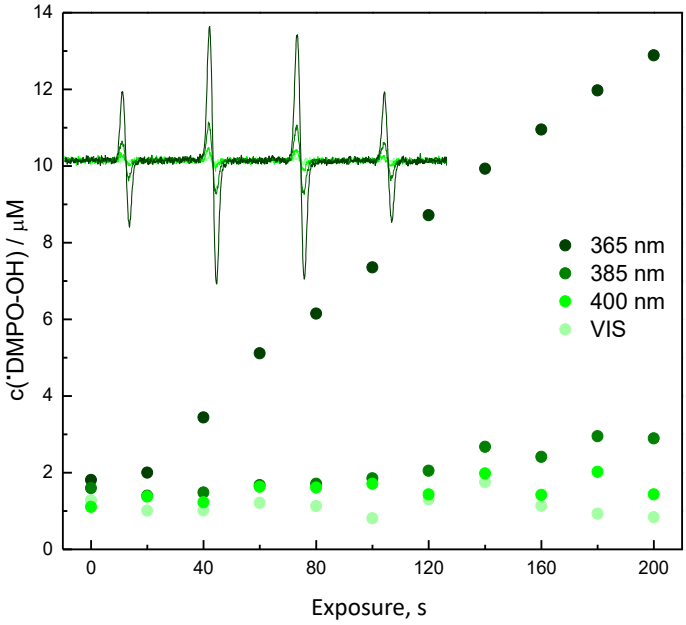

Fig. 28. EPR spectra as well as the concentrations of the ˙DMPO-OH obtained upon UV (λ_{max} = 365 nm; λ_{max} = 385 nm; λ_{max} = 400 nm; 16 mW cm^{-2}) and visible (160 klx) light exposure of H_2O_2 water solutions in the presence of spin trapping agent DMPO under the air. Initial concentrations: $c_0(H_2O_2)$ = 40 μM; c_0(DMPO) = 35 mM.

The EPR experiment results were not in agreement with the trend in activity of Cu/Zr modified photocatalysts obtained for the RB19 degradation. This may suggest the difference in mechanism responsible for the RB19 dye degradation and ˙DMPO-OH spin adduct formation in the system. Generally, DMPO-OH spin adduct may be produced by HO˙ diffused to the suspention (H_2O_2 decomposition) and on the TiO_2 surface. However, decomposition of RB19 apparently appears only on the surface of photocatalyst and is not influenced (or slightly influenced) by the HO˙ diffused to the solution. The mechanism standing behind the RB19 decomposition by simultaneous Cu/Zr modification of TiO_2 remained the open question and forced us to continue investigation and keep doing further experiments.

The in-depth investigation of surface morphology of Cu/Zr modified TiO_2 can help in answering the question about the undergoing dye degradation processes.

The materials were investigated by electron microscopy. In Fig. 29 scanning transmission electron micrographs (STEM) of Cu modified samples are shown.

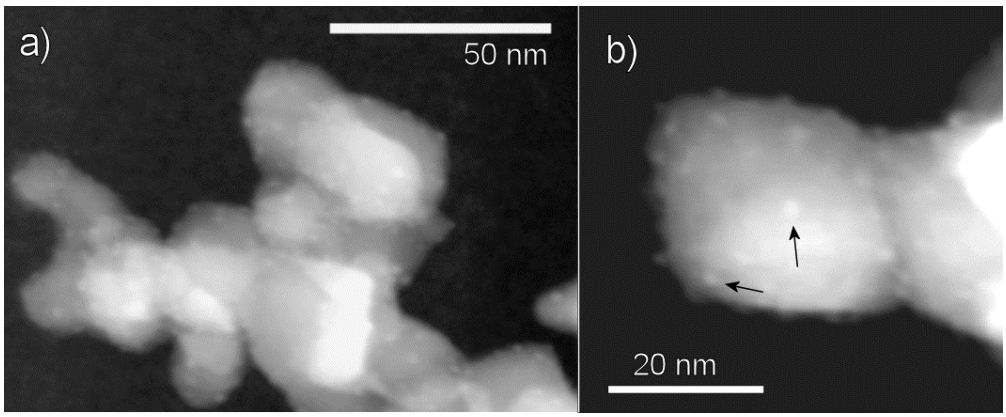

Fig. 29. Dark-field scanning transmission electron micrographs of 0.05 mol % Cu modified TiO_2 at different magnifications: a) an agglomeration of nanoparticles; b) CuO nanoclusters on the surface of a TiO_2 nanoparticle identified by arrows.

The presence of bright features of about 1-2 nm size are clearly visible on the surface of TiO_2 nanoparticles. Since in dark-field STEM the intensity in the images increases with the atomic number of the elements, the presence of features brighter than TiO_2 (and not present in the images of unmodified TiO_2) is compatible with the idea of copper-containing nanoclusters. Unfortunately, as a result of limited statistics it was not possible to clearly state the size and/or density increment of the observed CuO features at higher Cu loading. The large bright features in the centre of the Fig. 30 a) are not Cu particles, but regions where multiple nanoparticles overlap, which creates a brighter signal. The saturation is due to enhanced contrast, which is necessary to visualize the features in the rest of the picture.

The Cu K-edge XANES analysis was used to determine the Cu valence states in the Cu and Cu/Zr modified P25 photocatalysts. The valence state of the Cu cation is known to directly affect the energy position of the Cu K-edge and pre-edge features ascribed to (1s-4p) transitions. The changes in energy of the Cu K-edge and pre-edge features of about 4 eV are observed between Cu(I) and Cu(II) cations (Lytle et al. 1988), (Castagnola et al. 2005), (Alayon et al. 2015), (Irie et al. 2009).

The normalized Cu K-edge XANES spectra of the samples are shown on Fig. 30, together with XANES spectra of reference copper compounds with Cu(I)

and Cu(II) valence state and similar Cu coordination. Judging from the energy position of the Cu K-edge and pre-edge features in the XANES spectra of the catalyst samples, compared to those in XANES spectra of the Cu reference compounds, we can conclude that the oxidation state of copper cations in obtained samples is Cu(II).

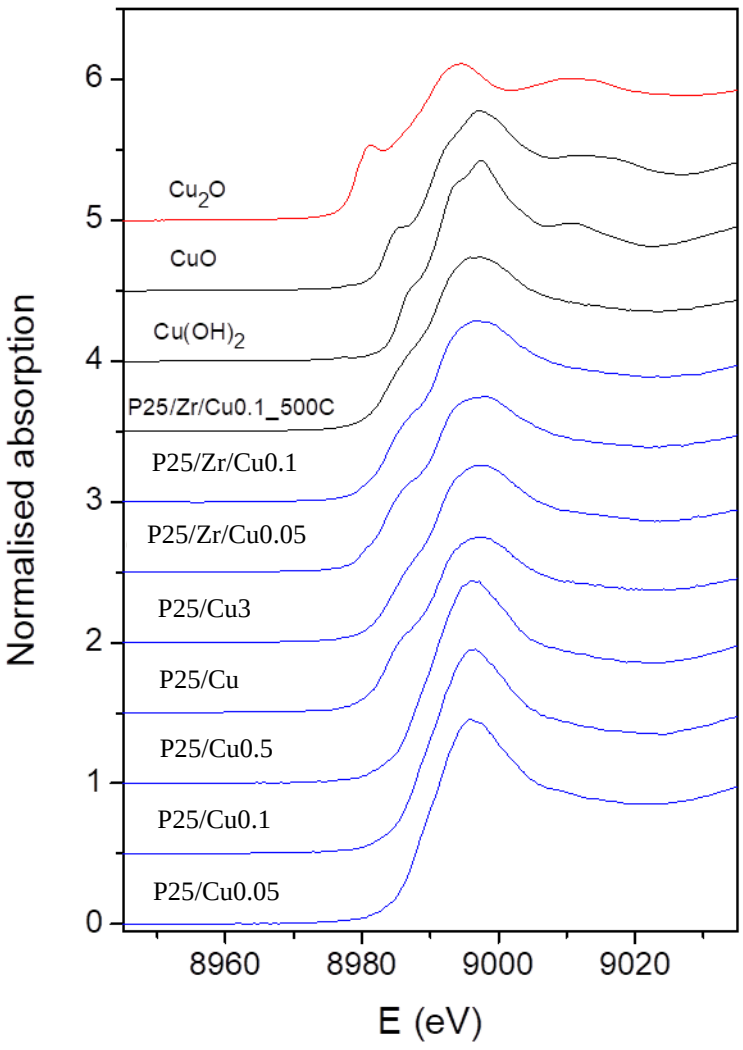

Fig. 30. Normalized Cu K-edge XANES spectraof Cu and Cu/Zr modified P25 photocatalysts. Spectra of reference Cu(I) and Cu(II) compounds (crystalline Cu_2O, CuO and $Cu(OH)_2$), and Cu/Zr modified P25 photocatalyst sample calcined at 500 °C (P25/Zr/$Cu_{0.1}$_500 °C) from Fig.17 are plotted for comparison.

A Cu and Zr K-edge EXAFS analysis is used to determine average local structure around Cu and Zr cations in the Cu, Zr and Cu/Zr modified P25 photocatalysts. In Fourier transform magnitude of the Cu (Fig. 31) and Zr K-edge

EXAFS spectra of the samples (Fig. 32) the contributions of photoelectron backscattering on the nearest shells of neighbor atoms around the Cu or Zr atoms are observed as peaks in the R range from 1 to 3.6 Å.

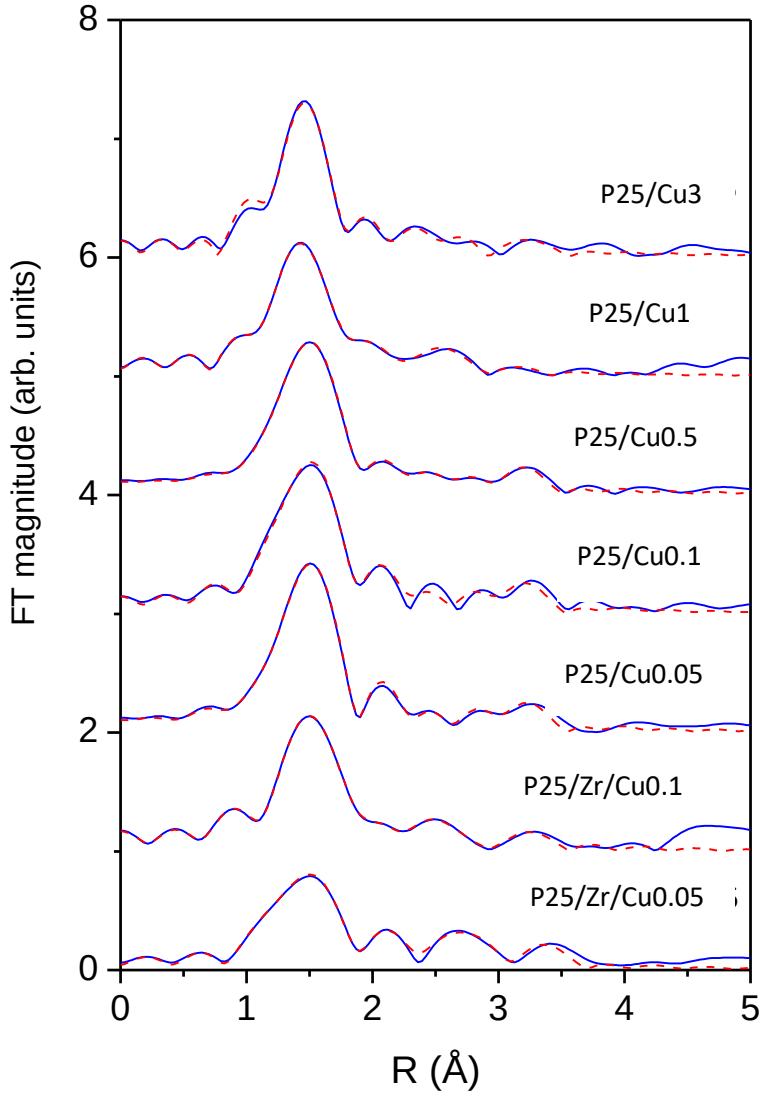

Fig. 31. Fourier transform magnitude of k^2-weighted Cu K-edge EXAFS spectra of Cu and Cu/Zr modified P25 photocatalysts, calculated in the k range of 2.5 $Å^{-1}$ – 11.0 $Å^{-1}$ and in the R range of 1.0 Å – 3.6 Å. Experiment: solid line; best-fit EXAFS model: dashed line.

A good agreement between the model (detailed description of the model can be found in experimental material) and the experimental spectra is found for all spectra, using the k range of 2.5 $Å^{-1}$ – 11.0 $Å^{-1}$ and in the R range of 1.0 Å – 3.6 Å for Cu EXAFS spectra (Fig. 31), and k and R ranges of 3.0 $Å^{-1}$ –13.5 $Å^{-1}$ and 1.0 Å –

3.7 Å, respectively, for Zr EXAFS spectra (Fig. 32). The list of the best fit parameters is given in the Tables 5-7.

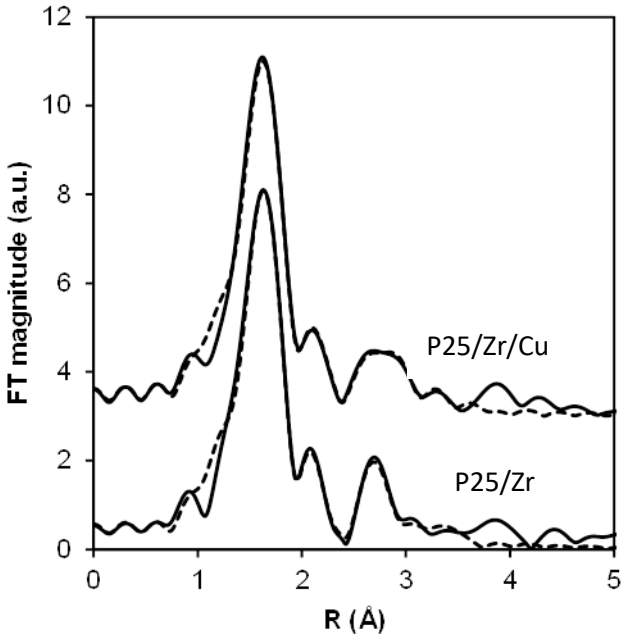

Fig. 32. Fourier transform magnitude of k^3-weighted Zr K-edge EXAFS spectra of Zr and Cu/Zr modified P25 photocatalysts, calculated in k and R ranges of 3.0 $Å^{-1}$ –13.5 $Å^{-1}$ and 1.0 Å – 3.7 Å, respectively. Experiment: solid line; best-fit EXAFS model: dashed line.

Similar average Cu local neighborhoods are found in all photocatalyst samples. Cu cations are octahedrally coordinated to six oxygen atoms, in a distorted octahedron with four oxygen atoms in the equatorial plane at shorter Cu–O distance (1.95 Å –1.98 Å) and two oxygen atoms on axial positions at longer distance (2.18 Å –2.28 Å). In the more distant coordination shells Ti and Cu neighbors are detected, while Zr neighbors are ruled out by the fit. The results show that part of Cu cations is bound to the TiO_2 surface forming Cu-O-Ti connections and part of Cu cations are forming Cu-O-Cu connections.

The average Cu neighborhood is mostly independent of Cu loading in monometallic or in bimetallic Cu/Zr modified photocatalysts, except at larger Cu loadings (1 % and 3 %), where average numbers of Cu and Ti neighbors are found to be slightly lower, compared to those in photocatalysts with lower Cu loadings. The result suggests that CuO nanoparticles are formed on TiO_2 surface.

In the bimetallic Cu/Zr modified P25 photocatalysts, there are no Cu-O-Zr bonds, which indicates that separate ZrO_2 and CuO species are formed on TiO_2 surface.

Table 5. Parameters of the nearest coordination shells around Cu cations in the Cu modified P25 photocatalysts at 0.05%, 0.1% and 0.5% Cu loading: average number of neighbor atoms (*N*), distance (*R*), and Debye-Waller factor (σ^2). Uncertainty of the last digit is given in parentheses. A best fit is obtained with the amplitude reduction factor $S_0^2 = 0.85$. The shift of the energy origin ΔE_o and *R*-factor (quality of fit parameter) are listed in the last column.

Cu neigh.	*N*	*R* [Å]	σ^2 [Å^2]	ΔE_o/ *R*-factor
P25/$Cu_{0.05}$				
O	4.7(4)	1.98(2)	0.004(1)	2 ± 1 eV 0.003
O	1.3(4)	2.26(2)	0.004(1)	
Ti	1.1(4)	3.30(4)	0.012(3)	
Cu	1.9(6)	3.48(3)	0.012(3)	
P25/$Cu_{0.1}$				
O	4.7(4)	1.97(1)	0.006(2)	2 ± 1 eV 0.012
O	1.3(4)	2.22(4)	0.006(2)	
Ti	1.0(6)	3.30(6)	0.012(3)	
Cu	2.0(9)	3.48(5)	0.012(3)	
P25/$Cu_{0.5}$				
O	5.0(2)	1.98(1)	0.007(1)	1 ± 1 eV 0.003
O	1.0(2)	2.27(3)	0.007(1)	
Ti	0.9(6)	3.23(4)	0.012(3)	
Cu	1.9(9)	3.44(4)	0.012(3)	

The result is supported also by Zr EXAFS analysis (Table 8), which shows that Zr cations in bimetal Cu/Zr modified P25 photocatalyst are dispersed on the surface of TiO_2 as ZrO_2 nanoparticles bonded to TiO_2 surface. Average Zr local neighborhood in bimetallic Cu/Zr modified P25 is very similar to that in the monometallic Zr modified P25 photocatalyst. In both cases we found Zr-O-Zr and Zr-O-Ti bonds, but no Zr-O-Cu connections.

Table 6**.** Parameters of the nearest coordination shells around Cu cations in the Cu modified P25 photocatalysts at 1% and 3% Cu loading: average number of neighbor atoms (*N*), distance (*R*), and Debye-Waller factor (σ^2). Uncertainty of the last digit is given in parentheses. A best fit is obtained with the amplitude reduction factor $S_0^2 = 0.85$. The shift of the energy origin ΔE_o and *R*-factor (quality of fit parameter) are listed in the last column.

Cu neigh.	*N*	*R* [Å]	σ^2 [Å^2]	ΔE_o/ *R*-factor
P25/Cu$_1$				
O	4.4(3)	1.95(1)	0.007(1)	0 ± 2 eV 0.002
O	1.6(3)	2.19(3)	0.007(1)	
O	0.7(3)	2.55(3)	0.008(1)	
Ti	0.9(4)	3.10(4)	0.012(3)	
Cu	0.7(4)	3.40(4)	0.012(3)	
P25/Cu$_3$				
O	4.0(3)	1.96(1)	0.003(1)	1 ± 2 eV 0.010
O	2.0(3)	2.18(3)	0.003(1)	
O	1.0(3)	2.45(5)	0.008(1)	
Ti	0.4(2)	3.16(9)	0.012(3)	
Cu	1.1(6)	3.51(6)	0.012(3)	

Table 7**.** Parameters of the nearest coordination shells around Cu cations in the Cu/Zr modified P25 photocatalysts: average number of neighbor atoms (*N*), distance (*R*), and Debye-Waller factor (σ^2). Uncertainty of the last digit is given in parentheses. A best fit is obtained with the amplitude reduction factor $S_0^2 = 0.90$. The shift of the energy origin ΔE_o and *R*-factor (quality of fit parameter) are listed in the last column.

Cu neigh.	*N*	*R* [Å]	σ^2 [Å^2]	ΔE_o/ *R*-factor
P25/Zr/$Cu_{0.05}$				
O	4.1(5)	1.98(3)	0.009(1)	4 ± 3 eV 0.008
O	1.9(5)	2.27(5)	0.009(1)	
Ti	1.5(5)	3.23(7)	0.012(3)	
Cu	2(1)	3.58(6)	0.012(3)	
P25/Zr/$Cu_{0.1}$				
O	5.2(5)	1.96(2)	0.012(5)	-3 ± 3 eV 0.019
O	0.8(5)	2.24(4)	0.012(5)	
Ti	1.1(5)	3.13(8)	0.012(5)	
Cu	1.5(7)	3.41(8)	0.012(5)	

Table 8. Parameters of the nearest coordination shells around Zr cations in the Zr and Cu/Zr modified P25 photocatalysts: average number of neighbor atoms (*N*), distance (*R*), and Debye-Waller factor (σ^2). Uncertainty of the last digit is given in parentheses. A best fit is obtained with the amplitude reduction factor $S_0^2 = 0.90$. The shift of the energy origin ΔE_o and *R*-factor (quality of fit parameter) are listed in the last column.

Zr neigh.	*N*	*R* [Å]	σ^2 [Å^2]	ΔE_o/ *R*-factor
P25/Zr				
O	4(1)	2.09(2)	0.002(1)	4 ± 2 eV 0.016
O	1.8(5)	2.23(4)	0.002(1)	
O	1.7(9)	2.75(3)	0.005(3)	
O	0.8(5)	3.11(9)	0.005(3)	
Ti	1.1(6)	3.22(9)	0.009(4)	
Zr	0.5(3)	3.49(6)	0.010(4)	
P25/Zr/$Cu_{0.1}$				
O	3.3(3)	2.08(2)	0.002(1)	4 ± 2 eV 0.010
O	1.8(3)	2.28(3)	0.002(1)	
O	1.2(8)	2.72(2)	0.003(2)	
Ti	1.7(5)	3.25(2)	0.009(4)	
Zr	2(1)	3.68(5)	0.016(4)	

The results obtained from the X-ray absorption spectroscopy and the assumption that the type of TiO_2 crystal phase, on which CuO clusters are formed, plays a role in the activity of CuO modified TiO_2 (Jin et al. 2013) led us to the hypothesis about spatial separation of CuO and ZrO_2 surface sites in the mixed phase TiO_2. The STEM-EDX mapping of Cu/Zr modified P25 was performed using Ni TEM grid (Fig. 33). We can clearly see the homogeneous distribution of Cu and Zr on the surface of TiO_2. However, to answer the question about uniform or spatially separated distribution of Cu and Zr containing species we would need to acquire spectrum on the single nanoparticle. With the resolution and sensitivity of our microscope it is not possible to address the Zr and Cu distribution on the single particle which in this case, due to very low Cu and Zr loading, became lower than detection limit (0.1 mol%). The other problem is the fast sample deterioration under the beam irradiation: the particle is burned before the entire spectrum is acquired.

According to the results obtained from the X-ray absorption spectroscopy and further assessed by STEM-EDX mapping (Fig. 33) it can be summarized that Zr and Cu containing species do not form mixed clusters and are homogeneously distributed on the TiO_2 surface.

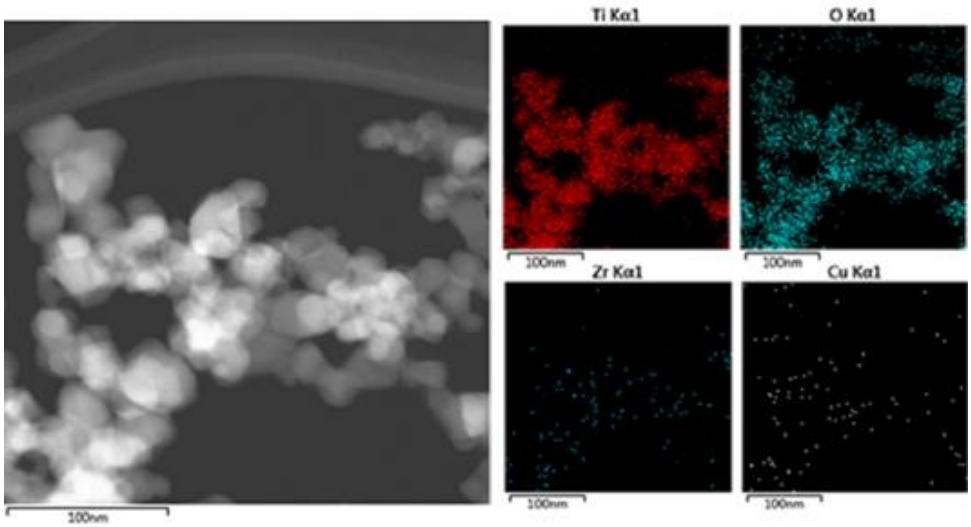

Fig. 33. STEM-EDX mapping results for P25/Zr/$Cu_{0.1}$ sample.

In order to check the hypothesis of spatial separation of CuO and ZrO_2 on the surface of P25 titration with Hammett indicators of Cu and Zr modified TiO_2 was applied. Surface sites on the metal oxides are usually associated with the acidity of the surface. The methyl red (MR) color changes can be caused only by rutile surface

sites with pK_1 = 3.9. The changes of bromothymol blue (BB) color can be caused by presence of two surface sites: rutile pK_1 = 3.9 and anatase pK_1 = 4.6. At the same time, the changes of neutral red (NR) color can be provoked by the presence of three surface sites: rutile pK_1 = 3.9, anatase pK_1 = 4.6 and rutile pK_2 = 6.8. Following the number of the surface sites determined by titration, we have clearly seen the gradual reduction in number of rutile and anatase acidic sites with modification (Fig. 34). The fraction of anatase and rutile surface sites covered by a modifier was calculated; the results are presented in Table 9.

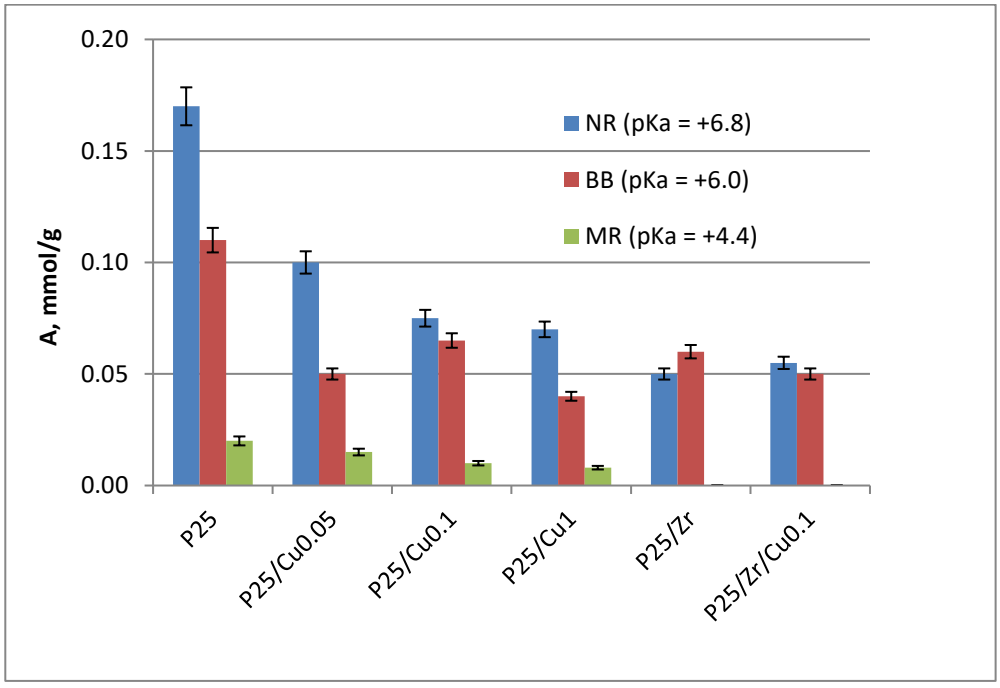

Fig. 34. Surface acidity of Cu/Zr modified TiO_2. The abbreviations in the figure are: NR - neutral red, BB - bromothymol blue, MR - methyl red.

The sample with only Cu-loading showed gradual coverage of both anatase and rutile acidic sites even at high 1 mol % of Cu loading. Meanwhile, the sample with 1 mol % Zr nominal loading exhibits sites with a lower total acid strength ($H_0 \leq$ +6.0) and shows total vanishing of rutile sites and much lower coverage of anatase surface sites. Taking into account that Zr loading is an order of magnitude in excess compared to the Cu nominal loading in the mixed Cu/Zr sample, it becomes evident that Zr occupies the rutile surface sites and this way prevents the formation of Cu-rutile connections (Fig. 35). As a consequence, the occupation of rutile surface sites postpones the appearance of reverse charge localization mechanism to higher Cu

loading and facilitates the photocatalytic activity of Cu/Zr modified P25 at 0.1 mol % Cu loading compared to Cu only modified sample.

Table 9. The fraction (F) of anatase and rutile surface sites covered by a modifier.

Sample	F±5, %		
	pK_1^{Rutile}	$pK_1^{Anatase}$	pK_2^{Rutile}
P25	0	0	0
$P25/Cu_{0.05}$	29	56	24
$P25/Cu_{0.1}$	80	36	73
$P25/Cu_1$	88	58	48
P25/Zr	100	24	100
$P25/Zr/Cu_{0.05}$	100	42	100

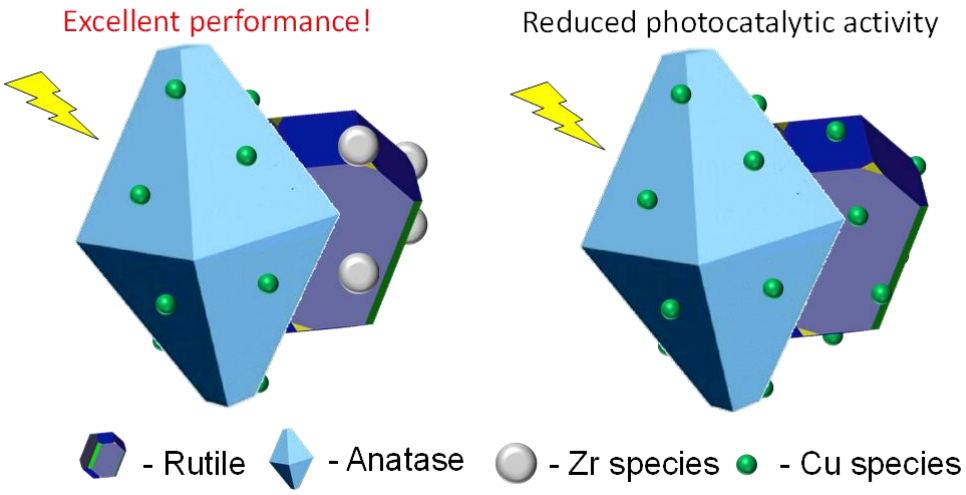

Fig. 35. Schematic presentation of beneficial Zr contribution to Zr/Cu modified mixed phase TiO_2 performance.

Interestingly, despite blocking the rutile surface sites, Zr does not influence the photocatalytic activity of P25 toward RB19. There is, therefore, a possibility that the degradation of RB19 proceeds mainly on the anatase surface of P25. However, the presence of rutile phase cannot be ignored since it has a beneficial role in the charge separation properties of the material.

Conclusions

Copper/zirconium surface modified photocatalysts were prepared by modification of commercial titanium dioxide Aeroxide®Degussa P25 with copper acetyl-acetonate and zirconium butoxide as sources of copper and zirconium ions. Hardness testing of the active layers formed from modified TiO_2 showed that Zr loading leads to an improvement in the scratch resistance of the film compared to Cu only modified samples.

XRD revealed only peaks responsible for anatase and rutile phases from P25, which can be attributed to low amount and fine dispersion of copper and zirconium species on the TiO_2 surface.

Applying DRS an additional absorption shoulder at ~450 nm was registered, which is attributed to the presence of CuO nanoclusters on the surface of TiO_2. In the samples modified with Zr this effect does not occur, but it persists at combined Cu/Zr modified samples. An additional broad band appears at about 700 nm and it can be attributed to the d-d transition of Cu in an (pseudo-) octahedral environment in CuO. The optical band gaps of Cu and Zr modified TiO_2 catalysts were determined. The band gap values estimated from the Kubelka-Munk curves differ not more than 3 %, which cannot significantly influence the visible light activity of materials.

Isoelectric point determination confirmed that Cu loading shifts IEP towards higher pH values however combined Cu/Zr modification results in IEP close to unmodified or Zr only modified TiO_2.

The activity test of prepared materials towards RB19 exhibited results similar to that discussed in chapter 3.1. There is a limit of copper loading for beneficial performance of TiO_2 towards dye degradation. Zr beneficially influences the rate of RB19 degradation at Cu/Zr modified TiO_2 compared to Cu only modified TiO_2.

The test performed with Fenton reagent and H_2O_2 as a source of $HO^{\cdot}$ radicals suggests that the lowering in photocatalytic efficiency of Cu modified TiO_2 is not connected to the capturing of $HO^{\cdot}$ radicals by the copper containing species formed on the surface of P25.

According to the EPR measurements both Zr and Cu modified samples in water suspension exhibit significantly higher concentrations of $^{\cdot}$DMPO-OH spin adduct compared to benchmark P25 photoexcited with UV light. This result was associated with the contribution of hydrogen peroxide to the formation of the

·DMPO-OH spin adduct. Increased formation of H_2O_2 can be connected to the increased number of oxyradicals formed by Cu/Zr modified samples. However, this statement needs additional proof. It was assumed, that RB19 dye degradation is not influenced by the $HO^{\cdot}$ formed from H_2O_2 and diffused to the suspension.

Microscopic investigation of the copper modified powders reveal the formation of copper oxide nanoclusters 1-2 nm in size, while EXAFS and STEM-EDX analyses confirm the formation of separate ZrO_2 and CuO species and their homogeneous distribution on the surface of the TiO_2, respectively.

Regarding the surface acidic sites, titration with Hammett indicators revealed that Zr modification results in the total coverage of the rutile surface sites. This together with photocatalytic activity test results strongly supports the statement that at high copper loading the formation of copper–rutile connections are harmful.

In the case of combined Cu/Zr modification, Zr acts as a shield, covering the rutile surface, which results in copper–anatase interaction. Thereby, zirconium modification beneficially influences the photocatalytic activity of copper modified mixed phase TiO_2 at high copper loading.

3.3. EVALUATION OF THE THIRD HYPOTHESIS.

Hypothesis 3. ***RB19 dye at low concentration degrades essentially by means of photocatalytic reaction.***

TLS FOR DETERMINATION OF RB19 DEGRADATION UNDER THE SIMULATED SOLAR LIGHT

The aim of this part of the research work is to distinguish between photocatalytic and photosensitization mechanisms of RB19 dye degradation and to determine the governing mechanism responsible for dye degradation at low dye and photocatalyst concentrations under the simulated solar light. The term «governing» does not mean that there is no influence of the second mechanism to overall degradation process, but it means that the contribution of the governing mechanism is higher compared to the second one. Additionally, we are going to demonstrate the capability of photothermal technique such as TLS to follow the RB19 dye degradation kinetics at low (5 mg/L) concentration.

All examined samples are in the shape of fine dispersed powders. They are the same photocatalysts described and characterized in the previous chapter. The light irradiation used for carrying out the experiments with solutions with 50 mg/L of RB19 (high dye concentration) was Xenon lamp with day light filter (Suntest XLS+, Atlas, USA) with UV fraction λ_{max} = 300 - 400 nm, 6.1 mW/cm^2 and UV lamp (home made photocatalytic chamber) with λ_{max} = 365 nm, 2.3 mW/cm^2. The light irradiation used for carrying out the experiments with solutions with 5 mg/L of RB19 (low dye concentration) was 300 W UV lamp (Osram Ultra Vitalux 300W E27) with radiated power of 13.6 W in near UV (315-400 nm) and 3.0 W at shorter wavelengths (280 – 315 nm), the remaining 284 W in Vis (400-800 nm) wavelength region. As it is discussed in the first chapter, solar light irradiation includes Vis light and may cause difficulties in understanding and description of processes that undergo during dye degradation assisted with TiO_2.

The photocatalytic test of materials with RB19 dye as model pollutant was performed and described in Chapter 3.2. It must be taken into account that sensitization mechanism of dye degradation is possible to occur under the solar light irradiation and may significantly influence the overall test results. To consider the mechanisms responsible for RB19 dye degradation assisted with TiO_2 at high and

low dye concentrations under the different light sources further experiments were performed.

The changes of RB19 spectrum caused by P25 and simulated solar or UV light are presented in Fig. 36. For clarity, obtained spectra were normalized according to their maximal absorption at 590 nm.

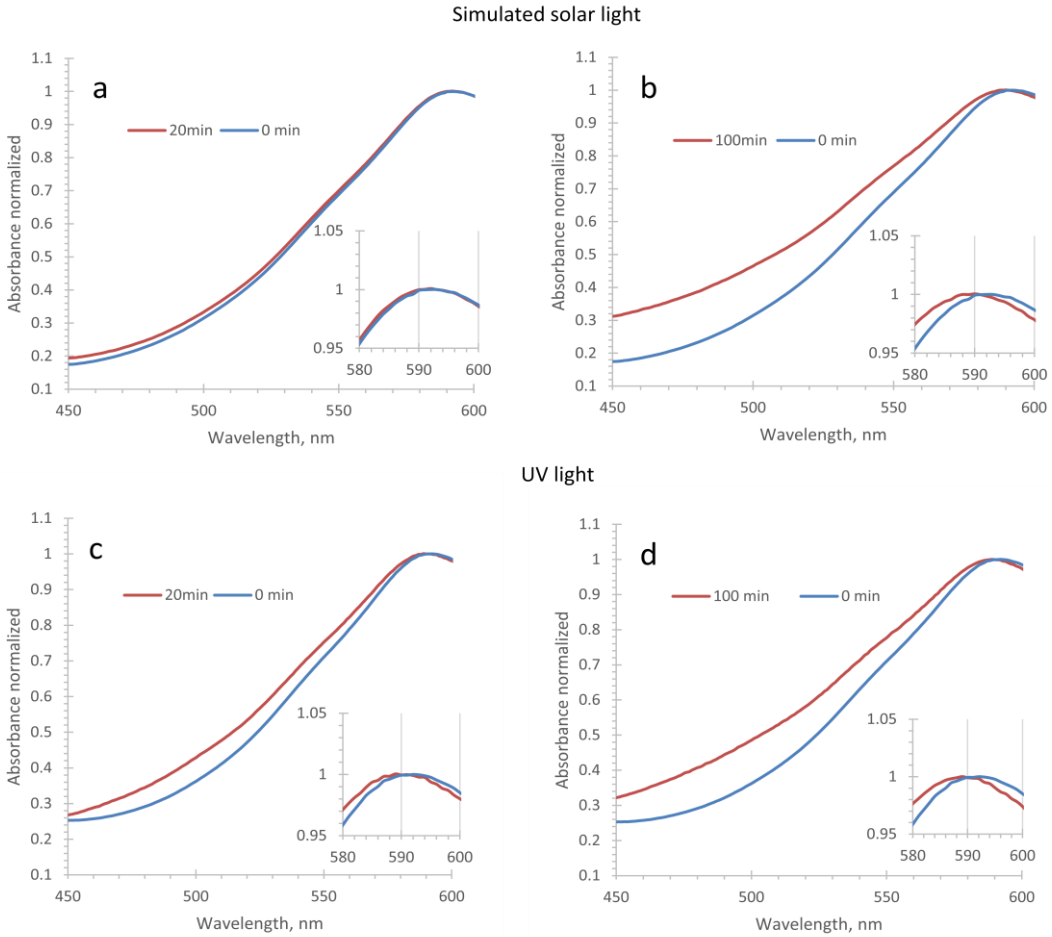

Fig.36. The absorption spectrum of RB19 after the simulated solar and UV lights irradiation in presence of TiO_2 (P25) for 0 min (blue), 20 or 100 min (red). For clarity all curves were normalized to the intensity of absorption peak at 590 nm.

Bleaching of the dye is characteristic feature that occurred under the both light sources. In parallel to lowering the absorbance at 590 nm, a dramatic broadening of the absorption band occurs after 100 min of irradiation (Fig. 36 b, d) under the both UV and solar simulated lights. The broadening is caused by the intermediates formed during the reaction (Rochkind et al. 2015). The spectra of intermediates can interfere with the spectrum of the dye causing the observed

broadening of absorption band. It is evident, that the absorption peak undergoes slight shift towards the lower wavelength, so-called hypocromic shift. This shift is a consequence of C-N bond cleavage. Break away of amino group, as typical auxochrom from benzene ring, may lead to a decline in intensity of the peak together with an obvious blue shift (Zhang et al. 2001).

The difference in two spectra can be observed at the first 20 min of irradiation (Fig. 36 a, c). For the initial stage (20 min) of RB19 dye degradation under the simulated solar light the shift is not observed (Fig. 36 a), however it is clearly detectable for the spectra recorded after 20 min of UV light irradiation (Fig. 36 c). Such observation can be explained by the action of two different mechanisms responsible for RB19 degradation: photocatalytic under the UV light and both, photosensitization and photocatalysis under the simulated solar light. This statement is in good agreement with different RB19 degradation pathways offered by (Bilal et al. 2018) and (Abu Bakar et al. 2015) observed under the simulated solar and UV lights, respectively. Obviously, the photocatalytic reaction contribution to overall dye degradation under the simulated solar light at 50 mg/L concentration cannot be ignored.

Typical behavior presented in Fig. 36 was observed for all the systems (RB19 with Cu/Zr modified photocatalyst) tested in this work except the system with P25/Cu0.5 involved. The changes of RB19 spectra assisted with P25/Cu0.5 is presented in the Fig. 37. There is no shift of absorption maximum registered neither after 20 nor after 120 min of solar light irradiation even though the bleaching of the solution and widening of the spectra were in progress. In Chapter 3.2 it is discussed that photocatalytic mechanism of the P25/Cu0.5 powder is suppressed due to reverse localization of electrons and holes at this copper concentration. This result suggests that RB19 degradation assisted with P25/Cu0.5 powder occurs by means of photosensitization mechanism. Moreover, it supports the statement, that observed shift of RB19 absorption maximum is obvious attribute of photocatalytic mechanism and can be probably used for distinguishing between two competing mechanisms at initial stage of dye degradation.

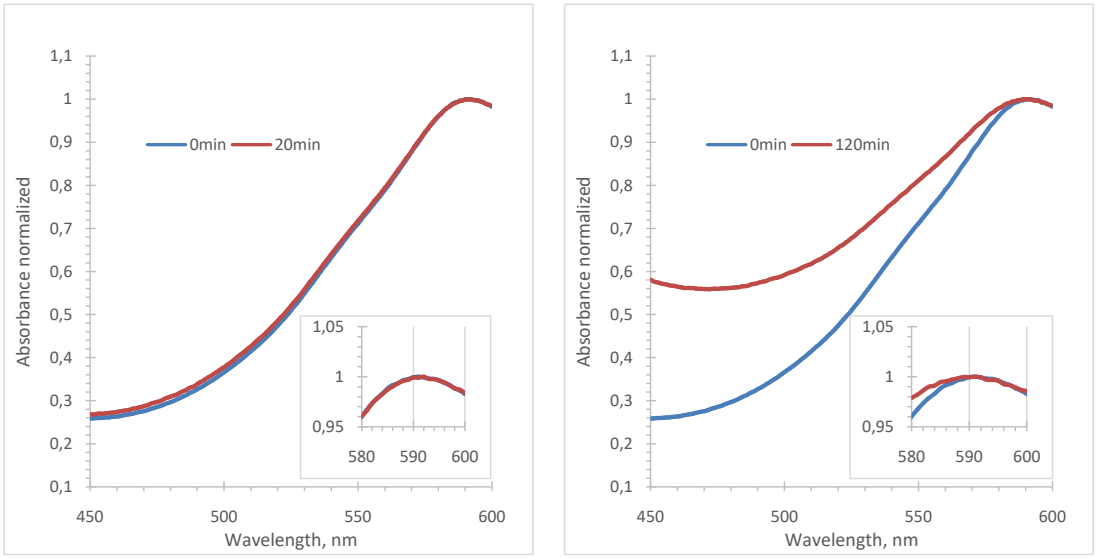

Fig. 37. The absorption spectrum of RB19 after the simulated solar irradiation in presence of P25/Cu0.5 for 0 min (blue), 20 or 120 min (red). For clarity all curves were normalized to the intensity of absorption peak at 590 nm.

It is important to add that the changes in the spectra (both, widening and shifting) are not connected to the concentration of the dye by itself (Fig. 38). With dilution of the dye, the shape of the spectra remains the same without widening or shifting of the absorption peak (Fig. 38).

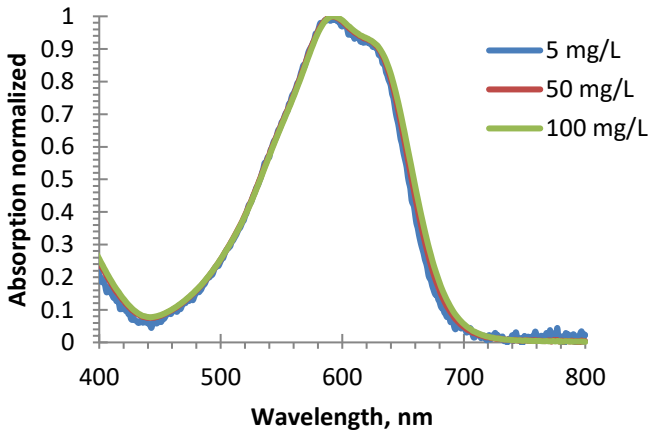

Fig. 38. Normalized optical absorption spectra of diluted RB19 dye measured by UV-Vis spectrometry in 1 cm cell.

The results obtained for 50 mg/L dye degradation assisted with TiO_2 photocatalysts under the UV and simulated solar lights and measured at 532 nm by UV-Vis spectrometry are presented in Fig. 39. The shift of absorption maximum,

which was attributed to the photocatalytic mechanism is clearly observed at the very beginning of UV light irradiation process and manifests itself as dramatic magnification of the analytical signal.

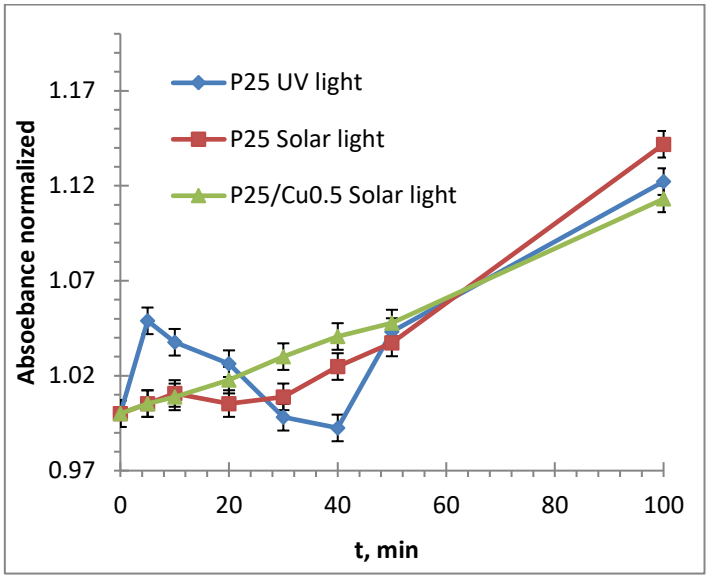

Fig. 39. RB19 (50 mg/L) degradation kinetics in presence of P25 or P25/Cu0.5 measured by UV Vis spectroscopy at 532 nm under the simulated solar and UV lights. The data is normalized to the absorbance registered at 0 min irradiation time.

Following the amplified analytical signal, decrease of the signal is registered for a short period of time. After approximately 50 min of irradiation next increase of the analytical signal is observed. Current magnification of the signal is attributed to the broadening of the absorption band due to intermediate products of dye degradation. It is difficult to say if amplification of the signal at first 10 min of simulated solar light irradiation is present or not. The changes of the signal are very small and lying within the error range of the measurements. However, it is possible that slight absorption band shift occurs under the solar light irradiation due to the contribution of photocatalytic process to overall RB19 degradation. Contrary, if one pays attention to the trend line observed for RB19 degradation under the simulated solar light irradiation with presence of P25/Cu0.5, one can note that constant analytical signal magnification is observed, which is in good agreement with results presented in Fig. 37. No shift, but constant widening of the absorption band is registered.

In order to validate the UV Vis method for determination of low concentration of RB19 the calibration curve was determined in the range of concentrations from 0.5 up to 10 mg/L. The calibration curve shows linear behavior with a correlation coefficient R^2 = 0,999 and 0,995 determined at 590 and 532 nm, respectively. The UV Vis method for determination of RB19 concentration was further validated based on the linearity range and the limits of detection (LOD) and quantification (LOQ), which were calculated as LOD = $3\times SD_{xy}/m$ and LOQ = $10\times SD_{xy}/m$ (where SD_{xy} is the standard deviation of the blank signal, and *m* is the slope of the calibration curve). The obtained values of LOD and LOQ are 200 and 700 μg/L, respectively.

Hovewer, more often validation of analytical method accuracy than validation of direct analysis is required. Before the absorption values measurements it is necessary to leave the sample for adsorption, then to centrifuge and filter the sample in order to separate particles. Additional steps in an analysis add additional opportunities for error. Since detection limits are defined in terms of error, this will naturally increase the measured detection limit. This detection limit (with all steps of the analysis included) is called the MDL (method detection limit). MDL was determined by repeatedly measuring samples of concentration near the expected limit of detection (0.5 mg/L). The standard deviation is then determined. The obtained values of LOD and LOQ are 300 and 1000 μg/L, respectively.

In order to lower the MDL, contraction of additional steps in analytical method can be used. We desided to omit the centrifugation and filtration steps and to performe the experiment in presence of photocatalyst. We performed the measurements of absorption at 532 nm with the presence of 0.06 mg/L TiO_2 and compared them with the same measurements without TiO_2. The relation of normalized absorbance of RB19 solution with presence of 0.06 mg/L and without presence of TiO_2 are shown in Fig. 40 and reveald huge impact of light scattering due to the presense of TiO_2 particles with dye concentration lowering.

From these experiments we can see, that conventional UV-Vis spectrophotometric technique is not able to provide accuracy at low (5 mg/L and lower) dye concentrations. These results clearly demonstrate that highly sensitive optical method is required to follow the kinetics of RB19 degradation at low concentrations (5 mg/L). The requirement of accurate low absorbance measurements

is satisfied by technique based on photothermal effect such as thermal lens spectrometry (TLS).

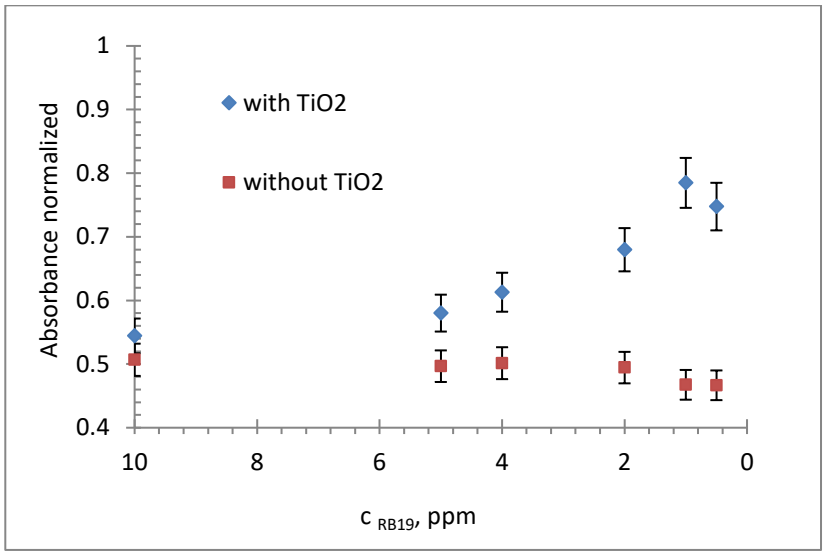

Fig. 40. Absorbance (532 nm) of RB19 solution with presence of 0.06 mg/L of TiO_2 and without TiO_2. For clarity all points were normalized to the intensity of absorption peak at 590 nm.

TLS method is known as the one developed to characterize samples with low absorption and its accuracy is not influenced by scattering. To demonstrate the applicability of the TLS method for determining low concentrations of RB19 dye at different stages of the degradation process in real time, the calibration curve was used (Fig. 41). The units of TLS signal were converted to units of concentration. The relative standard deviations (RSDs) of the TLS for standard solutions used for the calibration curve are presented in the inset of Fig. 41. The RSDs are in the range between 1.5 % and 5.4 %.

The TLS shows a linear behavior in the range of concentrations from 0.05 up to 8 mg/L, with a correlation coefficient R^2 = 0.998. At higher concentrations nonlinearity is observed due to the saturation of the signal. The TLS method for determination of RB19 concentration was further validated based on the linearity range and the limits of detection (LOD) and quantification (LOQ), which were calculated as LOD = $3\times SD_{xy}/m$ and LOQ = $10\times SD_{xy}/m$ (where SD_{xy} is the standard deviation of the blank signal, and *m* is the slope of the calibration curve). The obtained values of LOD and LOQ are 110 and 366 µg/L, respectively. Therefore, if

the sample is pumped at 590 nm, e.g., for which the absorption maximum is as twice as for 532 nm, the LOD would be around 2 times lower, what would be 53 μg/L.

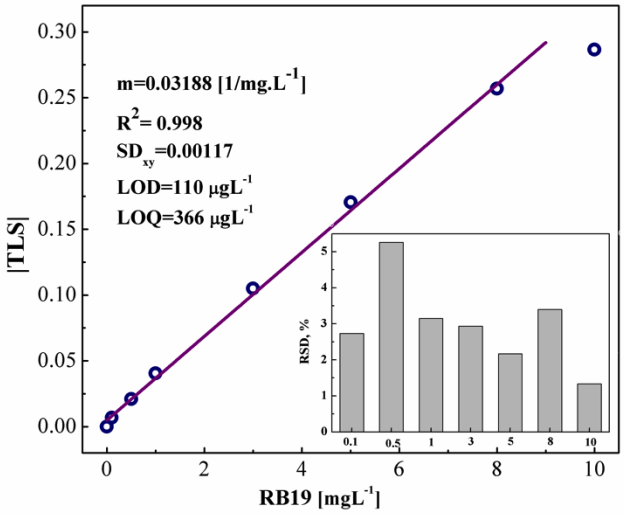

Fig. 41. Calibration curve for RB19. The inset shows the relative standard deviations (RSDs) of the data.

It is clear that TLS method is highly sensitive and enables following the degradation kinetics of RB19 at low concentration. It is not possible to observe the full spectrum of the compound by TLS measurements. The method is limited to one point wavelength measurements, controlled by pump beam wavelength. The pump beam wavelength, 532 nm, used in this study is not exactly matching the maximum absorption peak of the RB19 as it is shown in Fig. 9.

In order to evaluate the effect of the irradiation time on the photocatalyst/RB19 suspension, TL signal behavior was studied under two conditions: with and without light illumination. The light source was simulated solar light irradiation with a 300 W UV lamp (Osram Ultra Vitalux 300W E27) with radiated power of 13.6 W in near UV (315 - 400 nm) and 3.0 W at shorter wavelengths (280 - 315 nm), the remaining 284 W at Vis (400-800 nm) wavelengths. The results are shown in Fig. 42.

The TL signal changes during the irradiation period for P25 suspended in 5 mg/L of RB19. In the dark, the TL signal is constant during entire irradiation time. As the value of TL signal is proportional to the absorbance at 532 nm, the signal decrease is attributed to the dye degradation process in the presence of photocatalyst

and light simultaneously. These results reveal that the power of excitation (25 mW) and probe (3 mW) beams, as well as simulated solar light irradiation by its own have no effect on the dye degradation.

It is clearly seen, that TL signal increases at the very first period after the irradiation process started (Fig.42). The increase of the TL signal was attributed to the shift of the absorption peak. Of course, it is not possible to exclude the influence of photosensitization to overall process efficiency at 5 mg/L RB19 solution. However, the observation supports our hypothesis and demonstrates the clear presence and dominance of photocatalytic mechanism at low RB19 dye concentration.

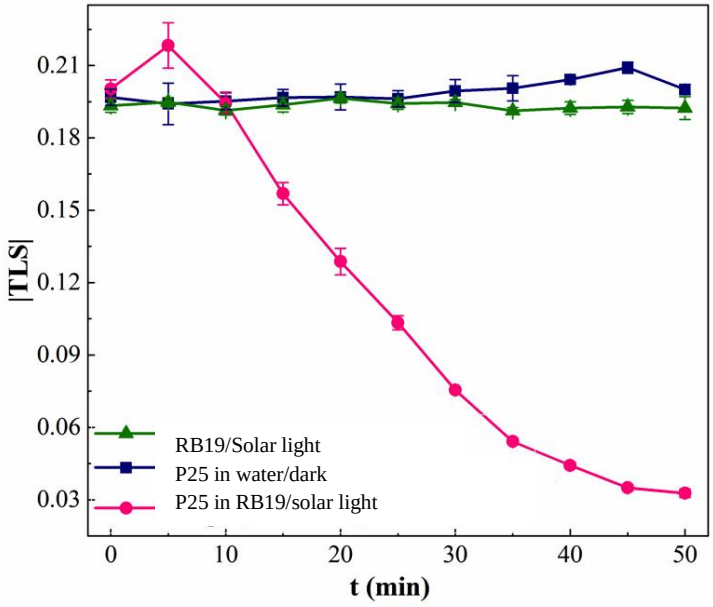

Fig.42. Temporal behavior of the TL signal for 0.06 mg/L P25 suspended in 5 mg/L RB19 under the simulated solar light irradiation.

The degradation of RB19 (5 mg/L) with Cu/Zr modified P25 was studied and obtained results are shown in Fig. 43 (a-d). The values of the TL signal in all graphs were normalized to the initial signal of the solution (5 mg/L RB19 at t=0 min). The process of dye degradation is observed for all examined catalysts.

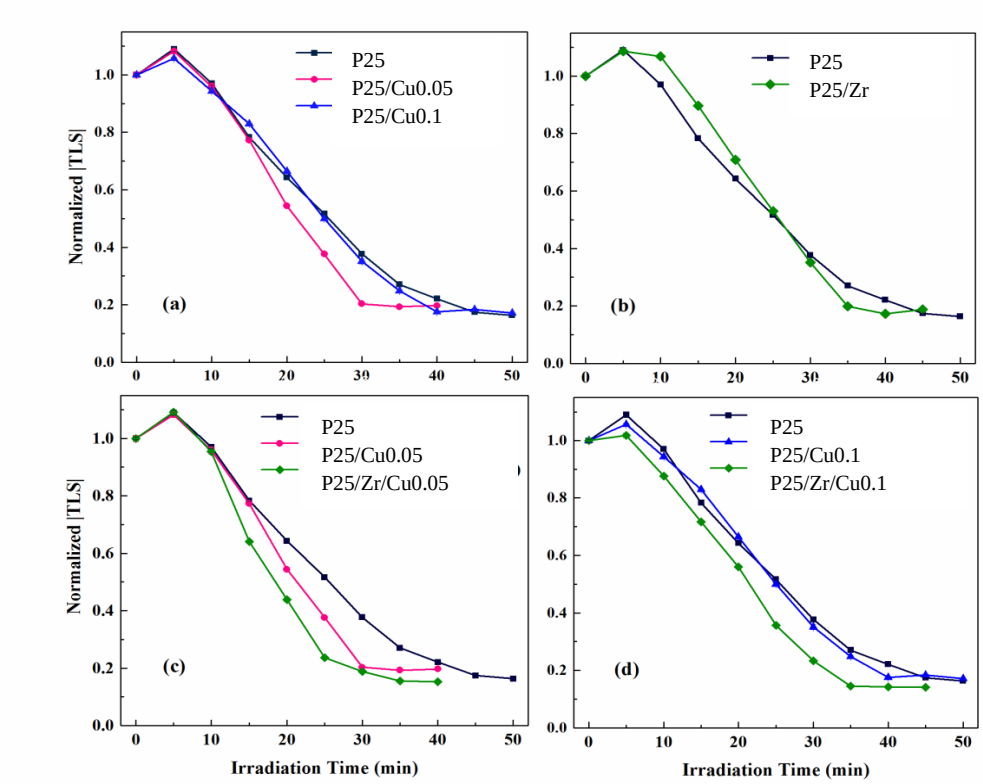

Fig. 43. Temporal evolution (a-d) of the TL signal during the simulated solar light irradiation of RB19 aqueous solution (5 mg/L) accompanied with 0.06 mg/L P25 or Cu/Zr modified P25.

Even though the overall performance of the material tested at high dye concentration (50 mg/L) is highly affected by the photosensitization mechanism and the mechanism responsible for the dye degradation at low concentration (5 mg/L) is shown to be photocatalytic, the trend in efficiency of tested photocatalyst is the same. The results show, that modification of P25 with 0.05 mol % of copper accelerates the degradation process. The higher amount (0.1 mol %) of copper loading has negative effect on the degradation kinetics of RB19, comparing to lower copper loading. There is no significant effect of zirconia loading on the degradation of RB19 at such low concentration. Fig.43 (c) and 43 (d), respectively, show the effect of P25/Zr/$Cu_{0.05}$ and P25/Zr/$Cu_{0.1}$ modified TiO_2 on the rate of RB19 degradation in comparison to P25 and Cu modified P25. These results are in good agreement with correlation between the mineralization and decolorization processes of RB19 under the simulated solar light showed elsewhere (Abu Bakar et al. 2015).

Conclusions

The attempt to distinguish between photocatalytic and photosensitization mechanisms of RB19 dye degradation was successfully made.

The results demonstrate the capability of TLS method to follow up the RB19 dye degradation under the simulated solar light at initial dye concentration 5 mg/L. The lowest detectable concentration of RB19 was found to be 110 μg/L. However, considering excitation of the dye at the maximum absorption peak it was estimated that the LOD should be improved even down to 53 μg/L.

The 3rd hypothesis was confirmed. At concentration 50 mg/L RB19, dye degrades by means of photosensitization mechanism at the beginning of the process, while presence of both mechanisms are registered at longer irradiation time. It was shown that at 5 mg/L RB19, dye degradation assisted with 0.06 mg/L TiO_2 photocatalysts under the simulated solar light proceeds by photocatalytic mechanism. The presence of photosensitization mechanism during degradation of 5 mg/L RB19 cannot be excluded. It can be concluded that it is possible that under the simulated solar light the predominant mechanism (photocatalytic/photosensitization) responsible for the dye degradation may change with dye concentration changes. Dominans of photocatalytic mechanism at lower dye concentrations may lead to good agreement between mineralization and decolorization processes. Deeper analysis of adsorption processes at such a low concentrations of dye and photocatalyst are necessary in order to understand the reasons of mechanism changes.

CONCLUSIONS OF THE THESIS AND FUTURE OUTLOOK

The 1st hypothesis was confirmed. Loading of Zr to the copper containing TiO_2 samples showed enhanced activity towards model pollutants. Cu and Zr couple is a promising combination for development of TiO_2 based materials with enhanced photocatalytic properties for dye polluted water treatment.

The 2nd hypothesis was disproved. The formation of Cu-O-Zr moieties was not confirmed. At the same time, however, it was shown that Zr containing species cover rutile acidic sites on the surface of mixed phase TiO_2 and provoke formation of copper – anatase containing species, which positively influences photocatalytic activity. It was observed that the formation of increased amount of H_2O_2, noticed with electron paramagnetic resonance measurements, does not affect the RB19 dye degradation. This observation supports the opinion about the great contribution of surface trapped holes (surface-bounded OH), but not free $HO^{\cdot}$ radicals in the degradation of RB19 under the simulated solar light.

The 3rd hypothesis of the thesis was confirmed. It is possible to register photocatalytic mechanism of RB19 dye at concentration 5 mg/L under the simulated solar light. This may suggest that the governing mechanism of RB19 dye may change with changing dye concentration under the simulated solar light.

I believe that findings of this thesis give a solid basis for further work to be done in order to obtain more precise quantitative information about details of mechanism responsible for water pollutants degradation at low pollutants concentrations. This approach may shed light on the distinguishing between two different mechanisms (direct hole/surface bounded $HO^{\cdot}$ and free $HO^{\cdot}$ radical oxidation), which can probably coexist and contribute to the overall degradation process.

Finally, the choice of the method and the model pollutant are the crucial points at photocatalyst/pollutant pair characterization. It is difficult to develop the general-purpose strategy for all photocatalytic systems. The specific character of both the material and the pollutant must be taken into account. Meticulous attention should be paid to the understanding of the whole process, which is responsible for the formation of the tracking substance. The success in the experimental results interpretation is strongly dependent on correctly chosen strategy and deep understanding of general features of the experiment.

REFERENCES

Abu Bakar F, Ruzicka JY, Nuramdhani I, et al (2015) Investigation of the photodegradation of Reactive Blue 19 on P-25 titanium dioxide: Effect of experimental parameters. Aust J Chem. 68(3):471-480. doi: 10.1071/CH14024

Akpan UG, Hameed BH (2009) Parameters affecting the photocatalytic degradation of dyes using TiO_2-based photocatalysts: A review. J. Hazard. Mater. 170(2-3):520-9. doi: 10.1016/j.jhazmat.2009.05.039.

Akpan UG, Hameed BH, Amini M, et al (2009) Fundamental principles and application of heterogeneous photocatalytic degradation of dyes in solution. Chem Eng J. 151:10-18. doi: 10.1016/j.cej.2009.02.026

Al-Ekabi H, Serpone N, Pelizzetti E, et al (1989) Kinetic studies in heterogeneous photocatalysis. 2. TiO_2 -mediated degradation of 4-Chlorophenol alone and in a three-component mixture of 4-Chlorophenol, 2,4-Dichlorophenol, and 2,4,5-Trichlorophenol in air-equilibrated aqueous media. Langmuir. 5(1):250-255. doi: 10.1021/la00085a048

Alayon EMC, Nachtegaal M, Bodi A, et al (2015) Bis(μ-oxo) versus mono(μ-oxo)dicopper cores in a zeolite for converting methane to methanol: an in situ XAS and DFT investigation. Phys Chem Chem Phys 17:7681–7693. doi: 10.1039/C4CP03226H

Anastas P, Eghbali N (2010) Green chemistry: Principles and practice. Chem Soc Rev. 39**:** 301-312. doi: 10.1039/B918763B

Andersson M, Österlund L, Ljungström S, Palmqvist A (2002) Preparation of nanosize anatase and rutile TiO_2 by hydrothermal treatment of microemulsions and their activity for photocatalytic wet oxidation of phenol. J Phys Chem B 106:10674–10679. doi: 10.1021/jp025715y

Augugliaro V, Baiocchi C, Prevot AB, et al (2002) Azo-dyes photocatalytic degradation in aqueous suspension of TiO_2 under solar irradiation. Chemosphere. 49(10):1223-1230. doi: 10.1016/S0045-6535(02)00489-7

Bae S, Kim S, Lee S, Choi W (2014) Dye decolorization test for the activity assessment of visible light photocatalysts: Realities and limitations. Catal Today. 224:21-28. doi: 10.1016/j.cattod.2013.12.019

Baiju K V., Zachariah A, Shukla S, et al (2009) Correlating photoluminescence and photocatalytic activity of mixed-phase nanocrystalline titania. Catal Letters.

130(1-2):130-136. doi: 10.1007/s10562-008-9798-5

Banat IM, Nigam P, Singh D, Marchant R (1996) Microbial decolorization of textile-dye-containing effluents: A review. Bioresour Technol. 58(3):217-227. doi: 10.1016/S0960-8524(96)00113-7

Banerjee S, Gopal J, Muraleedharan P, et al (2006) Physics and chemistry of photocatalytic titanium dioxide : Visualization of bactericidal activity using atomic force microscopy. Curr sciense 90:1378–1383

Behnajady MA, Eskandarloo H (2013) Silver and copper co-impregnated onto TiO_2-P25 nanoparticles and its photocatalytic activity. Chem Eng J. 228(Thin Solid Films 496 2006):1207-1213. doi: 10.1016/j.cej.2013.04.110

Bhatnagar A, Sillanpää M (2010) Utilization of agro-industrial and municipal waste materials as potential adsorbents for water treatment-A review. Chem. Eng. J. 157(2-3):277-296. doi: 10.1016/j.cej.2010.01.007

Bickley RI, Gonzalez-Carreno T, Lees JS, et al (1991) A structural investigation of titanium dioxide photocatalysts. J Solid State Chem. 92(1):178-190. doi: 10.1016/0022-4596(91)90255-G

Bilal M, Rasheed T, Iqbal HMN, et al (2018) Photocatalytic degradation, toxicological assessment and degradation pathway of C.I. Reactive Blue 19 dye. Chem Eng Res Des. 129:384-390. doi: 10.1016/j.cherd.2017.11.040

Boonstra AH, Mutsaers CAHA (1975a) Photohydrogenation of ethyne and ethene on the surface of titanium dioxide. J Phys Chem. 79(19):2025-2027. doi: 10.1021/j100586a009

Boonstra AH, Mutsaers CAHA (1975b) Adsorption of hydrogen peroxide on the surface of titanium dioxide. J Phys Chem. 79(18):1940-1943. doi: 10.1021/j100585a011

Bubacz K, Kusiak-Nejman E, Tryba B, Morawski AW (2013) Investigation of OH radicals formation on the surface of TiO_2/N photocatalyst at the presence of terephthalic acid solution. Estimation of optimal conditions. J Photochem Photobiol A Chem 261:7–11. doi: 10.1016/j.jphotochem.2013.04.003

Burhenne J, Riedel KD, Rengelshausen J, et al (2008) Quantification of cationic anti-malaria agent methylene blue in different human biological matrices using cation exchange chromatography coupled to tandem mass spectrometry. J Chromatogr B Anal Technol Biomed Life Sci. 863(2):273-282. doi:

10.1016/j.jchromb.2008.01.028

Butler MA (1978) Prediction of flatband potentials at semiconductor-electrolyte interfaces from atomic electronegativities. J Electrochem Soc 125:228. doi: 10.1149/1.2131419

Byrne JA, Fernandez-Ibañez PA, Dunlop PSM, et al (2011) Photocatalytic enhancement for solar disinfection of water: A review. Int J Photoenergy 2011(12):. doi: 10.1155/2011/798051

Carliell CM, Barclay SJ, Buckley CA (1996) Treatment of exhausted reactive dyebath effluent using anaerobic digestion: Laboratory and full-scale trials. Water SA 22:225–234. doi: ISSN 0378-4738

Carp O, Huisman CL, Reller A (2004) Photoinduced reactivity of titanium dioxide. Prog Solid State Chem 32:33–177. doi: 10.1016/j.progsolidstchem.2004.08.001

Castagnola NB, Kropf AJ, Marshall CL (2005) Studies of Cu-ZSM-5 by X-ray absorption spectroscopy and its application for the oxidation of benzene to phenol by air. Appl Catal A Gen 290:110–122. doi: 10.1016/j.apcata.2005.05.022

Černigoj U, Kete M, Štangar UL (2010) Development of a fluorescence-based method for evaluation of self-cleaning properties of photocatalytic layers. Catal Today 151:46–52. doi: 10.1016/j.cattod.2010.03.043

Chevalier Y, Bolzinger MA (2013) Emulsions stabilized with solid nanoparticles: Pickering emulsions. Colloids Surfaces A Physicochem Eng Asp. 439:23-34. doi: 10.1016/j.colsurfa.2013.02.054

Chiang K, Amal R, Tran T (2002) Photocatalytic degradation of cyanide using titanium dioxide modified with copper oxide. Adv Environ Res 6:471–485. doi: 10.1016/S1093-0191(01)00074-0

Choi W, Termin A, Hoffmann MR (1994) The role of metal ion dopants in quantum-sized TiO_2: Correlation between photoreactivity and charge carrier recombination dynamics. J Phys Chem 98:13669–13679. doi: 10.1021/j100102a038

Chong MN, Jin B, Chow CWK, Saint C (2010) Recent developments in photocatalytic water treatment technology: A review. Water Res 44:2997–3027. doi: 10.1016/j.watres.2010.02.039

Choudhury B, Dey M, Choudhury A (2013) Defect generation, d-d transition, and

band gap reduction in Cu-doped TiO_2 nanoparticles. Int Nano Lett 3:25. doi: 10.1186-2228-5326-3-25

Chung S-L, Wang C-M (2012) Solution combustion synthesis of TiO_2 and its use for fabrication of photoelectrode for dye-sensitized solar cell. J Mater Sci Technol 28:713–722. doi: 10.1016/S1005-0302(12)60120-0

Čižmar T, Lavrenčič Štangar U, Fanetti M, Arčon I (2018) Effects of different copper loadings on the photocatalytic activity of TiO_2 - SiO_2 prepared at a low temperature for the oxidation of organic pollutants in water. ChemCatChem 10:2982. doi: 10.1002/cctc.201800249

Cussler EL (1997) Diffusion: Mass transfer in fluid systems, 2nd edition

Czoska AM, Livraghi S, Chiesa M, et al (2008) The nature of defects in fluorine-doped TiO_2. J Phys Chem C. 112(24):8951-8956. doi: 10.1021/jp8004184

Dahl M, Liu Y, Yin Y (2014) Composite titanium dioxide nanomaterials. Chem Rev 114:9853–9889. doi: 10.1021/cr400634p

Dellamatrice PM, Silva-Stenico ME, Moraes LAB de, et al (2017) Degradation of textile dyes by cyanobacteria. Brazilian J Microbiol. 48(1):25-31. doi: 10.1016/j.bjm.2016.09.012

Di Paola A, Marcì G, Palmisano L, et al (2002) Preparation of polycrystalline TiO_2 photocatalysts impregnated with various transition metal ions: Characterization and photocatalytic activity for the degradation of 4-nitrophenol. J Phys Chem B 106:637–645. doi: 10.1021/jp013074l

Domingos RF, Baalousha MA, Ju-Nam Y, et al (2009) Characterizing manufactured nanoparticles in the environment: Multimethod determination of particle sizes. Environ Sci Technol 43:7277–7284. doi: 10.1021/es900249m

Dong H, Zeng G, Tang L, et al (2015) An overview on limitations of TiO_2-based particles for photocatalytic degradation of organic pollutants and the corresponding countermeasures. Water Res 79:128–146. doi: 10.1016/j.watres.2015.04.038

dos Santos AB, Cervantes FJ, van Lier JB (2007) Review paper on current technologies for decolourisation of textile wastewaters: Perspectives for anaerobic biotechnology. Bioresour Technol 98:2369–2385. doi: 10.1016/j.biortech.2006.11.013

Duling DR (1994) Simulation of multiple isotropic spin-trap EPR spectra. J Magn

Reson Ser B. 104(2):105-110. doi: 10.1006/jmrb.1994.1062

Epling GA, Lin C (2002) Photoassisted bleaching of dyes utilizing TiO_2 and visible light. Chemosphere 46:561–570. doi: 10.1016/S0045-6535(01)00173-4

Forgacs E, Cserhti T, Oros G (2004) Removal of synthetic dyes from wastewaters: A review. Environ Int 30:953–971. doi: 10.1016/j.envint.2004.02.001

Frank SN, Bard AJ (1977) Heterogeneous photocatalytic oxidation of cyanide ion in aqueous solutions at TiO_2 powder. J Am Chem Soc 99:303–304. doi: 10.1021/ja00443a081

Franko M (2001) Recent applications of thermal lens spectrometry in food analysis and environmental research. Talanta. 54:1-13. doi: 10.1016/S0039-9140(00)00608-1

Fu X, Clark LA, Yang Q, Anderson MA (1996) Enhanced photocatalytic performance of titania-based binary metal oxides: TiO_2 /SiO_2 and TiO_2 /ZrO_2. Environ Sci Technol 30:647–653. doi: 10.1021/es950391v

Fujishima A, Rao TN, Tryk DA (2000) Titanium dioxide photocatalysis. J Photochem Photobiol C Photochem Rev 1:1–21. doi: 10.1016/S1389-5567(00)00002-2

Goldstein J, Newbury DE, Joy DC, et al (2003) Scanning electron microscopy and X-ray microanalysis

Gonçalves* IMC, Gomes A, Brás R, et al (2000) Biological treatment of effluent containing textile dyes. J Soc Dye Colour. 116(12):393-397. doi: 10.1111/j.1478-4408.2000.tb00016.x

Gould IR, Ege D, Moser JE, Farid S (1990) Efficiencies of photoinduced electron-transfer reactions: Role of the marcus inverted region in return electron transfer within geminate radical-ion pairs. J Am Chem Soc. 112(11):4290-4301. doi: 10.1021/ja00167a027

Guerrero-Araque D, Ramírez-Ortega D, Acevedo-Peña P, et al (2017) Interfacial charge-transfer process across ZrO_2-TiO_2 heterojunction and its impact on photocatalytic activity. J Photochem Photobiol A Chem 335:276–286. doi: 10.1016/j.jphotochem.2016.11.030

Gupta VK, Ali I, Saleh T a., et al (2012) Chemical treatment technologies for waste-water recycling—an overview. RSC Adv 2:6380. doi: 10.1039/c2ra20340e

Haber J, Block JH, Delmon B (1995) Manual of methods and procedures for catalyst

characterization (Technical Report). Pure Appl Chem 67:1257–1306. doi: 10.1351/pac199567081257

Hanaor D a H, Sorrell CC (2011) Review of the anatase to rutile phase transformation. J Mater Sci 46:855–874. doi: 10.1007/s10853-010-5113-0

Harada K, Hisanaga T, Tanaka K (1990) Photocatalytic degradation of organophosphorous insecticides in aqueous semiconductor suspensions. Water Res 24:1415–1417. doi: 10.1016/0043-1354(90)90162-Y

Hargreaves J.S.J (2016) Some considerations related to the use of the Scherrer equation in powder X-ray diffraction as applied to heterogeneous catalysts. J Catalysis, Structure and Reactivity, 2:1-4, 33-37. doi: 10.1080/2055074X.2016.1252548).

He J, Zhao J, Shen T, et al (2002) Photosensitization of colloidal titania particles by electron injection from an excited organic dye−antennae function. J Phys Chem B. 101(44):9027-9034. doi: 10.1021/jp971550v

Helaïli N, Bessekhouad Y, Bouguelia A, Trari M (2009) Visible light degradation of Orange II using xCu_yO_z/TiO_2 heterojunctions. J Hazard Mater. 168(1):484-92. doi: 10.1016/j.jhazmat.2009.02.066

Herbst W, Hunger K, Wilker G, et al (2005) Industrial organic pigments: Production, properties, applications: Third, Completely Revised Edition

Hernández-Alonso MD, Tejedor-Tejedor I, M CJ, et al (2006) Sol–gel preparation of TiO_2–ZrO_2 thin films supported on glass rings: Influence of phase composition on photocatalytic activity. Thin Solid Films 502:125–131. doi: http://dx.doi.org/10.1016/j.tsf.2005.07.256

Herrmann JM (1999) Heterogeneous photocatalysis: Fundamentals and applications to the removal of various types of aqueous pollutants. Catal Today. 53(1):115-129. doi: 10.1016/S0920-5861(99)00107-8

Hoffmann MR, Martin ST, Choi W, Bahnemannt DW (1995) Environmental applications of semiconductor photocatalysis. Chem Rev 95:69–96. doi: 10.1021/cr00033a004

Holkar CR, Jadhav AJ, Pinjari D V., et al (2016) A critical review on textile wastewater treatments: Possible approaches. J. Environ. Manage. 182:351-366. doi: 10.1016/j.jenvman.2016.07.090.

Hu C, Yu JC, Hao Z, Wong PK (2003) Photocatalytic degradation of triazine-

containing azo dyes in aqueous TiO_2 suspensions. Appl Catal B Environ. 42:47-55. doi: 10.1016/S0926-3373(02)00214-X

Hurum DC, Agrios AG, Gray KA, et al (2003) Explaining the enhanced photocatalytic activity of Degussa P25 mixed-phase TiO_2 using EPR. J Phys Chem B 107:4545–4549. doi: 10.1021/jp0273934

Ilkhechi NN, Ahmadi A, Kaleji BK (2015a) Optical and structural properties of nanocrystalline anatase powders doped by Zr, Si and Cu at high temperature. Opt Quantum Electron 47:2423–2434. doi: 10.1007/s11082-015-0120-7

Ilkhechi NN, Kaleji BK, Salahi E, Hosseinabadi N (2015b) Comparison of optical and structural properties of Cu doped and Cu/Zr co-doped TiO_2 nanopowders calcined at various temperatures. J Sol-Gel Sci Technol 765–773. doi: 10.1007/s10971-015-3661-0

Irie H, Kamiya K, Shibanuma T, et al (2009) Visible light-sensitive Cu(II)-grafted TiO_2 photocatalysts: Activities and X-ray absorption fine structure analyses. J Phys Chem C 113:10761–10766. doi: 10.1021/jp903063z

Irie H, Miura S, Kamiya K, Hashimoto K (2008) Efficient visible light-sensitive photocatalysts: Grafting Cu(II) ions onto TiO_2 and WO_3 photocatalysts. Chem Phys Lett. 475(1-3):202-205. doi: 10.1016/j.cplett.2008.04.006

Jaeger CD, Bard AJ (2005) Spin trapping and electron spin resonance detection of radical intermediates in the photodecomposition of water at titanium dioxide particulate systems. J Phys Chem. 83(24):3146-3152. doi: 10.1021/j100487a017

Jafry HR, Liga M V., Li Q, Barron AR (2011) Simple route to enhanced photocatalytic activity of P25 titanium dioxide nanoparticles by silica addition. Environ Sci Technol. 45(41):563-1568. doi: 10.1021/es102749e

Janczarek M, Kowalska E (2017) On the origin of enhanced photocatalytic activity of copper-modified titania in the oxidative reaction systems. Catalysts. 7(11):317. doi: 10.3390/catal7110317

Jenkins; Snuder (1996) Introduction to X-ray powder diffractometry

Jin Q, Fujishima M, Iwaszuk A, et al (2013) Loading effect in copper(II) oxide cluster-surface-modified titanium(IV) oxide on visible- and UV-light activities. J Phys Chem C 117:23848–23857. doi: 10.1021/jp4085525

Jongsomjit B, PinKaew K, Mekasuwandumrong O, et al (2012) Zirconia modification on nanocrystalline titania-supported cobalt catalysts for

methanation. Eng J 16:29–38. doi: 10.4186/ej.2012.16.4.29

Kakuma Y, Nosaka AY, Nosaka Y (2015) Difference in TiO_2 photocatalytic mechanism between rutile and anatase studied by the detection of active oxygen and surface species in water. Phys Chem Chem Phys. 17**:**18691-18698. doi: 10.1039/c5cp02004b

Karunakaran C, Senthilvelan S (2005) Photocatalysis with ZrO_2: oxidation of aniline. J Mol Catal A Chem 233:1–8. doi: 10.1016/j.molcata.2005.01.038

Kausar A, Iqbal M, Javed A, et al (2018) Dyes adsorption using clay and modified clay: A review. J Mol Liq 256:395–407. doi: 10.1016/j.molliq.2018.02.034

Kete M, Pavlica E, Fresno F, et al (2014) Highly active photocatalytic coatings prepared by a low-temperature method. Environ Sci Pollut Res 21:11238–11249. doi: 10.1007/s11356-014-3077-3

Khan AI, O'Hare D (2002) Intercalation chemistry of layered double hydroxides: recent developments and applications. J Mater Chem 12:3191–3198. doi: 10.1039/b204076j

Klavarioti M, Mantzavinos D, Kassinos D (2009) Removal of residual pharmaceuticals from aqueous systems by advanced oxidation processes. Environ Int 35:402–417. doi: 10.1016/j.envint.2008.07.009

Klosek S, Raftery D (2002) Visible light driven V-doped TiO_2 photocatalyst and its photooxidation of ethanol. J Phys Chem B 105:2815–2819. doi: 10.1021/jp004295e

Koncagül E., Tran M, Connor R, et al (2017) Wastewater the untapped resource. Facts and figures. The United Nations World Water Development Report 2017. 12

Konstantinou IK, Albanis TA (2004) TiO_2-assisted photocatalytic degradation of azo dyes in aqueous solution: Kinetic and mechanistic investigations: A review. Appl Catal B Environ. 49(1):1-14. doi: 10.1016/j.apcatb.2003.11.010

Kontapakdee K, Panpranot J, Praserthdam P (2007) Effect of Ag addition on the properties of Pd–Ag/TiO_2 catalysts containing different TiO_2 crystalline phases. Catal Commun 8:2166–2170. doi: 10.1016/J.CATCOM.2007.03.003

Kubacka A, Fernández-García M, Colón G (2012) Advanced nanoarchitectures for solar photocatalytic applications. Chem Rev 112:1555–1614. doi: 10.1021/cr100454n

Kumar SG, Devi LG (2011) Review on modified TiO_2 photocatalysis under UV/visible light: Selected results and related mechanisms on interfacial charge carrier transfer dynamics. J Phys Chem A 115:13211–13241. doi: 10.1021/jp204364a

Kuo WS, Ho PH (2001) Solar photocatalytic decolorization of methylene blue in water. Chemosphere. 45(1):77-83. doi: 10.1016/S0045-6535(01)00008-X

Lawless D, Serpone N, Meisel D (2005) Role of hydroxyl radicals and trapped holes in photocatalysis. A pulse radiolysis study. J Phys Chem. 95(13):5166-5170. doi: 10.1021/j100166a047

Li G, Dimitrijevic NM, Chen L, et al (2008) Role of surface/interfacial Cu^{2+} sites in the photocatalytic activity of coupled CuO−TiO_2 nanocomposites. J Phys Chem C 112:19040–19044. doi: 10.1021/jp8068392

Li H, Bian Z, Zhu J, et al (2007) Mesoporous Au/TiO_2 nanocomposites with enhanced photocatalytic activity. J Am Chem Soc 129:4538–4539. doi: 10.1021/ja069113u

Lin F, Meng X, Kukueva E, et al (2015) Direct-synthesis method towards copper-containing periodic mesoporous organosilicas: detailed investigation of the copper distribution in the material. Dalt Trans 44:9970–9979. doi: 10.1039/C4DT03719G

Lin W, Frei H (2005a) Anchored metal-to-metal charge-transfer chromophores in a mesoporous silicate sieve for visible-light activation of titanium centers. J Phys Chem B 109:4929–4935. doi: 10.1021/jp040677z

Lin W, Frei H (2005b) Photochemical CO_2 splitting by metal-to-metal charge-transfer excitation in mesoporous ZrCu(I)-MCM-41 silicate sieve. J Am Chem Soc 127:1610–1. doi: 10.1021/ja040162l

Linsebigler AL, Linsebigler AL, Yates Jr JT, et al (1995) Photocatalysis on TiO_2 surfaces: Principles, Mechanisms, and Selected Results. Chem Rev 95:735–758. doi: 10.1021/cr00035a013

Lippens PE, Chadwick A V., Weibel A, et al (2008) Structure and chemical bonding in Zr-doped anatase TiO_2 nanocrystals. J Phys Chem C 112:43–47. doi: 10.1021/jp075898u

Liu G, Li X, Zhao J, et al (2000) Photooxidation mechanism of dye alizarin red in TiO_2 dispersions under visible illumination: An experimental and theoretical

examination. J Mol Catal A Chem. 153(1):221-229. doi: 10.1016/S1381-1169(99)00351-9

Liu M, Inde R, Nishikawa M, et al (2014) Enhanced photoactivity with nanocluster-grafted titanium dioxide photocatalysts. ACS Nano 8:7229–7238. doi: 10.1021/nn502247x

López R, Gómez R (2012) Band-gap energy estimation from diffuse reflectance measurements on sol-gel and commercial TiO_2: A comparative study. J Sol-Gel Sci Technol 61:1–7. doi: 10.1007/s10971-011-2582-9

Luttrell T, Halpegamage S, Tao J, et al (2014) Why is anatase a better photocatalyst than rutile? - Model studies on epitaxial TiO_2 films. Sci Rep 4:515–582. doi: 10.1038/srep04043

Lye J (2002) Colour chemistry. Color Res. Appl.

Lytle FW, Greegor RB, Panson AJ (1988) Discussion of x-ray-absorption near-edge structure: Application to Cu in the high-Tc superconductors $La_{1.8}Sr_{0.2}CuO_4$ and $YBa_2Cu_3O_7$. Phys Rev B 37:1550–1562. doi: 10.1103/PhysRevB.37.1550

MacKenzie R (2010) Clearing the waters over hygiene debate.

Mallakpour S, Nikkhoo E (2014) Surface modification of nano-TiO_2 with trimellitylimido-amino acid-based diacids for preventing aggregation of nanoparticles. Adv Powder Technol. 25(1):348-353. doi: 10.1016/j.apt.2013.05.017

Malvern, Instruments M (2011) Dynamic light scattering : An introduction in 30 minutes. Tech Note MRK656-01

Marcano A, Cabrera H, Guerra M, et al (2006) Optimizing and calibrating a mode-mismatched thermal lens experiment for low absorption measurement. J Opt Soc Am 23(7):1408-1413. doi: 10.1364/JOSAB.23.001408

Minero C, Vione D (2006) A quantitative evalution of the photocatalytic performance of TiO_2 slurries. Appl Catal B Environ. 67:257-269. doi: 10.1016/j.apcatb.2006.05.011

Morozov I V., Znamenkov KO, Korenev YM, Shlyakhtin OA (2003) Thermal decomposition of $Cu(NO_3)_2 \cdot 3H_2O$ at reduced pressures. Thermochim Acta 403:173–179. doi: 10.1016/S0040-6031(03)00057-1

Mukherjee PS, Ray AK (1999) Major challenges in the design of a large-scale photocatalytic reactor for water treatment. Chem Eng Technol 22:253–260. doi:

10.1002/(SICI)1521-4125(199903)22:3<253::AID-CEAT253>3.0.CO;2-X

Nagaveni K, Hegde MS, Madras G (2004) Structure and photocatalytic activity of $Ti_{1-x}MxO_{2\pm\delta}$ (M = W, V, Ce, Zr, Fe, and Cu) Synthesized by solution combustion method. J Phys Chem B 108:20204–20212. doi: 10.1021/jp047917v

Nasr C, Vinodgopal K, Fisher L, et al (1996) Environmental photochemistry on semiconductor surfaces. Visible light induced degradation of a textile diazo dye, Naphthol Blue Black, on TiO_2 Nanoparticles. J Phys Chem. 100(20):8436-8442. doi: 10.1021/jp953556v

Nawrocki J, Rigney M, McCormick A, Carr PW (1993) Chemistry of zirconia and its use in chromatography. J Chromatogr A 657:229–282. doi: 10.1016/0021-9673(93)80284-F

Neubert S, Mitoraj D, Shevlin SA, et al (2016) Highly efficient rutile TiO_2 photocatalysts with single Cu(II) and Fe(III) surface catalytic sites. J Mater Chem A. 4:3127-3138. doi: 10.1039/c5ta07036h

Nolan M, Iwaszuk A, Tada H (2012) Molecular metal oxide cluster-surface modified titanium(iv) dioxide photocatalysts. Aust. J. Chem. 65(6):624-632. doi: 10.1071/CH11451

Ohtani B, Prieto-Mahaney OO, Li D, Abe R (2010) What is Degussa (Evonic) P25? Crystalline composition analysis, reconstruction from isolated pure particles and photocatalytic activity test. J Photochem Photobiol A Chem. 216:179-182. doi: 10.1016/j.jphotochem.2010.07.024

Ollis D.F (2000) Photocatalytic purification and remediation of contaminated air and water. Comptes Rendus l'Académie des Sci - Ser IIC - Chem 3:405–411. doi: 10.1016/S1387-1609(00)01169-5

Pagni RM, Sigman ME (1999) The photochemistry of PAHs and PCBs in water and on solids. Environ Photochem Part 1 Part 1:139–180. doi: 10.1007/b138184

Palmisano L, Augugliaro V, Sclafani a., Schiavello M (1988) Activity of chromium-ion-doped titania for the dinitrogen photoreduction to ammonia and for the phenol photodegradation. J Phys Chem 92:6710–6713. doi: 10.1021/j100334a044

Papp J, Soled S, Dwight K, Wold A (1994) Surface acidity and photocatalytic activity of TiO_2, WO_3/TiO_2, and MoO_3/TiO_2 photocatalysts. Chem Mater 6:496–500. doi: 10.1021/cm00040a026

Paulauskas IE, Modeshia DR, Ali TT, et al (2013) Photocatalytic activity of doped and undoped titanium dioxide nanoparticles synthesised by flame spray pyrolysis. Platin Met Rev 57:32–43. doi: 10.1595/147106713X659109

Pearce CI, Lloyd JR, Guthrie JT (2003) The removal of colour from textile wastewater using whole bacterial cells: A review. Dye Pigment 58:179–196. doi: 10.1016/S0143-7208(03)00064-0

Pellegrino F, Pellutiè L, Sordello F, Minero C, et al (2017) Influence of agglomeration and aggregation on the photocatalytic activity of TiO_2 nanoparticles. Applied Catal B, Environ. 216:80-87. doi: 10.1016/j.apcatb.2017.05.046

Peng F, Cai L, Huang L, et al (2008) Preparation of nitrogen-doped titanium dioxide with visible-light photocatalytic activity using a facile hydrothermal method. J Phys Chem Solids 69:1657–1664. doi: 10.1016/j.jpcs.2007.12.003

Petronella F, Truppi A, Ingrosso C, et al (2017) Nanocomposite materials for photocatalytic degradation of pollutants. Catal Today 281:85–100. doi: 10.1016/j.cattod.2016.05.048

Phenrat T, Saleh N, Sirk K, et al (2008) Stabilization of aqueous nanoscale zerovalent iron dispersions by anionic polyelectrolytes: Adsorbed anionic polyelectrolyte layer properties and their effect on aggregation and sedimentation.J Nanoparticle Res 10:795–814. doi: 10.1007/s11051-007-9315-6

Philips D (1996) Environmentally friendly, productive and reliable: priorities for cotton dyes and dyeing processes. J Soc Dye Colour. 12:183-190. doi: 10.1111/j.1478-4408.1996.tb01814.x

Pliekhov O, Arčon I, Tušar NN, Štangar UL (2016) Photocatalytic activity of Zirconium- and Manganese-codoped titania in aqueous media: The role of the metal dopant and its incorporation site. ChemCatChem 8:2109–2118. doi: 10.1002/cctc.201600206

Pližingrová E, Klementová M, Bezdička P, et al (2017) 2D-Titanium dioxide nanosheets modified with Nd, Ag and Au: Preparation, characterization and photocatalytic activity. Catal Today. 281:165-180. doi: 10.1016/j.cattod.2016.08.013

Polisetti S, Deshpande PA, Madras G (2011) Photocatalytic activity of combustion synthesized ZrO_2 and ZrO_2-TiO_2 mixed oxides. Ind Eng Chem Res 50:12915–

12924. doi: 10.1021/ie200350f

Prieto-Mahaney O-O, Murakami N, Abe R, Ohtani B (2009) Correlation between photocatalytic activities and structural and physical properties of titanium(IV) oxide powders. Chem Lett 38:238–239. doi: 10.1246/cl.2009.238

Punzi M, Anbalagan A, Aragão Börner R, et al (2015) Degradation of a textile azo dye using biological treatment followed by photo-Fenton oxidation: Evaluation of toxicity and microbial community structure. Chem Eng J. 270:290-299. doi: 10.1016/j.cej.2015.02.042

Rauf MA, Meetani MA, Hisaindee S (2011) An overview on the photocatalytic degradation of azo dyes in the presence of TiO_2 doped with selective transition metals. Desalination 276(1):13- 17. doi: 10.1016/j.desal.2011.03.071

Ravel B, Newville M (2005) ATHENA, ARTEMIS, HEPHAESTUS: data analysis for X-ray absorption spectroscopy using IFEFFIT. J Synchrotron Radiat 12:537–41. doi: 10.1107/S0909049505012719

Rehr JJ, Albers RC, Zabinsky SI (1992) High-order multiple-scattering calculations of x-ray-absorption fine structure. Phys Rev Lett 69:3397–3400. doi: 10.1103/PhysRevLett.69.3397

Reza KM, Kurny ASW, Gulshan F (2015) Parameters affecting the photocatalytic degradation of dyes using TiO_2: a review. Appl Water Sci. 7(4): 1569–1578. doi: 10.1007/s13201-015-0367-y

Riaz N, Chong FK, Man ZB, et al (2013) Photodegradation of orange II under visible light using Cu-Ni/TiO_2: Influence of Cu: Ni mass composition, preparation, and calcination temperature. Ind Eng Chem Res. 52 (12): 4491-4503. doi: 10.1021/ie303255v

Rochkind M, Pasternak S, Paz Y (2015) Using dyes for evaluating photocatalytic properties: A critical review. Molecules 20:88–110. doi: 10.3390/molecules20010088

Sahu M, Biswas P (2011) Single-step processing of copper-doped titania nanomaterials in a flame aerosol reactor. Nanoscale Res Lett 6:441. doi: 10.1186/1556-276X-6-441

Saito G, Nakasugi Y, Sakaguchi N, et al (2015) Glycine-nitrate-based solution-combustion synthesis of $SrTiO_3$. J Alloys Compd 652:496–502. doi: 10.1016/j.jallcom.2015.08.227

Sakthivel S, Shankar M., Palanichamy M, et al (2004) Enhancement of photocatalytic activity by metal deposition: characterisation and photonic efficiency of Pt, Au and Pd deposited on TiO_2 catalyst. Water Res 38:3001–3008. doi: 10.1016/j.watres.2004.04.046

Salvador P (2011) Mechanisms of water photooxidation at n-TiO_2 rutile single crystal oriented electrodes under UV illumination in competition with photocorrosion. Prog. Surf. Sci. 86(1):41-58. doi: 10.1016/j.progsurf.2010.10.002

Savi EL, Malacarne LC, Baesso ML, et al (2015) Investigation into photostability of soybean oils by thermal lens spectroscopy. Spectrochim Acta - Part A Mol Biomol Spectrosc. 145(15): 125-129. doi: 10.1016/j.saa.2015.02.106

Schneider J, Matsuoka M, Takeuchi M, et al (2014) Understanding TiO_2 photocatalysis : Mechanisms and Materials. Chem Rev 114:9919–9986. doi: 10.1021/cr5001892

Sclafani A, Herrmann JM (1996) Comparison of the photoelectronic and photocatalytic activities of various anatase and rutile forms of titania in pure liquid organic phases and in aqueous solutions. J Phys Chem 100:13655–13661. doi: 10.1021/jp9533584

Shanker U, Rani M, Jassal V (2017) Degradation of hazardous organic dyes in water by nanomaterials. Environ. Chem. Lett. 15 (4): 623-642. doi: 10.1007/s10311-017-0650-2

Sing KSW (1985) Reporting physisorption data for gas/solid systems with special reference to the determination of surface area and porosity (Recommendations 1984). Pure Appl Chem 57:603–619. doi: 10.1351/pac198557040603

Sirés I, Brillas E (2012) Remediation of water pollution caused by pharmaceutical residues based on electrochemical separation and degradation technologies: A review. Environ Int 40:212–229. doi: 10.1016/j.envint.2011.07.012

Sivalingam G, Nagaveni K, Hegde MS, Madras G (2003) Photocatalytic degradation of various dyes by combustion synthesized nano anatase TiO_2. Appl Catal B Environ 45:23–38. doi: 10.1016/S0926-3373(03)00124-3

Snook RD, Lowe RD (1995) Thermal lens spectrometry. A review. Analyst. 120: 2051-2068. doi: 10.1039/an9952002051

Stasinakis AS (2008) Use of selected advanced oxidation processes (AOPs) for

wastewater treatment - A mini review. Glob Nest J 10(3): 376-385.

Štengl V, Bakardjieva S (2010) Molybdenum-doped anatase and its extraordinary photocatalytic activity in the degradation of Orange II in the UV and vis regions. J Phys Chem C 114:19308–19317. doi: 10.1021/jp104271q

Su K, Ai Z, Zhang L (2012) Efficient visible light-driven photocatalytic degradation of pentachlorophenol with Bi_2O_3/TiO_2– xB_x. J Phys Chem C 116:17118–17123. doi: 10.1021/jp305432g

Šuligoj A, Arčon I, Mazaj M, et al (2018) Surface modified titanium dioxide using transition metals: nickel as a winning transition metal for solar light photocatalysis. J Mater Chem A. 6 (21): 9882-9892. doi: 10.1039/C7TA07176K

Sun J, Gao L, Zhang Q (2003) Synthesizing and comparing the photocatalytic properties of high surface area rutile and anatase titania nanoparticles. J Am Ceram Soc 86:1677–1682. doi: 10.1111/j.1151-2916.2003.tb03539.x

Suttiponparnit K, Jiang J, Sahu M, et al (2011) Role of surface area, primary particle size, and crystal phase on titanium dioxide nanoparticle dispersion properties. Nanoscale Res Lett. 6 (27). doi: 10.1007/s11671-010-9772-1

Taurozzi JS, Hackley V a, Wiesner MR (2012) Preparation of a nanoscale TiO_2 aqueous dispersion for toxicological or environmental testing. NIST Spec Publ 1200:3. doi: 10.6028/NIST.SP.1200

Tayade RJ, Kulkarni RG, Jasra R V. (2006) Transition metal ion impregnated mesoporous TiO_2 for photocatalytic degradation of organic contaminants in water. Ind Eng Chem Res. 45(15): 5231-5238. doi: 10.1021/ie051362o

Thiruvenkatachari R, Kwon TO, Jun JC, et al (2007) Application of several advanced oxidation processes for the destruction of terephthalic acid (TPA). J Hazard Mater 142: 308–314. doi: 10.1016/j.jhazmat.2006.08.023

Tiburcio-Moreno JA, Marcelín-Jiménez G, Leanos-Castaneda OL, et al (2012) Study of the photodegradation process of vitamin e acetate by optical absorption, fluorescence, and thermal lens spectroscopy. Int J Thermophys 33:2062–2068. doi: 10.1007/s10765-012-1311-0

Tishchenko K, Muratova M, Volkov D, et al (2017) Multi-wavelength thermal-lens spectrometry for high-accuracy measurements of absorptivities and quantum yields of photodegradation of a hemoprotein–lipid complex. Arab J Chem. 10(6): 781-791. doi: 10.1016/j.arabjc.2016.01.009

Venkatachalam N, Palanichamy M, Arabindoo B, Murugesan V (2007) Enhanced photocatalytic degradation of 4-chlorophenol by Zr^{4+} doped nano TiO_2. J Mol Catal A Chem 266:158–165. doi: 10.1016/j.molcata.2006.10.051

Vodišek N, Ramanujachary K, Brezová V, Lavrenčič Štangar U (2016) Transparent titania-zirconia-silica thin films for self-cleaning and photocatalytic applications. Catal Today 287:142–147. doi: 10.1016/j.cattod.2016.12.026

Wang Y, Shi R, Lin J, Zhu Y (2010) Significant photocatalytic enhancement in methylene blue degradation of TiO_2 photocatalysts via graphene-like carbon in situ hybridization. Appl Catal B Environ 100:179–183. doi: 10.1016/j.apcatb.2010.07.028

Wendlandt WW (1956) The thermolysis of the rare earth and other metal nitrates. Anal Chim Acta 15:435–439. doi: 10.1016/0003-2670(56)80082-2

Williams DB, Carter CB (2009) Transmission electron microscopy: A textbook for materials science

Wu K, Oikawa K, Hidaka H, Serpone N (1998a) Photoassisted degradation of dye pollutants . 3 . Degradation of the cationic dye Rhodamine B in aqueous anionic surfactant/TiO_2 dispersions under visible light irradiation : Evidence for the need of substrate adsorption on TiO_2 particles. Environ. Sci. Technol. 32:2394–2400. doi: 10.1021/es9707926

Wu T, Liu G, Zhao J, et al (1998b) Photoassisted degradation of dye pollutants. V. self-photosensitized oxidative transformation of *Rhodamine B* under visible light irradiation in aqueous TiO_2 dispersions. J Phys Chem B 102:5845–5851. doi: 10.1021/jp980922c

Xianzhi FU, Clark LA, Yang Q, Anderson MA (1996) Enhanced photocatalytic performance of titania-based binary metal oxides: TiO_2/SiO_2 and TiO_2/ZrO_2. Environ Sci Technol 30:647–653. doi: 10.1021/es950391v

Xin B, Wang P, Ding D, et al (2008) Effect of surface species on Cu-TiO_2 photocatalytic activity. Appl Surf Sci 254:2569–2574. doi: 10.1016/j.apsusc.2007.09.002

Xing M-Y, Qi D-Y, Zhang J-L, Chen F (2011) One-step hydrothermal method to prepare carbon and lanthanum co-doped TiO_2 nanocrystals with exposed {001} facets and their high UV and visible-light photocatalytic activity. Chem - A Eur J 17:11432–11436. doi: 10.1002/chem.201101654

Xu M, Gao Y, Moreno EM, et al (2011) Photocatalytic activity of bulk TiO_2 anatase and rutile single crystals using infrared absorption spectroscopy. Phys Rev Lett. 106: 138302. doi: 10.1103/PhysRevLett.106.138302

Yanagida S, Yoshiya M, Shiragami T, et al (1990) Semiconductor photocatalysis.' Quantitative photoreduction of aliphatic ketones to alcohols using defect-free ZnS quantum crystallites. J Phys Chem. 94(7): 3104-3111. doi: 10.1021/j100370a066

Yong X, Schoonen MAA (2000) The absolute energy positions of conduction and valence bands of selected semiconducting minerals. Am Mineral 85:543–556. doi: 10.2138/am-2000-0416

Yordanov ND, Gancheva V, Pelova VA (1999) Studies on some materials suitable for use as internal standards in high energy EPR dosimetry. J Radioanal and Nuc Chem. 240(2): 619–622. doi: 10.1007/BF02349422

Yuliati L, Ruu Siah W, Roslan NA, et al (2016) Modification of titanium dioxide nanoparticles with copper oxide co-catalyst for photocatalytic degradation of 2,4-Dichlorophenoxyacetic acid. Malaysian J Anal Sci. 6: 5079-5087. doi: 10.17576/mjas-2016-2001-18

Zachariah A, Baiju K V., Shukla S, et al (2008) Synergistic effect in photocatalysis as observed for mixed-phase nanocrystalline titania processed via sol-gel solvent mixing and calcination. J Phys Chem C. 112(30): 11345-11356. doi: 10.1021/jp712174y

Zangeneh H, Zinatizadeh AAL, Habibi M, et al (2015) Photocatalytic oxidation of organic dyes and pollutants in wastewater using different modified titanium dioxides: A comparative review. J Ind Eng Chem. 26: 1-36. doi: 10.1016/j.jiec.2014.10.043

Zawadzki P, Laursen AB, Jacobsen KW, et al (2012) Oxidative trends of TiO_2 - hole trapping at anatase and rutile surfaces. Energy Environ Sci 5:9866–9869. doi: 10.1039/c2ee22721e

Zhang T, Oyama T, Aoshima A, et al (2001) Photooxidative N-demethylation of methylene blue in aqueous TiO_2 dispersions under UV irradiation. J Photochem Photobiol A Chem. 140(2):163-172. doi: 10.1016/S1010-6030(01)00398-7

Zhenhua Pan, Jason A. Röhr, Zuyang Ye, Zachary S. Fishman, Qianhong Zhu X, Shen SH (2019) Elucidating charge separation in particulate photocatalysts

using nearly-intrinsic semiconductors with small asymmetric band bending. Sustain Energy Fuels 216:80–87. doi: 10.1039/C9SE00036D

Zorn ME, Tompkins DT, Zeltner WA, Anderson MA (1999) Photocatalytic oxidation of acetone vapor on TiO_2/ZrO_2 thin films. Appl Catal B Environ 23:1–8. doi: http://dx.doi.org/10.1016/S0926-3373(99)00067-3

Zorn ME, Tompkins DT, Zeltner WA, Anderson MA (2000) Catalytic and photocatalytic oxidation of ethylene on titania-based thin-films. Environ Sci Technol 34:5206–5210. doi: 10.1021/es991250m